

A Mechanistic Model for CO₂
Localized Corrosion of Carbon Steel

A dissertation presented to
the faculty of
the Russ College of Engineering and Technology of Ohio University

In partial fulfillment
of the requirements for the degree
Doctor of Philosophy

Hui Li

June 2011

© 2011 Hui Li. All Rights Reserved.

This dissertation titled
A Mechanistic Model for CO₂
Localized Corrosion of Carbon Steel

by

HUI LI

has been approved for
the Department of Chemical and Biomolecular Engineering
and the Russ College of Engineering and Technology by

Srdjan Nešić

Professor of Chemical and Biomolecular Engineering

Dennis Irwin

Dean, Russ College of Engineering and Technology

ABSTRACT

LI, HUI, Ph.D., June 2011, Chemical Engineering

A Mechanistic Model for CO₂ Localized Corrosion of Carbon Steel

Director of Dissertation: Srdjan Nešić

Localized corrosion of carbon steel in CO₂ environments is a long-standing challenge faced by the oil and gas industry. Extensive research efforts have been dedicated to elucidating the mechanisms governing localized corrosion of carbon steel. Recent studies have discovered pseudo-passivation of carbon steel under FeCO₃ layer-forming conditions where high supersaturation of FeCO₃ and high temperature are typically involved, which appreciably increases the potential of metal. A galvanic coupling mechanism is then proposed for localized corrosion propagation of carbon steel. In this theory, FeCO₃ layer-covered surfaces are considered to undergo a substantial surface pH increase due to the mass transfer limiting effect, which could trigger the formation of pseudo-passive film and result in potential increase of metal surface. In a case where a small portion of this film-covered surface loses the protective film, an active surface that has a lower potential will be exposed. A galvanic cell can then be established between film-covered and active surfaces, which drives the active surface to corrode at a higher rate. Supersaturation of FeCO₃ is found to play a critical role in determining whether a pit propagates or dies. It was found that pit propagation is predominant when the supersaturation is around 1, a condition known as a “grey zone”.¹ Outside the “grey zone”, pits are often captured due to formation of FeCO₃ on the pit surface.

Based on the experimental findings, a new transient mechanistic model is developed in this study to simulate the localized corrosion process of carbon steel in a CO₂ environment (MULTICORP V5). The model covers the physics governing both uniform and localized corrosion, including mass transfer, chemical reactions, electrochemical reactions, FeCO₃ layer formation, FeS layer formation (for uniform corrosion only), pseudo-passivation and pit propagation. Pit initiation is triggered using a statistical function, as mechanisms for pit initiation are still under investigation and not available at this stage of research. The model is able to provide detailed information on critical parameters involved in the corrosion process, such as water chemistry, potential and current distribution in the solution, particularly for those adjacent to the metal surface. This information will assist engineers in better understanding the corrosion process in order to make strategic decisions. The uniform corrosion model has been fully calibrated against and verified with a database that contains a large number of experimental results under various conditions in CO₂/H₂S environments. The localized corrosion model is calibrated against limited experimental data obtained from the artificial pit tests in CO₂ environments. Parametric study is performed for localized corrosion. It is shown that model predictions quantitatively match experimental results and qualitatively agree with the general understanding of the localized corrosion process.

To disseminate the knowledge and raise the level of understanding of corrosion within the broader range of the corrosion community, a stand-alone electrochemical model is developed using Microsoft Excel VBA. The model, named FREECORP, is exclusively based on the public literature and offered free of charge. The model is

capable of predicting steady-state CO₂ and/or HAc uniform corrosion and transient H₂S uniform corrosion for carbon steel. Apart from corrosion rate prediction, polarization curves can also be predicted for individual and overall electrochemical reactions in order to enhance understanding of corrosion mechanisms. In the case of H₂S corrosion, the concentration profile of H₂S across the inner and outer magnetite film and bulk solution is shown in order to give more meaningful information about H₂S corrosion. This model is written with the concept of object-oriented programming (OOP) which provides great flexibility to model calculations. Any reactions, including system-defined and user-defined reactions, can be added or removed from the system, a feature that allows for investigation into the effect of individual reactions on the corrosion process. This feature also permits the expansion of the model into a much wider range of environments than the model was originally designed for. The current model is fully calibrated and verified with a large number of in-house experimental data contained in the ICMT (Institute for Corrosion and Multiphase Flow Technology at Ohio University) database.

Approved: _____

Srdjan Nešić

Professor of Chemical and Biomolecular Engineering

DEDICATION

To

Guangyou Li and Piyu Yan (my parents)

and

Jun Luo (my wife)

ACKNOWLEDGMENTS

I would like to express my sincere gratitude to my advisor and chairman of my dissertation committee, Dr. Srdjan *Nešić*, for his constant guidance and support during my PhD studies. His direction and encouragement are among the key factors for the completion of my PhD degree. Apart from being an esteemed professor and a well-known expert, he also showed great care for issues pertaining to my everyday life. I am so grateful for his willingness to help whenever I approached him with a “problem”.

I would like to acknowledge my project leader, Mr. Bruce Brown, for his help with my experimental work and valuable suggestions on my project. Assistance was also provided by Dr. Dusan Sormaz with modeling work and by Dr. Yoon-Seok Choi with model verification, which are greatly appreciated. My gratitude is extended to other committee members, Dr. Michael Prudich, Dr. Howard Dewald and Dr. Michael Jensen, for their agreement to serve on my dissertation committee.

I would like to acknowledge Ms. Jing Huang and Mr. Danyu You for their help during the model development, especially in the development of FREECORP. I greatly appreciate all the staff and fellow students in this institute for their cooperation and assistance, which has made my stay an enjoyable experience. Special thanks go to the CCJIP sponsoring companies for their financial and technical support.

I would like to convey my heartfelt gratitude to my parents for their unconditional love and encouragement. A last but not least thanks go to my wife for her love, sacrifice and devotion to my family, without which I could have never made this far.

TABLE OF CONTENTS

	Page
Abstract.....	3
Dedication.....	6
Acknowledgments.....	7
List of Tables.....	11
List of Figures.....	12
Chapter 1: Introduction.....	17
Chapter 2: Literature Review.....	21
2.1 Passivation.....	22
2.2 Pit initiation.....	29
2.3 Pit propagation.....	43
Chapter 3: Research Objectives.....	58
Chapter 4: Mechanistic Model of Localized CO ₂ Corrosion.....	61
4.1 Introduction.....	61
4.2 Physico-chemical Processes Described by the Model.....	63
4.3 Physico-chemical Model.....	68
4.3.1 Chemical Reactions.....	68
4.3.2 Electrochemical reactions.....	72
4.3.3 Mass transport.....	75
4.3.4 FeCO ₃ precipitation.....	77
4.3.5 Pseudo-passivation.....	78
4.3.6 Depassivation and pit initiation.....	80
4.3.7 Repassivation and pit death.....	81
4.3.8 Pit propagation.....	82
4.4 Mathematical Model.....	84
4.4.1 Chemical reactions.....	84
4.4.2 Electrochemical reactions.....	89
4.4.3 Mass transport.....	104
4.4.4 FeCO ₃ layer Growth.....	110

4.4.5 Pseudo-passivation/repassivation.....	115
4.4.6 Pit initiation.....	118
4.4.7 Pit propagation.....	120
4.5 Numerical technique.....	124
4.6 Solving strategy.....	130
4.7 Model verification and parametric study.....	133
4.7.1 Uniform corrosion verification.....	134
4.7.2 Localized corrosion verification.....	137
4.7.3 Parametric study.....	146
4.8 Model limitations.....	152
5. Conclusions.....	153
References.....	156
Appendix 1: Derivation of the Equation for FeCO_3 layer Dissolution.....	168
Appendix 2: Derivation of the Exchange Current Density for Iron Oxidation.....	170
Appendix 3: Derivation of the Exchange Current Density for H^+ Reduction.....	173
Appendix 4: Determination of the Environmental Parameters Affecting Pseudo-Passive Current Density of Carbon Steel by Cyclic Polarization Technique.....	176
A4.1 Test Procedure and Test Matrix.....	176
A4.2 Test Results.....	178
A4.3 Test Result Analysis.....	183
Appendix 5: Modeling Pseudo-Passive Current Density of Carbon Steel in CO_2 Environment Based on Point Defect Model.....	185
A5.1 Introduction.....	185
A5.2 Model Development.....	187
Appendix 6: Open Source Model of Uniform $\text{CO}_2/\text{H}_2\text{S}$ Corrosion.....	196
A6.1 Introduction.....	196
A6.2 Theories of the Model.....	198
A6.3 Mathematical Model.....	200
A6.3.1 CO_2/HAc Corrosion.....	201
A6.3.2 H_2S Corrosion.....	210
A6.3.3 Film Growth.....	214
A6.3.4 Determination of $\text{CO}_2/\text{H}_2\text{S}$ Dominant Process.....	215

A6.4 Implementation of the Model.....	215
A6.5 Model Limitations.....	221
A6.6 Model Verification.....	222
A6.7 Conclusions.....	229

LIST OF TABLES

	Page
<i>Table 1.</i> The electrochemical parameters used for Tafel equation* in the previous model where the current density is calculated as $i = \pm i_o \times 10^{\pm \frac{E-E_o}{b}}$	94
<i>Table 2.</i> The electrochemical parameters used for Butler-Volmer equation* in the current model where current density is calculated as $i = i_o \left(10^{\frac{E-E_{rev}}{ba}} - 10^{\frac{E_{rev}-E}{bc}} \right)$	95
<i>Table 3.</i> Effect of factors on pseudo-passive current density	102
<i>Table 4.</i> Species commonly existing in the system of interest, and the corresponding diffusion coefficient at 25°C.....	106
<i>Table 7.</i> Test conditions for cyclic polarization test	177
<i>Table 8.</i> Test matrix for factorial design experiments	178
<i>Table 9.</i> Summary of the results for cyclic polarization tests.....	182
<i>Table 10.</i> Matrix used for performing factorial effect analysis	184
<i>Table 6.</i> Test conditions taken from open literature ¹³² for FREECORP verification.....	228

LIST OF FIGURES

	Page
<i>Figure 1.</i> Place exchange mechanism proposed by Sato and Cohen. ²⁴ M: metal ion; O: oxygen ion.....	23
<i>Figure 2.</i> Mechanism proposed by Marcus <i>et al.</i> ⁶⁶ for local breakdown of passivity driven by the potential drop at the oxide/electrolyte interface of an inter-granular boundary of the barrier layer. The effect of chlorides is shown.	40
<i>Figure 3.</i> Mechanisms proposed by Marcus <i>et al.</i> ⁶⁶ for local breakdown of passivity driven by the potential drop at the metal/oxide interface of an inter-granular boundary of the barrier layer. The effect of ion transport is shown: (a) predominant cation transport and (b) predominant anion diffusion.....	41
<i>Figure 4.</i> Illustration of corrosion process: FeCO ₃ layer formation leading to surface pH increases.....	65
<i>Figure 5.</i> Illustration of corrosion process: pseudo-passivation leading to potential increases.....	65
<i>Figure 6.</i> Illustration of corrosion process: depassivation leading to separation of anode and cathode and establishment of potential difference.	66
<i>Figure 7.</i> Illustration of corrosion process: Pit propagation.....	66
<i>Figure 8.</i> Illustration of corrosion process: FeCO ₃ re-precipitation if supersaturation of FeCO ₃ is sufficiently high.....	67
<i>Figure 9.</i> Illustration of corrosion process: Repassivation leading to pit death.	67
<i>Figure 10.</i> The Pourbaix diagram for Fe/CO ₂ /H ₂ O system with temperature 80°C, [Fe ²⁺]1ppm. Courtesy of T. Tanupabrungsun.....	80
<i>Figure 11.</i> Illustration of potential distribution in a galvanic cell. ϕ_i represents the solution potential drop across the double layer, E_i represents the electrode potential at different locations, E_{metal} represents metal potential.	84
<i>Figure 12.</i> Potential/current distribution predicted by the Tafel equation.....	92
<i>Figure 13.</i> Potential/current distribution predicted by the Butler-Volmer equation.	93
<i>Figure 14.</i> Potentiodynamic sweep on stainless steel and carbon steel. Test condition: T=25°C, pH=4.1, pCO ₂ =1 bar, stagnant solution.	99
<i>Figure 15.</i> Comparison of potentiodynamic sweep of stainless steel with polarization curves of carbon steel generated from the software. Test conditions: T=25°C, pH=4, NaCl=1%, stagnant solution.	100

<i>Figure 16.</i> Comparison of potentiodynamic sweep of stainless steel with Polarization curves of carbon steel generated from FREECORP. Test condition: T=25°C, pH=5, NaCl=1%, stagnant solution.	100
<i>Figure 17.</i> Illustration of computation domain and governing equation for mass transport simulation.....	110
<i>Figure 18.</i> Comparison of surface porosity of FeCO ₃ layer with different high-order schemes for convective term in Equation (95). Simulation condition: temperature 80°C, CO ₂ partial pressure 1 bar, liquid velocity 1m/s, pipe diameter 0.1m, bulk super saturation of FeCO ₃ about 0.5 and bulk pH 6.5.....	113
<i>Figure 19.</i> Comparison of corrosion rate with different high-order schemes for convective term in Equation (95). Simulation condition: temperature 80°C, CO ₂ partial pressure 1 bar, liquid velocity 1m/s, pipe diameter 0.1m, bulk super saturation of FeCO ₃ about 0.5 and bulk pH 6.5.....	113
<i>Figure 20.</i> Illustration of computation domain and governing equation for FeCO ₃ layer growth simulation.	114
<i>Figure 21.</i> Computation domain and governing equation with boundary conditions for electrostatic potential distribution in aqueous solution.....	123
<i>Figure 22.</i> Schematic of control volumes used for discretizing the governing equations for mass transport and FeCO ₃ layer growth. ¹³	126
<i>Figure 23.</i> Schematic of the 2-D control volumes used for discretizing governing equations for potential distribution.	129
<i>Figure 24.</i> Flow chart used in the localized corrosion model.....	132
<i>Figure 25.</i> Comparisons between model and experiments for 1 bar CO ₂ , 20°C and various pHs and velocities.	135
<i>Figure 26.</i> Comparison between model and experiments for FeCO ₃ layer forming condition at temperature 80°C, 0.53bar CO ₂ , pH 6.3 and bulk Fe ²⁺ concentration 50ppm, stagnant.	136
<i>Figure 27.</i> Comparisons between the model and the experiments for flowing FeCO ₃ layer-forming condition at temperature 80°C, pH 6.6, 0.53bar CO ₂ , 10ppm bulk Fe ²⁺ and 1000rpm rotation speed.....	137
<i>Figure 28.</i> Schematic illustration of the artificial pit unit used in Han <i>et al.</i> experiments (a) fully assembled artificial pit, (b) cutaway side view, (c) enlarged bottom view of cathode; center hole for anode, (d) detailed cross section view. ¹⁰⁵	139
<i>Figure 29.</i> Evans diagram depicting relationship of galvanic current and anodic current. Galvanic current is represented by I _{galvanic} and anodic current is symbolized by I _{corr} ^{couple}	140
<i>Figure 30.</i> Comparison of anodic current density and galvanic current density. Simulation conditions: Supersaturation of FeCO ₃ 0.3–0.9, T 80 °C, CO ₂ 0.53bar, pH 5.9–6.1, 1wt % NaCl, stagnant.	140

<i>Figure 31.</i> Comparison of galvanic current density between model and experiments for the conditions: Supersaturation of FeCO ₃ 0.3–0.9, Temperature 80 °C, CO ₂ 0.53bar, pH 5.9-6.1, 1wt % NaCl, stagnant.	142
<i>Figure 32.</i> Surface pH and potential as a function of time. Simulation conditions: Supersaturation of FeCO ₃ 0.3–0.9, T 80 °C, CO ₂ 0.53bar, pH 5.9-6.1, 1wt % NaCl, stagnant.	143
<i>Figure 33.</i> Comparison between the model and the experiment for the conditions: Supersaturation of FeCO ₃ 3–9, T 80 °C, pCO ₂ 0.53bar, pH 5.6, [NaCl] =1wt%, stagnant.	144
<i>Figure 34.</i> Comparison between model and experiments for the conditions: Supersaturation of FeCO ₃ 0.8–4, T 80 °C, CO ₂ 0.53bar, pH 5.9, 1wt % NaCl, 500rpm.	145
<i>Figure 35.</i> Anode surface pH vs. time for the condition: Supersaturation of FeCO ₃ 0.8–4, T 80 °C, CO ₂ 0.53bar, pH 5.9, 1wt % NaCl, 500rpm.	146
<i>Figure 36.</i> Effect of supersaturation on localized corrosion rate. Simulation conditions: temperature 80°C, CO ₂ partial pressure 0.52bar, 0.1 wt% NaCl, velocity 0.2m/s, bulk pH 6.	148
<i>Figure 37.</i> Potential difference between anode and cathode for two simulation cases with supersaturation 1 and 10 respectively. Simulation conditions: temperature 80°C, CO ₂ partial pressure 0.52bar, 0.1 wt% NaCl, velocity 0.5m/s, bulk pH 6.	149
<i>Figure 38.</i> Corrosion rate comparison for bulk liquid velocity at 0.5m/s and 1m/s. Simulation conditions: temperature 80°C, CO ₂ partial pressure 0.52bar, 0.1 wt% NaCl, bulk pH 6, bulk supersaturation of FeCO ₃ 10.	151
<i>Figure 39.</i> Galvanic current densities for solutions with different conductivity. Simulation conditions: pH 5.9, T 80°C, CO ₂ 0.53bar, FeCO ₃ supersaturation 2, 0.25m/s.	152
<i>Figure 40.</i> E-i diagram for Fe oxidation. i_{rev} can be obtained from the point (E ₀ , i ₀), the Tafel slope b _a and E _{rev}	172
<i>Figure 41.</i> E-i diagram for H ⁺ reduction. i_{rev} can be obtained from the point (E ₀ , i ₀), the Tafel slope b _c and E _{rev}	175
<i>Figure 42.</i> Cyclic polarization curve of C1018. Test conditions: T=60°C, pH=7, NaCl=0.2 mol/L.	178
<i>Figure 43.</i> Cyclic polarization curve of C1018. Test conditions: T=60°C, pH=8, NaCl=0.2 mol/L.	179
<i>Figure 44.</i> Cyclic polarization curve of C1018. Test conditions: T=80°C, pH=7, NaCl=0.2 mol/L.	179
<i>Figure 45.</i> Cyclic polarization curve of C1018. Test conditions: T=80°C, pH=8, NaCl=0.2 mol/L.	180
<i>Figure 46.</i> Cyclic polarization curve of C1018. Test conditions: T=60°C, pH=7, NaCl=2 mol/L.	180

<i>Figure 47.</i> Cyclic polarization curve of C1018. Test conditions: T=60°C, pH=8, NaCl=2 mol/L.....	181
<i>Figure 48.</i> Cyclic polarization curve of C1018. Test conditions: T=80°C, pH=7, NaCl=2 mol/L.....	181
<i>Figure 49.</i> Cyclic polarization curve of C1018. Test conditions: T=80°C, pH=8, NaCl=2 mol/L.....	182
<i>Figure 50.</i> Illustration of the Schottky(a) and Frenkel(b) defects by Gao. ¹³⁷	187
<i>Figure 51.</i> Original point defect model for carbon steel. ³⁸ Fe: Fe atom on a metal lattice site; Fe _{Fe} : Fe on Fe site in the oxide; Fe _i ^{x+} : iron interstitial in the oxide layer; O _O : oxygen ion in the oxide; V _{Fe} ^{x-} = Fe vacancy; V _O ⁻ = oxygen vacancy; Fe ^{Γ+} : metallic species in solution; FeO _{γ/2} : oxide barrier layer; FeCO ₃ : precipitated outer layer; k _i : reaction rate constant; BL: oxide barrier layer; OL: outer layer.....	188
<i>Figure 52.</i> Point Defect Model proposed in this work. Fe: Fe atom on a metal lattice site; Fe _{Fe} : Fe on Fe site in the oxide; O _O : oxygen ion in the oxide; V _{Fe} ³⁻ : Fe vacancy; V _O ²⁺ : oxygen vacancy; Fe ²⁺ : metallic species in solution; FeO _{3/2} : oxide barrier layer; k _i : reaction rate constant; BL: oxide barrier layer; S: solution.	189
<i>Figure 53.</i> Structure of the FREECORP software. ¹⁶	216
<i>Figure 54.</i> Screen shot for contributions of corrosive species in a CO ₂ corrosion case. Simulation conditions: temperature 20°C, pipe diameter 0.1m, velocity 1m/s, CO ₂ partial pressure 1bar, HAc 10ppm, pH 4.....	217
<i>Figure 55.</i> Screen shot for contributions of corrosive species in a H ₂ S corrosion case. Simulation conditions: temperature 20°C, pipe diameter 0.1m, velocity 1m/s, CO ₂ partial pressure 1bar, H ₂ S 10ppm, pH 4.....	218
<i>Figure 56.</i> Screen shot for the user input/output window for CO ₂ corrosion in FREECORP.	219
<i>Figure 57.</i> Screen shot for the user input/output window for H ₂ S corrosion in FREECORP.	220
<i>Figure 58.</i> Template for the inputs of a user-defined reaction in FREECORP.....	221
<i>Figure 59.</i> Comparison of experimental and FREECORP predicted polarization curves for temperature 20°C , partial pressure of CO ₂ 1bar, solution pH 4 and velocity 2 m/s. ¹⁶	223
<i>Figure 60.</i> Comparison between FREECORP predictions and experiments for different partial pressure of CO ₂ . Test condition: temperature 60°C, pH 5, pipe diameter 0.1 m. Data is taken from ICMT database. ¹⁶	225
<i>Figure 61.</i> Comparison of experimental and FREECORP predicted corrosion rate. Test conditions: temperature 60°C, pH 5, liquid velocity 1 m/s, partial pressure of CO ₂ 10 bar, pipe diameter 0.1m. ¹⁶	226

<i>Figure 62.</i> Comparison of FREECORP predictions and measurements for H ₂ S corrosion. Test conditions: temperature 80°C, pH 5, liquid velocity 1 m/s, pipe diameter 0.1m. Data is taken from icmt database. ¹⁶	227
<i>Figure 63.</i> Comparison of measured and FREECORP predicted corrosion rates under the conditions listed in Table 10. ¹⁶	228

CHAPTER 1: INTRODUCTION

Carbon steel is one of the most widely used engineering constructional materials due to its low cost and relatively good mechanical properties. This is particularly true in the oil and gas industry where transportation of products predominantly relies on pipelines spanning thousands of miles. In such cases, corrosion resistant alloys (CRAs) are not cost-efficient considering the large amount of materials involved in the construction. The use of carbon steels, when combined with other protective measures such as corrosion inhibitors, cathodic protection, non-metallic paints or CRA claddings, is the most common ways to satisfy the transportation needs of the oil and gas industry. Unlike CRAs, which are protected by the surface passive film spontaneously formed in the air, carbon steel surface is active in most corrosive media, which often leads to an unacceptably high corrosion rate. Clearly, the corrosion of carbon steels represents a major concern in their industrial applications. Uniform and localized corrosion are the two most common types of corrosion in carbon steel.² In most cases, uniform corrosion can be efficiently controlled by various corrosion inhibition methods as parts of a properly maintained corrosion management program. Localized corrosion, however, poses a much greater threat to the integrity of carbon steel pipelines. This is due to the stochastic and seemingly unpredictable induction period associated with localized corrosion and the fact that once initiation occurs, some pits can propagate at a much higher rate compared to uniform corrosion. Therefore, localized corrosion of carbon steel can significantly reduce the lifetime of pipelines, and increase the costs by increasing the frequency of replacing or repairing facilities and interrupting oil and gas production.

To combat corrosion, significant efforts have been made in the past few decades towards understanding the corrosion of carbon steel in the oil and gas industry. Thanks to past study, the mechanisms governing uniform CO₂ corrosion of carbon steel (especially without the presence of precipitates such as iron carbonate (FeCO₃) and other less soluble salts) are now well understood. As a result, a number of corrosion models have been developed to predict uniform CO₂ corrosion of carbon steel.³ These models typically exhibit good agreement in “bare” steel corrosion conditions, but they deviate from each other when the protective FeCO₃ layer is present on the steel surface.⁴ The difficulty of modelling FeCO₃ layer growth is the main cause for these prediction deviations. Different strategies have been proposed by various modellers to account for the FeCO₃ effect. Most models incorporate an empirical factor into the corrosion calculations; some determine FeCO₃ effect based on thermodynamic criteria while others simulate FeCO₃ layer growth kinetics. Although no consensus has been reached as to the strategy for modelling the FeCO₃ layer effect, a satisfactory corrosion prediction can be achieved if the models are carefully calibrated with good source of experiment data.

At present, most uniform corrosion models are proprietary and unavailable to the public. The corrosion prediction tool available to the corrosion community at large is limited to a few empirical and semi-empirical models, such as de Waard-Milliams model⁵⁻⁸, Norsok model^{9,10} etc., which were developed based on individual databases. Application of these models in users’ unique corrosion situations poses some degree of uncertainty as to the judgement of corrosion severity, particularly when the field conditions fall outside the parameter range used for model development. A mechanistic

model, however, can be extrapolated to a much wider range of parameters due to sound theoretical basis; therefore, it is able to provide corrosion prediction with a higher confidence level. As part of the efforts to provide the corrosion community with an additional tool for corrosion evaluation, a mechanistic model to predict uniform $\text{CO}_2/\text{HAc}/\text{H}_2\text{S}$ corrosion is developed in this project. This model, called FREECORP, is built exclusively based on publicly available information and the source code is open for maximum transparency. The model development is described in detail in Chapter 5.

Although uniform CO_2 corrosion can now be predicted with reasonable confidence, localized corrosion modelling remains as a more challenging topic. Despite extensive research carried out in the past with the aim of understanding localized corrosion of carbon steel, the mechanisms are still only partly understood. This is mainly due to the complexity associated with pit initiation; a number of factors (pH, flow disturbance, chloride concentration, etc.) have been proposed to induce pit initiation. However, the stochastic nature of pit initiation makes any attempts to validate the proposed theories difficult. In addition, the pits are typically inaccessible to common experiment equipment due to geometrical restrictions, making it difficult to examine the water chemistry inside the pit area, a property considered to be closely related to localized corrosion.

In recent studies performed in the Institute for Corrosion and Multiphase Technology at Ohio University (ICMT), an appreciable electrochemical potential increase has been observed for carbon steel immersed in CO_2 solutions after the build-up of an FeCO_3 layer.¹¹ The potential increase is attributed to the generation of magnetite

leading to pseudo-passivation of the carbon steel surface.¹² Due to the large potential difference between active surface and film covered surfaces, a galvanic coupling mechanism has been proposed for the propagation of localized corrosion of carbon steel.¹¹ Based on this mechanism, a transient mechanistic model is developed in the present study to predict localized CO₂ corrosion of carbon steel. The new model is built from the “ground-up” however it is based on a previously developed uniform corrosion model, MULTICORP, in which water chemistry, electrochemistry, mass transport and FeCO₃ layer formation are simulated according to corresponding physico-chemical laws^{13,14}. The unique phenomena for CO₂ localized corrosion, such as pseudo-passivation/repassivation, pit initiation and pit propagation are added into MULTICORP in this study to enable prediction of both uniform and localized CO₂ corrosion. With this model, water chemistry in the pit area, particularly pH near the pit surface, can be determined, and this can be utilized to facilitate the understanding of localized CO₂ corrosion of carbon steel.

This document is structured as follows: the literature review is given in Chapter 2; research objectives are laid out in Chapter 3; the localized corrosion model is presented in Chapter 4. Relevant equation derivations and experiment details, and are presented in the Appendix 1 to 5. A free mechanistic uniform corrosion model is described in Appendix 6. It should be noted that parts of Chapter 4 for the localized corrosion model and Appendix 6 for the uniform corrosion model have been presented in two published papers.^{15,16}

CHAPTER 2: LITERATURE REVIEW

The model discussed in this work is based on a galvanic coupling mechanism where pseudo-passivation is proposed to be present on the cathode surface. For any galvanic corrosion scenario, it is generally accepted that there are three important stages involved: passivation, pit initiation and pit propagation. In the passivation stage, steel surfaces are covered with passivating material(s) leading to a pronounced potential increase and a dramatic decrease in the corrosion rate. In the pit initiation stage, passive film is damaged in localized regions, leading to uncovered active surfaces with a lower potential, which are electrically coupled with a passivated surface with a higher potential. In the pit propagation stage, the potential difference between large passivated surfaces (cathode) and small active surfaces (anode) drives an electrical current between the two which makes the pit propagate. Under some conditions, however, the pit growth could be arrested due to repassivation of the active surface(s). Each of these stages is governed by unique mechanisms and must be treated separately.

A number of models have been developed in the past with the aim of simulating one or multiple stages of localized corrosion. These models, most of which have been developed for stainless steels and other passivating alloys, differ significantly in their underlying mechanisms. A literature review is given in this chapter for localized corrosion models in order to pave the path towards CO₂ localized corrosion modelling of carbon steel.

2.1 Passivation

Passivation is characteristic of a substantial corrosion current (rate) drop resulting from a small increase in potential. The passive film formed on metal surface prohibits the metal from actively reacting with a surrounding corrosive medium, and therefore significantly reduces the corrosion rate. Passivation used to be considered a unique feature for CRAs in the early stage of localized corrosion research. In recent years, it has been discovered that passivation also takes place on carbon steel surfaces under appropriate conditions^{12,17-22}.

Fleischmann and Thirsk²³ derived generic equations for calculating transient current in the initial stage of metal passivation. By assuming cylindrical-shaped crystals, the equations were developed to simulate two scenarios of passivated crystal growth, namely growth of the discrete passivated crystal centers and two-dimensional growth of mono-layer passivated crystal centers. The rate constants in the equations can be obtained by making short-period potentiostatic measurements at the initial stage of passivation. It was claimed that the difference in the two models relies on the assumption of crystal growth due to a single nucleus vs. a large number of nuclei. A distribution function is built in the model equations to account for random distribution of all possible forms of crystals center overlapping.

Sato and Cohen²⁴ developed an equation to calculate the passive iron growth kinetics in neutral solutions. The model is proposed based on the assumption of “place-exchange”, which suggests that growth of passive oxide film is a result of the oxygen atom from OH⁻ in water replacing the iron atom in the metal substrate. This process is

schematically illustrated in Figure 1. At steady state, the number of iron atoms transferred from the metal substrate are balanced by oxygen atoms moving from the solution into the oxide film, leading to a constant thickness of passive film. The equation takes the form of an Arrhenius-type equation, where passive current density is a function of a rate constant, potential, activation energy of Fe-O exchange and passive film thickness. The developers accentuated that this mechanism would lead to the activation energy increasing with passive film thickness, which could change the mechanism at some specific film thickness.

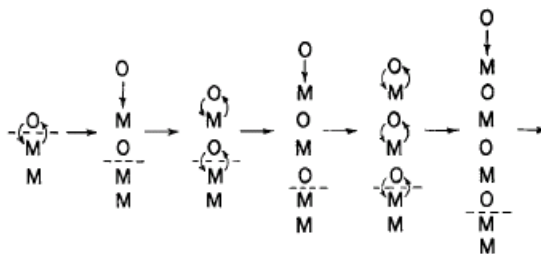


Figure 1. Place exchange mechanism proposed by Sato and Cohen.²⁴ M: metal ion; O: oxygen ion.

Griffin²⁵ suggested a simple kinetic model to describe the passivation process. In this model, the passivation process was considered to be composed of two subsequent steps, namely, metal oxidative hydrolysis to form cations adsorbed on the metal surface, followed by cation dissolution into the solution. In the model, passivation is considered to occur when the rate of cation dissolution is slower than that of cation formation. The passive film growth kinetics is described as a function of the rate constants associated with cation formation and dissolution, together with cation coverage on the metal surface

and the Tafel coefficient of metal oxidation. The model equation was shown to be able to simulate the current-potential behaviour in the active-passive transition region.

Zakroczymski *et al.*¹⁷ found that passive film formation on iron occurred in two steps. In the initial step which lasted only a few seconds, passive film thickness reached 60-80% of its final value. Iron oxide/hydroxide, FeOOH, along with significant amount of water, was found within the passive film. The amount of water decreased as the passivation process continued, resulting in a much denser passive film in the second step, where metal was much more resistant to pitting corrosion. The presence of water was thought to play a significant role in passivity breakdown, as the continuous phase of water provides a path for Fe²⁺ and Cl⁻ to move through the passive film and also allows hydrolysis reaction of Fe²⁺ to occur. The thickness of the passive film, on the other hand, was not found to be important in passivation process.

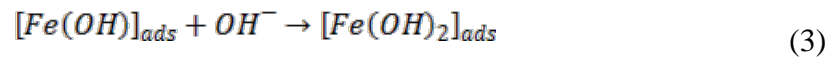
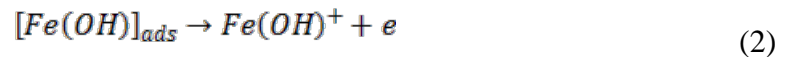
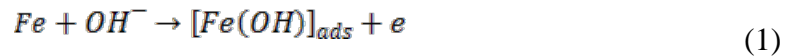
Sarasola *et al.*²⁶ presented a layer-pore resistance model to explain the experimentally-observed passivation of iron in 1M KOH solution in the cyclic polarization test. In this model, passive film growth rate is calculated as a function of polarization scan rate, passive film consumption rate and the total system resistance. The total resistance is attributed to three components: active electrode surface, electrolyte and passive film. The authors referred to the work of Devilliers *et al.*²⁷ and suggested that the active and passive behavior of iron polarization can be obtained using the model by assuming the first and second orders of passive film consumption respectively. As shown by the authors, this model is capable of simulating the current-potential behaviour in the passive region for iron in KOH solution.

Macdonald and his colleagues proposed a so-called 'Point Defect Model' for passive film growth in a series of published papers, initiating at the beginning of 1980s²⁸⁻³¹. In this model, passive film growth was hypothesized as a result of motions of various defects (vacancies and/or interstitials) within the passive film. The whole process was mathematically described by five equations accounting for five reactions that occur at metal/film and film/solution interfaces. Vacancies/interstitials are considered participants of these reactions. The most important assumptions made in this model include:

- Passive film is composed of metal oxide, $\text{MO}_{x/2}$ where high concentrations of defects, particularly vacancies, are present. Passive film growth is attributed to the transport of these defects.
- The metal/passive film and passive film/solution are in electrochemical equilibrium.
- Electric field strength is independent of film thickness. This assumption has been verified by experimental evidence, as the potential drop across the passive film was found to be linearly changed with passive film thickness.³²
- Passive film/solution interface potential is linearly related to pH and applied potential.
- It was argued that this model is consistent with the well-established experimental observations related to passivation.³² These observations include:
- A passive film has a bi-layer structure with a highly disordered barrier adjacent to the metal substrate and a less protective outer precipitated layer;

- The passive film thickness and logarithmic passive current density are linearly varied with the applied potential;
- The inner passive film grows into the metal substrates while the outer passive film grows outwards the solution.
- Due to the capability of explaining the above-mentioned experimental results, the Point Defect Model is considered to be one of the most successful passivation models. Although originally developed for aluminium alloys, the theories embedded in this model can be expanded to other metals such as carbon steel. Proper electrochemical experiments need to be conducted in order to obtain multiple constants in the model equations suitable for the materials of interest.

Hibbert and Murphy³³ developed a minimal kinetic model to simulate corrosion and passivity of iron. The model is based on the mechanisms proposed by Epelboin³⁴ as shown below:



By expressing the rates of generation/consumption of each involved species, $[Fe(OH)]_{ads}$, $[Fe(OH)_2]_{ads}$ and $[OH^-]$, as functions of rate constant, surface coverage ratio and concentrations, a current-voltage relationship can be obtained. The model equations are able to predict the current variations in the full range of potential, covering active, passive and active-passive transition regions. A linear stability analysis indicated that the model was stable in the active and passive regions of the current-potential curves and

became unstable in the transition region, which resulted in a periodic current-time variation in this region. This indicates that the model requires external perturbation to trigger passivity.

Pyun and Hong³⁵ developed a model to simulate the passive film growth kinetics by taking into account Fickian diffusion and migration of cation vacancy in the passive film. The current density associated with passive film growth is calculated as a function of electric field strength and film thickness, which evolves with time. In contrast to Macdonald's model where electric field strength is independent of applied potential, this model suggests an increasing electric field strength with applied potential. However, no experimental verification was given for the proposed functions, making the model less convincing compared to Macdonald's.

Meakin *et al.*³⁶ took a probabilistic approach to simulate passivation and depassivation of metals subject to localized corrosion. A 2D square-lattice model was developed in their work where sites of lattice are represented by four different states, namely: unreactive fluid or corrosion product, corrosive fluids or particles, reactive metal and unreactive passive metal. This model assumes a diffusion-limited corrosion process. Passivation is considered to be a spontaneous random event characterized by a passivation rate constant. At each time step, a randomly generated number between 0 and 1 is compared with a passivation probability function; a smaller random number would lead to one of the reactive metal sites converted to a passive metal site, and vice versa. Despite a lack of physical representation of the process, the model was shown to be able to simulate some characteristic features of localized corrosion, including pit propagation,

pit death and current fluctuation. However, the authors also stressed that the model cannot represent the real corrosion system, as the passivation rate constant, which is a time-dependent variable, is taken as a constant in the model.

Reis *et al.*³⁷ proposed a stochastic model to simulate corrosion and passivation of a metal based on the scaling theory. This model was designed to simulate the incubation period during which transition from slow passivation to fast pit propagation occurs. The model is simulating a 2D lattice where each site of lattice is represented by one of the six possible states: bulk, reactive or passive metal and neutral, basic or acidic solution. In this model, passivation, dissolution of passive film and spatially separated electrochemical reactions are described by certain probabilistic rules. The model predicts the average radius of passive film dissolution and average incubation time. It suggests that the average radius decreases with the spatially separated electrochemical reaction rates and dissolution rates in acidic media, but increases with the diffusion coefficients of H^+ and OH^- in solution. The average incubation time is determined by the time characteristic of slow passive film dissolution in neutral solutions until significant pH inhomogeneities are established inside the pit. The model suggests that the average incubation time linearly increases with the rate of dissolution.

Camacho *et al.*³⁸ developed an impedance model based on the Point Defect Model to calculate the steady-state passive current density on carbon steel surfaces in CO_2 environments. The model suggests that passive current density is attributed to the movements of cation interstitials, cation vacancies and H^+ under applied potentials. The passive film is considered to contain a bi-layer structure; the outer layer is the

precipitated FeCO_3 , while the inner layer is the defective magnetite. Based on the EIS experiments, the inner layer was found to contribute most of the electric resistance to current transport.

In this project, a mechanistic approach is preferred to simulate the pseudo-passivation process as stochastic models are not able to cope with the change in parameters as the passivation process proceeds. Due to the wide acceptance and generic nature of the Point Defect Model, it is used in this project to calculate the pseudo-passive current density of carbon steel in CO_2 environments. The various parameters needed in the model are obtained by calibrating against experimental measurements for galvanic current density, as presented in Chapter 5.

2.2 Pit initiation

Pit initiation manifests itself as a process of localized passive film removal leading to depassivation of the metal surface. Two different strategies are usually employed to simulate pit initiation, namely *a priori* and *a posteriori* approaches. According to Papavinasam³⁹, “the *a priori* approach emphasizes the inherent microscopic defects on the metal surface such as inclusions, grain boundaries, and scratches. The *a posteriori* approach emphasizes the non-uniformity on the metal surface that becomes visible after a passive metal is placed in a corrosive media.” This definition implies that the former approach assumes inherent imperfection of the passive materials while the latter assumes induced imperfection due to the corrosion process. In essence, the former is the deterministic approach while the latter is the stochastic approach.³⁹

As opposed to passivation and pit propagation, pit initiation appears to occur in a more-or-less random fashion and exhibits a large degree of scatter with regard to when and where it takes place. The often seemingly-oscillatory phenomenon has led many researchers to consider this process as stochastic in nature, and therefore to seek a statistical approach in order to explain the phenomenon. This approach formulates the pitting corrosion process with some probabilistic functions. However, the nature of this process is still subject to extensive debate. For example, Sharland⁴⁰ argued that the oscillations of pit initiation could be described by a set of differential equations for which multiple steady-state solutions exist. The presence of multiple solutions is the mathematical answer for the stochastic nature of pit initiation. According to Sharland⁴⁰, a differential equation system involving at least three variables would be necessary for a complete description of the process.

Oldfield and Sutton⁴¹ developed a mechanistic model for crevice corrosion. Four stages are identified in the model leading to stable crevice corrosion propagation. The breakdown of the passive film is preceded by depletion of oxygen and increased acidity and chloride concentration inside the crevice. In this model, passive film breakdown is considered a result of the formation of a critical crevice solution (CCS) in which pH and chloride concentration is such that the passive film can be destroyed. The composition of the alloy and its associated CCS, passive current density, bulk Cl⁻ concentration and crevice geometry are identified as the major parameters determining passivity breakdown.

Galvele⁴² developed a pitting corrosion model where passive film breakdown is assumed to be a consequence of local acidification results from metal ion hydrolysis. The model proposed a critical “ x_i ” value (representing the distance toward pit bottom times the current density) beyond which critical pH is reached and a pit is initiated in cases where the potential is above the pitting potential. The pitting potential was calculated as a linear function of logarithmic Cl^- concentration.

Hebert and Alkire^{43,44} proposed a deterministic model to simulate the initiation of crevice corrosion of aluminum based on their preceding experimental work. This model assumes that crevice corrosion initiates when the concentration of metallic species inside the crevice exceeds a certain critical level, leading to significant potential drop inside the pit. The authors argue that crevice acidification due to hydrolysis and accumulation of Cl^- inside the crevice are not the direct cause of passivity breakdown, as crevice acidification occurs long before crevice corrosion initiation and negligible Cl^- accumulation is measured before the initiation. The exact mechanism through which metallic species induce passivity breakdown was not identified in the paper. The experimentally determined critical concentration was used in the model to trigger pit initiation. A set of partial differential equations describing diffusion and migration of the involved species are solved in the model as a function of time; the time at which metallic species concentration at the crevice surface exceeds the predefined critical concentration is considered the time needed for crevice corrosion initiation.

Okada⁴⁵ proposed a model of pit initiation based on perturbation theory. This model assumes that pit initiation is caused by perturbation of concentrations of aggressive

ions and of an electrical field. The linear stability theory applied to a system with a passive film held at a constant potential indicates that disturbance of the system would lead to local accumulation of aggressive species on the passive film surface, and the consequent local increase of dissolution rate. The perturbation can be characterized by a wave length. Above a critical wave length, the perturbation keeps increasing with time, causing more and more aggressive species to be absorbed on the passive film surface and pass through the passive film. This eventually results in pit initiation. Below the critical wave length, however, perturbation decreases with time, and the passive film tends to dissolve uniformly; therefore no pits are generated. Okada⁴⁵ argues that whether the perturbation increases with time or not, determines the occurrence of pitting. In this model, pit initiation is treated as a probabilistic rather than a deterministic process.

Williams *et al.*⁴⁶ developed a stochastic model for pitting corrosion of stainless steels. The model was built based on nucleation-type theory together with statistical methods. The modeling strategy was inspired by that adopted for electro-crystallization. In the model, the pitting process is simulated as a series of events that are randomly distributed over the metal surface with time. Each of these events induces a local current, which is increased over time following certain predefined rules. The total current is obtained by summing up all local currents. The events have the following common features: events are triggered by a frequency; events bear a probability to die; events that last longer than a critical age do not die; and each event has an induction time during which the local current does not change with time, but the event could die. The model defines a critical pH below which pit initiation occurs. The main hypotheses made in the

model include: that pit initiation requires the existence and persistence of acidity and potential gradients on the scale of the metal surface roughness; that pit initiation is triggered by the fluctuation of acidity and potential gradients in the boundary layer; that the fluctuations of acidity and potential gradients are attributed to the variation of boundary layer thickness, which is defined by the authors as the summation of the hydrodynamic boundary layer and the surface roughness; and that a stable pit is obtained when the pit depth exceeds a critical value related to surface roughness.

Dawson and Ferreira⁴⁷ postulated a semi-stochastic model for pitting corrosion of stainless steels. The model consists of both mechanistic and stochastic components. Pit initiation is modeled as an electro-crystallization process in which chloride ion plays a major role by forming soluble intermediates adsorbed on the metal surface. The kinetic competition between the formation of non-passivated species $[\text{MOMOHCl}]_{\text{ad}}$, $[\text{MOMCl}]_{\text{ad}}$ and passivated species $[\text{MOOH}]_{\text{ad}}$, $[\text{MOMOH}]_{\text{ad}}$ determines whether a pit propagates or dies. Passive film rupture is seen as a natural process that is enhanced by an increase of potential and an accumulation of aggressive chloride ions. Although passive film formation and metal dissolution are deterministic in nature, the crack-heal process is considered to be a stochastic process. In the model, the transition of the initial passivity breakdown to stable pit propagation is determined by potential, Cl^- ion concentration and its diffusion through the initial crack and the growing pit. The model indicates that the effect of adsorbed intermediates on metal dissolution is intensified with increasing potentials.

Macdonald *et al.*⁴⁸ proposed a deterministic strategy in conjunction with a statistical approach to simulate the stochastic nature of passivity breakdown. The model is built based on the mechanistic Point Defect Model. According to the Point Defect Model, the passivity breakdown is induced by cation vacancies concentrated on the passive film/metal interface. It was argued that this could occur when the movement of cation vacancies from the passive film/solution interface is faster than cation vacancy consumption on the passive film/metal interface. The pitting potential is mechanistically determined as a function of a number of parameters such as electric field strength within the film, the diffusivity of cation vacancies, molar volume of the cation vacancies and temperature, etc. A normal or log-normal random function is applied to the diffusivity of cation vacancies, which results in normal or log-normal distribution in pitting potential. By using normal or log-normal distributed diffusivity and the standard deviation determined from pitting potential distribution, a distribution function is derived for induction time of pit initiation. It was shown that a quantitative agreement was achieved between experimentally-observed and model-predicted induction time.

Bardwell and Macdougall⁴⁹ proposed that the composition, thickness and stability of a passive film on an iron surface in a Cl⁻-containing borate solution is related to the total anodic charge passing through the passive film during film formation, which is a function of passive film thickness, rather than potential. Pit initiation takes place only if the passive film reaches a critical thickness leading to passivity breakdown.

Baroux⁵⁰ developed a model to predict pit nucleation rate based on the potentiodynamic and potentiostatic experiments conducted on two types of 304 stainless

steel in neutral aqueous solutions. According to the model, pit initiation is a successive process involving a deterministic stage, followed by a probabilistic stage. The deterministic stage leads to passivity breakdown, which can be characterized by an induction time. However, the exact mechanism that causes passivity breakdown was not identified by the author. Instead, a number of possible mechanisms were proposed, including accumulation of cation vacancies on metal substrate or on passive film, acidification of the solution due to hydrolysis, and soluble complex formation by chloride, etc. All of these mechanisms are consistent with experimental results if different values of parameters are used in the model equation. Baroux⁵⁰ argues that multiple pitting mechanisms could be involved in a pit nucleation process with one being kinetically dominant. The probabilistic stage of pit initiation leads to pit stabilization, which is considered to be probabilistic in nature and can be characterized by a pitting probability.

McCaffery⁵¹ considered the passivity breakdown as a process in which aggressive ions (such as Cl^-) and inhibitive ions (such as CrO_4^-) compete for sites for adsorption. Passive film breakdown happens when the ratio of coverage of aggressive ions to inhibitive ions exceeds a critical value, determined to be around 1.9. This value is in agreement with the experimental results from x-ray photoelectron spectroscopy. A model was developed to simulate the competitive adsorption of the aggressive and inhibitive ions on a metal surface by assuming Temkin isotherm for both ions. The model predicts the same critical coverage ratio for both pitting and crevice corrosion cases, based on which the author suggests that passivity breakdown in pitting and crevice corrosion are governed by the same mechanisms. The model was shown to predict the linear decrease

of pitting potential with logarithmic activity of chloride, which is consistent with experimental observations.

Nagatani⁵² proposed a probabilistic 3D model to simulate the pit size distribution on a metal surface. The model assumes that the metal dissolution rate is controlled by diffusion of anions from the bulk solution towards the metal surface. The concentrations of anions are assumed to follow the Laplace equation under quasi-steady state conditions. The model predicts a percolation threshold below which isolated pits dominate the pitting pattern, and the pit distribution follows a proposed dynamic scaling function.

Shibata and Ameer⁵³ studied the pit initiation of passive zirconium film formed in 1N H₂SO₄ at different potentials. Stochastic models were developed to simulate the pit initiation process. The pit initiation process is modeled as a series or parallel or combination of pit birth-and-death stochastic process. A number of pit survival probability functions are postulated as a function of pit induction time, pit generation rate and/or repassivation rate depending on different mechanisms. The appropriate governing mechanism is determined by fitting the distribution for pit initiation time into a specific function.

Xu *et al.*⁵⁴ postulated that passive film breakdown happens when electrostatic pressure at film/solution interface of some local sites is higher than the compressive film strength. A deterministic mathematical model was developed relating the electrostatic pressure with electric field strength, film thickness and surface energy of the film/metal interface. It is argued that the aggressive ions such as Cl⁻ can reduce the surface energy of film/metal interface and therefore facilitate passivity breakdown. In their model, pit

initiation is considered as a repeated generation-cessation process due to repassivation of the pit until a critical depth of pit is reached, where pit bottom is within the active region of the polarization curve and the pit is stabilized. It is claimed that this hypothesis is consistent with the experimentally observed lace-like pattern inside the pit.

Lillard and Scully⁵⁵ developed a deterministic model to determine the inception of crevice corrosion by combining the concepts proposed in Oldfield-Sutton's⁴¹ and Xu-Pickering's⁵⁴ models. The former emphasizes the development of a critical crevice corrosion solution where H^+ and Cl^- concentrations are sufficiently high due to depletion of oxygen and hydrolysis of metallic ions inside the crevice. The latter focuses on the solution resistance between the crevice mouth and bottom which maintains the crevice bottom at the active dissolution region. Potential and current distributions are obtained by solving the Laplace equation for potential inside the crevice. A set of artificially-set criteria is then used to determine whether a pit can initiate at specific locations along crevice walls. The criteria states that for a pit to initiate, three conditions must be satisfied: potential is below passivation (Flade) potential, dissolution rate is higher than $10\mu A/cm^2$ and pH reaches -0.46 at the locations where the first two criteria are met.

Darowski and Krakowiak⁵⁶ analyzed the pitting potential distribution of steels predicted by various stochastic models, which were developed based on potentiodynamic measurements. They argue that different pitting potential distribution functions are derived due to the fact that the functions are obtained under different threshold current values. It has been shown that the pitting potential is a function of the square root of the threshold current density. They propose a new method to obtain the pitting potential

distribution by extrapolating the threshold current density to 0. It is claimed that the extrapolation method would not change the characteristics of the distribution function.

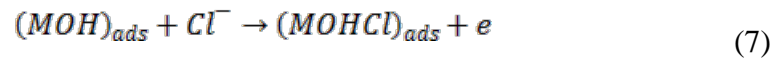
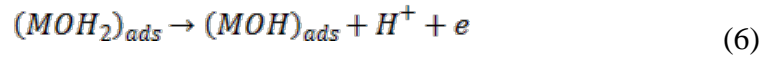
Cheng *et al.*⁵⁷ studied the pit initiation of A516-70 carbon steel based on statistical analysis of current and potential noise. It was shown that the pit initiation rate can be described as:

$$\lambda(t) = \lambda(0)\exp(at), 0 \leq t < \tau \quad (4)$$

$$\lambda(t) = \lambda(\tau)\exp(-bt), t \geq \tau \quad (5)$$

Where $\lambda(0)$ and $\lambda(\tau)$ are the pit initiation rate at time 0 and the traverse time respectively. The a and b are chloride concentration dependent constants. The average peak pitting potential is a function of logarithmic Cl^- concentration. The role of Cl^- is considered to increase the chance for passivity breakdown rather than inhibit repassivation.

Szklarska-Smialowska⁶¹ proposed that pit nucleation is initiated due to electric breakdown. It is argued that a current increase is induced in passive film by the movement of electrons due to the existence of large electric field within the oxide conduction band. When the current reaches a critical value, a local heating is produced and results in passive film breakdown. Two mechanisms are considered to contribute to current increase. The first one suggests that electrons injected from the electrolyte are accelerated and multiplied in the oxide conduction band, a process called avalanche ionization. The second one is quantum mechanical tunneling, where the binding electrons in the valence band are separated by electric field and traverse the energy gap that is otherwise unachievable. The effect of Cl^- is considered through the following reactions which contribute electrons to passive film:



Marcus *et al.*⁶⁶ proposed a model to simulate the passivity breakdown that predominately occurs on the inter-granular boundaries. The mechanisms considered include: local thinning and dissolution of oxide film; metal voiding on metal/passive film interface induced by cation diffusion; and mechanical breakdown by particle growth on metal/passive film interface induced by anion diffusion. Figure 2 schematically shows the first mechanism with and without Cl⁻. Figure 3 demonstrates the second and third mechanisms respectively. The straight lines on the top of each illustration signify the potential distribution in the system. Clearly, potential constantly redistributes as the pit initiation process advances.

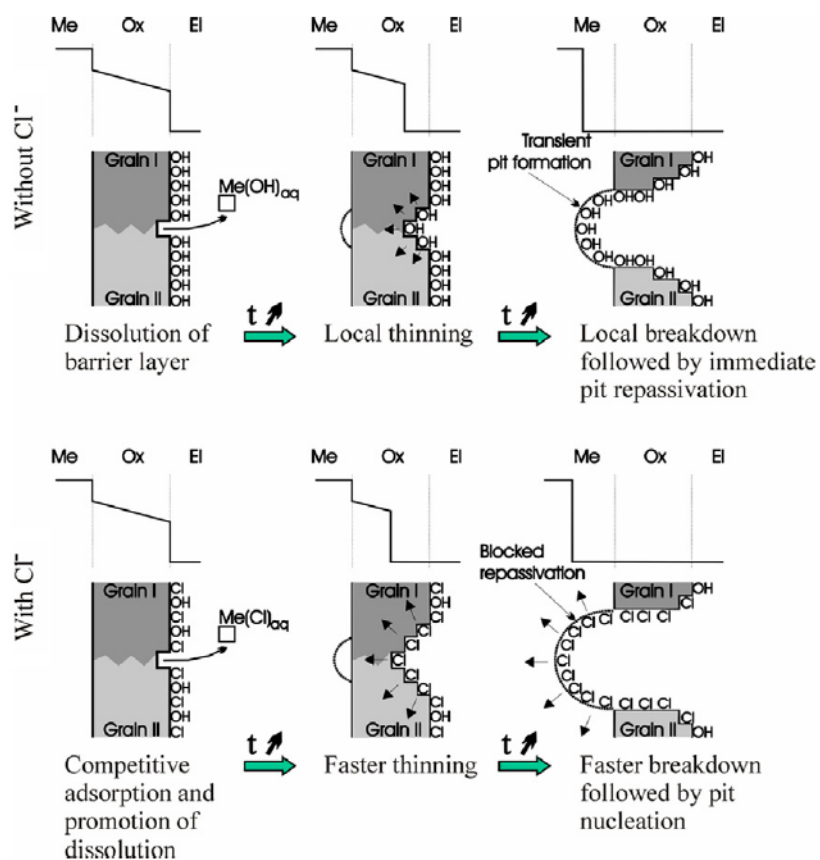


Figure 2. Mechanism proposed by Marcus *et al.*⁶⁶ for local breakdown of passivity driven by the potential drop at the oxide/electrolyte interface of an inter-granular boundary of the barrier layer. The effect of chlorides is shown.

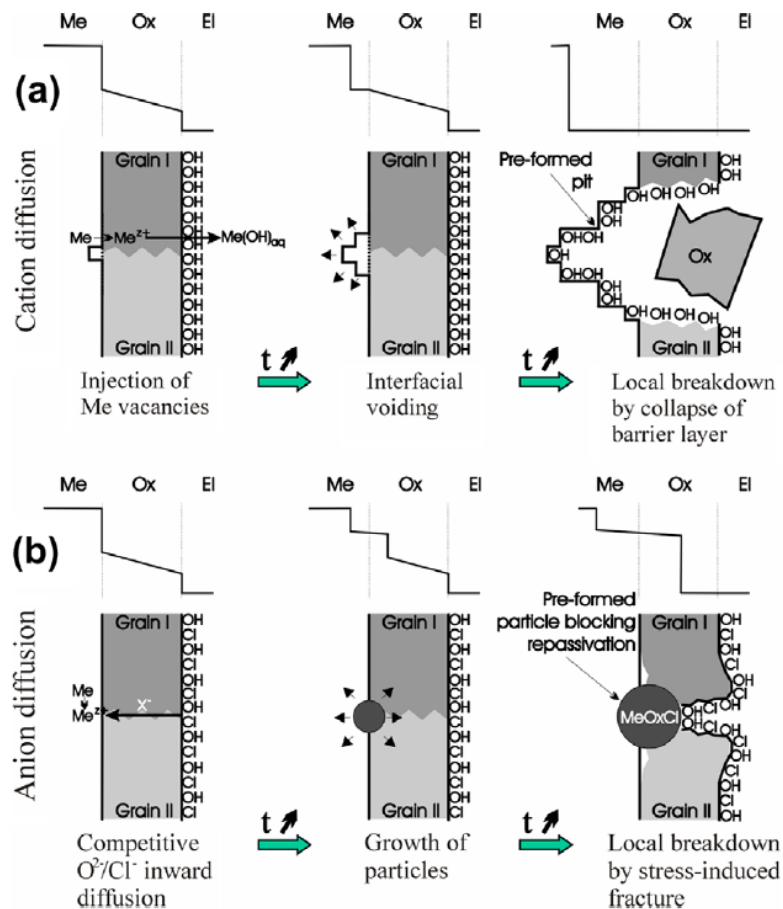


Figure 3. Mechanisms proposed by Marcus *et al.*⁶⁶ for local breakdown of passivity driven by the potential drop at the metal/oxide interface of an inter-granular boundary of the barrier layer. The effect of ion transport is shown: (a) predominant cation transport and (b) predominant anion diffusion.

Schmitt *et al.*⁵⁸ proposed a deterministic model to predict the initiation of flow-induced localized corrosion (FILC). The model compares the kinetic energy exerted on a critical impact surface area by turbulence with FeCO₃ fracture energy. The turbulent kinetic energy is evaluated in terms of near wall shear stress. When the former is larger than the latter, development of microcrack growth is facilitated, leading to onset of

FILC. This mechanism is challenged by Yang⁵⁹, who experimentally showed that the strength of FeCO₃ layer is higher than wall shear stress by several orders of magnitude.

Ergun and Akcay⁶⁰ investigated the pitting potential of 1018 carbon steel as a function of pH, chloride concentration and temperature using potentiodynamic sweep. The Box-Wilson experiment design concept was adopted in the experiments. By analyzing a total of 20 experiments, an empirical equation in the form of polynomial expression was developed, which relates the pitting potential with investigated parameters. The equation suggests that the interactions between temperature/pH and pH/Cl⁻ concentration are important factors in determining pitting potential.

Nyborg and Dugstad⁶² experimentally investigated the mesa attack of carbon steel in flowing CO₂ conditions using in-situ video technique. The initiation of mesa-type defect is proposed to be related to the competition between corrosion and FeCO₃ layer precipitation for available metal surface. It is argued that when the ratio of the precipitation rate and the corrosion rate is below a certain level, the void on the metal surface created by the corrosion process will not be able to be filled by FeCO₃ precipitates. The void underneath the FeCO₃ layer jeopardizes the mechanical strength of the film, which can then be removed by hydrodynamic forces. A model developed by Nešić *et al.*⁶³ is shown to be able to provide the quantitative information required for determination of the onset of pit initiation based on the proposed mechanism.

Xiao⁶⁴ developed a 2D stochastic model to simulate the localized corrosion process of carbon steel. Uniform corrosion rate and surface scaling tendency were used as the major inputs for calculation of the probability function, which was originally

proposed by Van Hunnik and Pots.⁶⁵ The model gives reasonable simulation in pit shape; however, no mechanistic information can be provided by the model due to the lack of mechanistic background.

From the literature review presented in this section, it can be seen that the mechanisms of pit initiation are still unclear despite the significant research efforts made in this area. Various models have been developed based on different proposed mechanisms, such as electric field, pH, chloride, passive film thickening, flow or a combination of these factors. A clear pit initiation model cannot be proposed before a consensus is reached as to the determining factor responsible for pit initiation, and the deterministic vs. probabilistic nature of pit initiation.

2.3 Pit propagation

Pit propagation is one of the most active research areas in the field of localized corrosion modelling. Given the corrosive environment favors pit propagation, a pit can penetrate into the metal at a high rate. The rate of pit propagation directly determines the service life of pipelines. Most pit propagation models invoke a galvanic coupling mechanism. In the context of galvanic corrosion, pit propagation rate is dictated by the potential/current distribution between anode and cathode. Due to the existence of solution resistance, potential is non-uniformly distributed over the metal surface, leading to varied anodic dissolution rates on different parts of the anode. Obviously, the solution resistance effect must be taken into account in pit propagation modelling in order to achieve reasonable predictions.

The earliest mechanistic model for localized corrosion propagation is probably the one proposed by Pickering and Frankenthal.⁶⁷ In their work, a 1D model was developed to simulate the potential and current distribution in a cylinder-shaped pit with passivated walls and an active pit bottom. In this model, a single electrochemical reaction, metal oxidation, is considered on the pit bottom. Diffusion and electro-migration are considered to drive mass transport of metal ions. Chemical equilibrium is assumed in the model. The simple geometry and simple physics allow them to derive the analytical solutions for concentration and potential distributions as functions of pit depth. Although this model over-simplifies the complexity of localized corrosion, the basic principles involved are widely adopted in the more complicated models developed thereafter.

Alkire *et al.*⁶⁸ developed a mechanistic model to investigate the effect of electrolyte conductivity on galvanostatic and potentiostatic experiments conducted in an artificial pit with certain dimensions. The simulation is achieved through modeling of transient Fickian diffusion of salt within the artificial pit, as shown in equation (8):

$$\frac{\partial c(y,t)}{\partial t} = D \frac{\partial^2 c(y,t)}{\partial y^2} \quad (8)$$

Where c is concentration of salt, D is diffusion coefficient, t is time and y is pit depth. By considering the neutral salt molecule as a whole, modeling of the electro-migration effect is avoided. The salt concentration is assumed to be under the saturation limit, so it can be assumed that no precipitation would occur. The pit bottom is assumed to be flat and smooth during the corrosion process, which is claimed to be valid for short time tests. Only one electrochemical reaction, metal dissolution, is considered in this model. Current density associated with metal dissolution is converted into the flux of salt and is used as

the boundary condition for the governing mass transport equation. Four components are considered in calculating the potential between working electrode and reference electrode: charge transfer resistance, concentration difference resistance, solution resistance within the pit and solution resistance over the pit mouth.

Alkire and Siitari⁶⁹ developed a model to simulate current distribution along the wall of a long narrow pit. In this model, anodic reaction is assumed to occur only at the pit bottom, while cathodic reaction occurs along the pit wall. Two equations (equation (9) and (10)) are derived for potential and concentration distributions from Ohm's law and Fick's law, respectively. Metal dissolution and H⁺ reduction are the only electrochemical reactions considered, the kinetics of which are assumed to follow Tafel behavior. Mass transport is attributed only to molecular diffusion, while convective flow is neglected due to geometric restrictions. The constriction for current flowing into the crevice is implemented. The model results indicate that cathodic reaction can occur inside the narrow pit even though the bulk solution contains a low H⁺ concentration.

$$\kappa \frac{d^2 \phi_s}{dx^2} = ai_0 \frac{c}{c^o} \exp \left\{ \frac{-\alpha_c nF}{R_g T} (V - \phi_s) \right\} \quad (9)$$

$$D \frac{d^2 c}{dx^2} = \frac{ai_0 c}{nFc^o} \exp \left\{ \frac{-\alpha_c nF}{R_g T} [V - \phi_s] \right\} \quad (10)$$

Where i_s : current density in the solution; ϕ_s : potential in the solution; κ : solution conductivity; α : ratio of surface area over volume; i_0 : exchange current density; c, c^o : local and reference concentration of species; D : diffusion coefficient; α_c : transfer

coefficient; V : potential of metal; n : electrons involved in electrochemical reactions; F : Faraday constant; R_g : universal gas constant; T : temperature.

Harb and Alkire⁷⁰ developed a 2D mechanistic model for pitting corrosion of nickel alloy (Ni) in a stagnant 0.5M NaCl solution at steady-state. Five species are taken into account in the model (NiCl^+ , NiCl_2 , Ni^{2+} , Cl^- , Na^+). Mass transports of involved species are simulated for constant applied potentials. In this model, mass transport is contributed only by molecular diffusion and electro-migration. Chemical equilibrium is assumed, which gives zero generation or consumption rates of the species. A hemispheric pit and the solution well beyond the pit are used as the computation domain. The simulation reveals significant concentration gradients outside the pit indicating the importance of solution resistance both inside and outside the pit.

Based on the stagnant pitting model, Harb and Alkire⁷¹ developed a second model by including the effect of convective flow. In this model, in-situ velocities are required in order to solve the mass transport equation. This was achieved by solving the simplified Navier-Stokes equation (Equation (11) and (12)):

$$\nabla p = \nabla^2 v \quad (11)$$

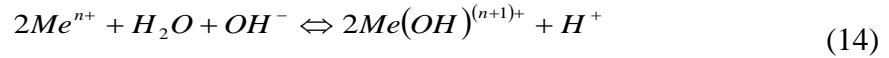
$$\nabla \cdot v = 0 \quad (12)$$

Where v : in-situ velocity; p : pressure.

Galvele⁷² developed a 1D mechanistic model for pitting corrosion. Two reactions, metal oxidation and first level metal ion hydrolysis, are considered as the main mechanism of pitting corrosion, as shown in Equation (13) and (14). In this model, diffusion is considered to be the only mechanism for species transport, while electro-

migration and convection are neglected inside the pit. This is due to the assumption of sufficient supporting electrolytes in the bulk and lack of convective flow inside the pit due to geometric restrictions. By solving the mass transport equation (in a similar form like equation (8)) in conjunction with chemical equilibrium for involved atoms (Me, O and H), the concentrations of species can be obtained and the fluxes can then be calculated. An arbitrarily determined constant current is used in the model to give the flux of metal species. The analytic solution of the equation system leads to the identification of a key parameter, $x.i$ (product of pit depth and current density), that is considered to control the occurrence of pitting corrosion. In a later paper, Galvele published an improved model in which full hydrolysis of cation is taken into account.⁷³ The model generates a relationship between pitting potential and pH. The model suggests that for a bivalent metal, pitting potential is independent of bulk pH up to the value of 8-9 and becomes pH-dependent at a higher pH; for a trivalent metal, pitting potential is unaffected by bulk pH due to multiple steps of hydrolysis. Gravano and Gavele⁷⁴ further improved the model by taking into account the electro-migration effect. The model was applied to zinc in a diluted NaCl solution with a borate buffer. The model suggests that effect of aggressive species (Cl⁻) on pitting is inhibited by the buffer solution due to increasing critical $x.i$ value to a level where electro-migration becomes important. In this case, solution resistance inside the pit plays an important role in determining pitting potential.





Bardal *et al.*⁷⁵ developed a mechanistic model to predict the galvanic corrosion induced by contact of dissimilar metals. The model is based on the Laplace equation for potential ($\nabla^2\phi = 0$), solved using the boundary element method, which transforms the governing equation into the form of:

$$\int_{\Gamma} \frac{\partial\phi}{\partial\Gamma} d\Gamma = 0 \quad (15)$$

Where Γ is the boundary surface of the computational domain. Polarization curves obtained experimentally for electrochemical reactions are used to describe the boundary conditions. The variation of cathodic reaction rate at different locations along the metal surface is estimated by incorporating the concept of diffusion boundary layer development.

Fu *et al.*⁷⁶ proposed a transient mechanistic model to simulate pit propagation rate. The model considers the current and potential distribution, mass transport and hydrolysis of metal ions. The model is initiated by solving for electro-migration potential and diffusion potential distribution separately, based on initial concentrations and solution conductivity, as shown in equations (16) and (17), respectively. With the knowledge of potential distribution, fluxes of species can be calculated using equation (18). A mass transport equation is then solved to give the concentration distribution in a new time step (equation (19)). This is followed by an update of solution conductivity and water chemistry. The process is then repeated for as many time steps as necessary.

$$i = \kappa \nabla \phi \quad (16)$$

$$\nabla \phi' = \frac{\sum z_j F u_j c_j \nabla \mu_j}{\sum z_j^2 F^2 u_j c_j} \quad (17)$$

$$N_j = u_j c_j \nabla (z_j F \phi) + u_j c_j \nabla \left((z_j F \phi' - \mu_j) \right) \quad (18)$$

$$\frac{\partial c_j}{\partial t} = -\nabla \cdot N_j \quad (19)$$

Where i : current; κ : solution conductivity; ϕ : electromigration potential; ϕ' : diffusion potential; z_j : charges of ionic species; u_j : mobility; c_j : concentration; μ_j : chemical potential; N_j : fluxes; F : Faraday's constant and t : time.

Benrais and Sohm⁷⁷ proposed a pit propagation model to simulate pitting corrosion of aluminum in acidic media. The model is an improved version of the Pickering⁶⁷ model. The distribution of concentrations and potentials along the pit depth is obtained analytically by transforming governing mass transport equations into non-dimensional form. To derive the analytic expressions for concentration and potential as a function of pit depth, a number of assumptions are made in the model: the solution inside the pit is assumed to be dilute; species are assumed to travel through the solution only by molecular diffusion and electro-migration; aluminum ion is assumed to be saturated on the bottom of the pit, and no supersaturation is considered. Aluminum ion hydrolysis is neglected in the model, as is any change of corroding area as a result of corrosion.

Sharland^{78,79} presented a 2D mechanistic model to simulate the propagation stage of iron corrosion in crevices and pits with prescribed dimensions. A mass transport

equation (equation (20)) is solved for all involved species in conjunction with a charge balance equation (equation (21)):

$$\frac{\partial c_i}{\partial t} = D_i \nabla^2 c_i + z_i F u_i \nabla (c_i \nabla \phi) + R_i \quad (20)$$

$$\sum z_i c_i = 0 \quad (21)$$

Where D_i : diffusion coefficient of species; c_i : concentration of species; z_i : electrical charge number; F : Faraday constant; u_i : mobility of species; ϕ : solution potential; i : current density; R_i : chemical reaction rate; t : time. A few assumptions are made in the model: passivity is maintained outside the pit/crevice; chemical equilibrium is maintained for all involved chemical reactions; convective flow is neglected inside the pit/crevice; dilute solution is assumed; and moving-boundary of pit bottom is slow compared to migration rate of ions and is therefore neglected. Only one electrochemical reaction, iron oxidation, is considered in this model. The kinetics of iron oxidation rate are described by a Tafel expression as a function of potential.

Heppner⁸⁰ developed a 2D mechanistic model for crevice corrosion. Mass transport, electrode kinetic, chemical equilibrium and fluid mechanics are taken into account in his model. The governing equation is:

$$\frac{\partial c_i}{\partial t} = D_i \nabla^2 c_i - \left(z_i u_i F \frac{i + i_{cdp}}{\kappa} + v \right) \cdot \nabla c_i - z_i u_i F \frac{\delta}{\epsilon} c_i + R_i \quad (22)$$

Where c_i : concentration of species; t : time coordinate; D_i : diffusion coefficient; z_i : electrical charge number; u_i : mobility of species; F : Faraday's constant; i : current density due to regular potential; i_{cdp} : current density due to convection diffusion

potential; \mathbf{v} : in-situ velocity; κ : solution conductivity; δ : charge density; ϵ : dielectric constant of water.

Walton *et al.*⁸¹ presented a mechanistic model to simulate crevice corrosion of passive and active metals. This model is made in a generic way in order to accommodate different corrosion systems. The inputs of the model include: specification of species involved, chemical reactions in the solution, chemical potential of species, electrochemical reaction kinetics on metal/solution interface and mesh sizes. The model starts with a calculation of current flowing through the solution based on the current generated at the metal/solution interface (equation (23)). This is followed by a calculation of potential distribution using equation (24). Equation (24) suggests that current flow in the solution is ascribed to electro-migration and diffusion. With the knowledge of potential and current distribution, mass transport of involved species can then be solved for using equation (25). It should be noted that the fluxes of electroactive species (\bar{N}_n) induced by electrochemical reactions on the metal surface, are directly incorporated into the governing equation and therefore not used as boundary conditions.

$$i_s = \frac{1}{A_c} \int_L^x i_e P dx \quad (23)$$

$$\nabla \phi_s = \frac{-\left(i_s + \sum_n (z_n F D_n / \gamma_n) (\gamma_n \nabla c_n + c_n \nabla \gamma_n) \right)}{\kappa} \quad (24)$$

$$\frac{\partial c_n}{\partial t} = -\nabla \cdot N_n + \frac{P}{A_c} \bar{N}_n + R_n \quad (25)$$

Where i_s : current density at any point in the crevice corrosion; i_e : current density at the metal/solution interface; L : the depth of the crevice/pit; P : the corroded perimeter ($2\pi r$ for a pit, $2w$ for a crevice); x : the position in the crevice measured from the mouth; A_c : cross-sectional area of the crevice/pit (πr^2 for a pit, wg for a crevice); ϕ_s : solution potential; z_n : charges of ionic species; D_n : diffusion coefficient; F : Faraday's constant; c_n : concentration; γ_n : activity coefficient; κ : solution conductivity; N_n : flux of species in solution; \bar{N}_n : flux of species on the metal/solution interface; R_n : chemical reaction rate.

Xu *et al.*^{82,83} simulated crevice corrosion based on an IR-driven mechanism. In their models, potential and current distributions in a crevice are obtained by solving the Laplace equation for potential. The electrochemical reaction kinetics at the crevice surface are described by the polarization curve obtained in bulk solution. An iterative algorithm is used to establish the transition from passive to active surfaces along the crevice wall. The critical point where transition occurs is shown to be influenced by polarization behavior of the metal-solution system, solution conductivity, potential at outside surface of the crevice, dimensions of crevice gap and depth and passive current density.

Achour *et al.* developed a mechanistic model for pit propagation of carbon steel in CO₂ environments under turbulent conditions.⁸⁴ The model takes into account chemical equilibrium, electrochemical reaction kinetics of iron oxidation, FeCO₃ layer formation kinetics and hydrodynamic conditions inside the pit. In this model, pit propagation/repassivation is determined based FeCO₃ precipitation. Surface Fe²⁺ concentration is determined by mass balance accounting for chemical reactions, surface

electrochemical reactions and mass transfer. The surface Fe^{2+} concentration is then compared with the Fe^{2+} concentration associated with $FeCO_3$ saturation. If the former is higher than the latter, the pit is considered to be protected; otherwise the propagation rate is calculated according to Equation (26):

$$J_{cor} = k([Fe^{2+}]_{ss} - [Fe^{2+}]_s) \quad (26)$$

Where J_{cor} : flux of iron dissolution; k : mass transfer coefficient of Fe^{2+} ; $[Fe^{2+}]_{ss}$: saturation concentration of Fe^{2+} with respect to $FeCO_3$; $[Fe^{2+}]_s$: surface Fe^{2+} concentration.

Engelhardt and Macdonald⁸⁵ analyzed the relationship between critical pit depth and critical service life. A quasipotential is proposed in the model as a function of metal potential. Based on the quasipotential, they were able to develop the analytical solutions for potential and concentration distribution inside the pit and the pit propagation rate. The model shows that the initial anodic current density will not exceed the 10^{-4} - 10^{-3} A/cm² given that the critical pit depth is less than 10mm and that service life is more than 1 year. This conclusion is limited by the assumption that polarization behavior of anodic dissolution does not change as a pit propagates. The model also suggests that potential drop inside the pit can be neglected if the conductivity of the bulk solution is sufficiently high, roughly in the order of magnitude for seawater. It is claimed that this model can be used to extrapolate short term experimental results to long term operations.

Laycock *et al.*⁸⁶ proposed a mechanistic model to simulate a pit propagation process of stainless steel under potentiostatic control. A truncated spherical-shaped pit and the solution beyond the pit are taken as the computational domain. The pit is assumed

to retain the original shape during pit evolution. In this transient model, initial conditions are set at the point where a pit has just been initiated. At pit initiation, it is assumed that metallic ions are saturated in the pit, but absent from the outside solution of the pit. A reference potential of 0V is given everywhere in the domain. Chemical equilibrium is assumed for reactions inside the pit with the exception of salt precipitation, the rate of which is proposed to be a linear function of supersaturation. Two electrochemical reactions, metal oxidation and H^+ reduction, are considered in the model. The kinetics of both reactions are assumed to follow Tafel's law. The mass transport equation and the Laplace equation for potential are solved for concentration and potential distribution under applied potential. The moving boundary due to receding of the pit bottom is accounted for in the model. Repassivation is considered to occur when anodic current density exceeds a critical current density defined as a function of dissolved metallic ion concentration. In a later model, Laycock *et al.*⁸⁷ incorporated a stochastic approach into the earlier model in order to simulate pit initiation. In this model, 3 geometric parameters for the pit: radius, degree of opening and depth from the free surface, are specified by a random function following log-normal distribution. The maximum potential above which a stable pit is formed and the minimum potential, below which pit dies are empirically related to three geometric parameters, giving the corresponding fluctuation of potentials. The number of pit nucleation sites is determined by a binomial function. The Monte-Carlo simulation is then performed to determine the probability of pit initiation.

Malki and Baroux⁸⁸ proposed two stochastic approaches to simulate pit growth kinetics. In the first approach, a fresh metal surface is discretized into multiple sites

subject to pitting corrosion. The Monte-Carlo tests are performed with respect to a dissolution probability, which changes with time. If the test is positive, a pit is developed with a randomly determined pit radius ranging from 0 to the maximum values determined by the applied potential and solution corrosivity; the process is then taken to the next time step. A repassivation probability is also incorporated in the model. At each time step, iterations are performed as many times as needed to generate a pit. The pit growth rate is given by the pit depth and the time. In the second approach, the metal/passive film/electrolyte system is discretized into multiple cells using a technique known as Cellular Automation. Each site is assigned one of four possible states: corrosion cell, non-corrosion cell, passive film cell or metallic substrate cell. At each time step, cells can transform into different states following certain transition rules; the number of corrosion cells is related to corrosion current. The rules are defined based on the following assumptions: that a pit is already initiated; that passive film acts as a perfect barrier for dissolution; and that the corrosion process is under diffusion control.

Scheiner *et al.*⁸⁹ presented a mechanistic model to simulate the stable pitting growth of stainless steel by assuming a diffusion-controlled corrosion process. Moving boundaries are taken into consideration in the model. Four computational domains, namely: solid metal, salt film at pit surface, solution inside and outside the pit, are identified in the model, where concentrations of metal/metallic ions are calculated in different ways. The authors accentuated the concentration discontinuity from the salt film to the pit solution, which incapacitates Fick's law in calculating concentration gradient within the salt film. In this model, the evolution of pit shape as a function of time can be

mechanistically determined as a result of the corrosion process, which is particularly related to solid metal concentration, saturation concentration of dissolved metallic ions, diffusion coefficient of the ions and the boundary ionic flux.

Agarwal *et al.*⁹⁰ developed a model to simulate the current distribution in crevice corrosion. Potential and current distribution are obtained by solving the Laplace equation for potential. The effect of non-conductive particulates on the cathode surface is accounted for by idealizing the particulates into uniform distribution with fixed porosity and tortuosity. It was argued that the particulates influence current distribution in two ways: they reduce the electrolyte conductivity due to the effect of volume blockage and they reduce the electrochemical reaction kinetics by blocking parts of the active surface. The former is calculated using Bruggeman's equation⁹¹, while the latter is taken into consideration by involving particulate surface coverage in the surface reaction kinetics.

Han *et al.* proposed an electrochemical model to calculate the steady-state localized corrosion rate of carbon steel in CO₂ environments.⁹² The model is based on their experimental observations which suggest passivation of carbon steel in the presence of FeCO₃. The substance responsible for passivation is proposed to be magnetite (Fe₃O₄). Chemical equilibrium is assumed in the model. An experimentally determined passive current density is used in the model. The cathodic reaction kinetics on the passive surface are assumed to follow Tafel behavior, and a correction factor is introduced into the cathodic reaction rate calculation due to the lack of consideration for solution resistance effect.

Amri *et al.*⁹³ developed a steady-state model to simulate the pit propagation of carbon steel in CO₂ environments with the presence of acetic acids. A 2D simulation is performed in a domain containing a pit with prescribed sizes and a diffusion boundary layer above it. Mass transport equations with consideration of diffusion and electro-migration are solved for concentration gradient, and the Laplace equation is solved for potential distribution. The electrochemical reaction kinetics are described by Tafel's law. The model shows the depletion of acetic acid and progressive reduction of CO₂ concentration towards the pit bottom. This is attributed to the reduction of H⁺ and diffusion limitation.

This part of literature review points out two main modeling strategies for simulating pit propagation in the context of galvanic cell. The first one is solving the mass transport equation with the electro-migration effect involved, the second one is by solving the Laplace equation for potential distribution. Essentially, the concept of electroneutrality is embedded in both approaches. Both methods lead to the potential distribution along metal surface, which highlights the importance of solution resistance between electrodes. The consideration of some complicating factors, such as non-conductive precipitates, changing pit shape, transition of passive-active region along the pit wall and chemical reactions (such as metal ion hydrolysis), plays a significant role in determining model complexity and model limitations.

CHAPTER 3: RESEARCH OBJECTIVES

The above literature review indicates that most localized corrosion models either aim at simulating a specific stage of the localized corrosion process or are exclusively applicable to specific environments, making them less valuable for a carbon steel exposed to CO₂ aqueous system.

The overall goal of this study is to develop a mechanistic model that can be used to predict the localized CO₂ corrosion process of carbon steels. The effect of H₂S on localized corrosion is not known at present and will not be taken into account in this model. The model is expected to cover the following aspects of the corrosion process:

- Uniform or localized CO₂ corrosion rate of carbon steel as a function of time;
- Concentration profiles of species involved in the corrosion process as functions of locations and time;
- Characteristics of FeCO₃ layer formation in terms of porosity and tortuosity as a function of time;
- FeCO₃ layer removal on metal surface leading to pit initiation;
- Passivation/repassivation effect;
- Galvanic effect between anode and cathode.

Potentiodynamic and potentiostatic tests have revealed that the passive film formed on a carbon steel surface in the system of interest is not as protective as those present on stainless steel or other alloy surfaces. To make a distinction from commonly-known passivation as exhibited by alloys, the term “pseudo-passivation” will be used

throughout the document to refer to the passive-like behaviour of carbon steel in an $\text{H}_2\text{O}/\text{CO}_2/\text{Fe}^{2+}$ environment.

The overall goal of this project was achieved by fulfilling the individual objectives listed below:

- Expand the original CO_2 corrosion model of Nešić *et al.*^{13,14} (a “single-point” model) into a “two-point” model to simulate an anode and cathode of a galvanic cell and establish the link between the anode and cathode through potential distribution along the metal surface. This step forms the basis for all future developments.
- Improve the previous FeCO_3 layer growth model numerically by solving the governing equation with a proper higher-order upwind scheme for convection-like term and the implicit time marching scheme for better stability and faster calculation;
- Investigate the effect of Fe^{2+} hydrolysis on localized CO_2 corrosion of carbon steel;
- Derive the Butler-Volmer expressions for electrochemical reaction kinetics and implement them into the mass transport equations as implicit boundary conditions to achieve a realistic potential distribution in a galvanic cell;
- Add hydrogen gas as an additional species into the system in order to obtain the realistic reversible potential of cathodic reactions;
- Incorporate thermodynamic calculation for the generation of magnetite to enable the determination of pseudo-passivation/repassivation;

- Experimentally determine the major factors affecting pseudo-passive current density;
- Based on the experiments, develop/implement a mechanistic model to calculate the pseudo-passive current density of carbon steel in CO₂ environments;
- Investigate the cathodic reaction kinetics on pseudo-passive carbon steel surfaces;
- Develop a mechanistic model to obtain the potential and current distribution in a galvanic cell with the effect of non-conductive FeCO₃ layer;
- Implement a random function to simulate the stochastic behaviour of pit initiation in terms of time.

All of the above tasks have been accomplished and are presented in the corresponding subsections of Chapter 4.

CHAPTER 4: MECHANISTIC MODEL OF LOCALIZED CO₂ CORROSION

4.1 Introduction

As noted above, localized corrosion presents one of the greatest threats to integrity of pipelines in oil and gas industry. Extensive research efforts have been made towards understanding the mechanisms of localized corrosion in the past few decades, yet the mechanistic understanding of localized corrosion is still limited. This is partly due to the fact that water chemistry, particularly surface water chemistry, in the restricted area of a pit is not easily reached by conventional equipment, yet it often differs substantially from the bulk solution. The picture is further complicated by the fact that initiation of pitting corrosion is difficult to manage and detect, even in highly controllable laboratory experiments. Pit initiation often manifests itself as a seemingly random process as to when and where it occurs. This has led to a number of stochastic models for pit initiation, as discussed in Chapter 2. One can intuitively imagine that localized corrosion has to do with water chemistry in close proximity to the metal surface, but this is not yet fully understood by the corrosion community. Therefore, it would be beneficial to determine the physic-chemical parameters near the steel surface, such as water chemistry and electrochemical properties, in order to understand the process of localized corrosion. Unfortunately, up to now, no experimental methods are reliable for detecting localized corrosion or local water chemistry, making it one of the biggest challenges for corrosion research. Due to the difficulties associated with experimental means, a mechanistic model can be helpful towards the understanding of localized corrosion of carbon steel.

The goal of this chapter is to present a transient mechanistic model that can be used to predict the details of the corrosion process of mild steel exposed to an aqueous environment containing CO₂. It should be mentioned that localized corrosion can be governed by multiple mechanisms, as can be seen from the review of the various localized corrosion models presented in Chapter 2, such as pit acidification, concentration differentiation cells and flow induced corrosion, to name a few. This model is designed to cover one of the major mechanisms for localized corrosion of mild steel in CO₂ environments: galvanic coupling between the bare pit (anode) and the pseudo-passive surface (cathode), and is primarily based on the recent studies at the ICMT.¹¹ The model is built based upon fundamental theories governing chemistry, electrochemistry and transport phenomena. Evolution of the corrosion process is simulated as a function of time. Depending on specific physical and chemical conditions, uniform or localized corrosion might be predicted. After a randomized event is triggered for the initiation step of localized corrosion, the model can predict and simulate the transition from uniform to localized corrosion according to appropriate theories. Various factors involved in the corrosion processes, such as FeCO₃ layer precipitation and dissolution, solution resistance, pseudo-passivation, depassivation and repassivation are built into the model to give a comprehensive and physically realistic description of the actual process. In addition to the corrosion rate, the model also provides other valuable information to help evaluate environment corrosivity and explain corrosion behavior. This information includes: electrochemical potential distribution, current distribution, concentrations of species, fluxes of species, and FeCO₃ layer properties at any given location and time.

In the following subsections, the processes simulated in the model are qualitatively described, followed by theories governing various phenomena and mathematical descriptions of the theories. Model verification and parametric study are then presented to discuss how key parameters affect the localized corrosion process. The assumptions and limitations of the model are then presented in final portion of the chapter.

4.2 Physico-chemical Processes Described by the Model

The model describes CO₂ localized corrosion process in terms of three stages: pseudo-passivation/ repassivation, pit initiation and pit propagation. Each of these stages has its unique mechanisms and characteristics, and therefore each has to be considered separately. The processes simulated in this model are described below.

When carbon steel is in contact with an aqueous CO₂ solution, electrochemical reactions occur on the steel surface. Some species are consumed and others are generated, which establishes the concentration gradients of the species. As the corrosion process proceeds, ferrous ion (Fe²⁺) is continuously released into the solution and varies the water chemistry. When the product of the concentrations for Fe²⁺ and CO₃²⁻ in the solution exceeds the solubility limit of FeCO₃, it will precipitate out of the solution and build a layer on the metal surface. This deposited corrosion product poses significant mass transfer resistance to species (including H⁺) moving to/ from the bulk solution which leads to an increased pH at the metal surface. The pH increase enables the formation of a pseudo-passive phase beneath the corrosion product layer, which is thought to be a mixture of FeCO₃, Fe(OH)₂ and/or Fe₃O₄. As a result of pseudo-passivation, the metal

potential increases. Evidently, up to this point in the scenario, the metal experiences uniform corrosion. It can be assumed that at some point in time, a small area of the metal loses its protective film, leading to depassivation and resulting in potential drop within this area. Therefore, a potential difference is established between this small film-free active surface (which has now become an anode) and the large film-covered pseudo-passive surface around the anode (which has now become a cathode). Based on the galvanic coupling mechanism, this potential difference can drive the anode to corrode at a much higher rate than which would be experienced with uniform corrosion. In cases where supersaturation of FeCO_3 in the solution is sufficiently high, substantial amounts of Fe^{2+} resulting from pit propagation promote further precipitation of FeCO_3 on the anode. This may again increase the surface pH of the anode and facilitate repassivation, which would lead to pit death. The processes described above are schematically illustrated in Figure 4 through Figure 9 .

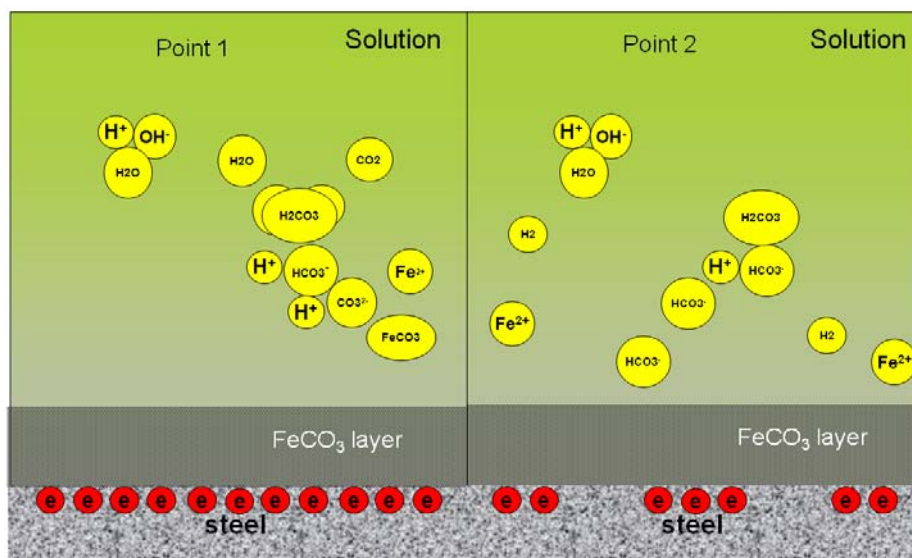


Figure 4. Illustration of corrosion process: FeCO_3 layer formation leading to surface pH increases.

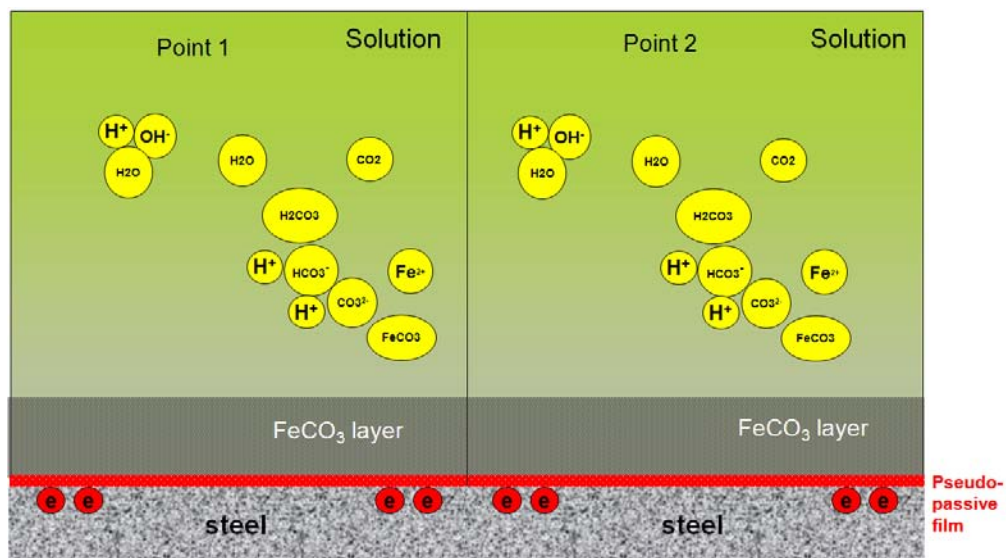


Figure 5. Illustration of corrosion process: pseudo-passivation leading to potential increases.

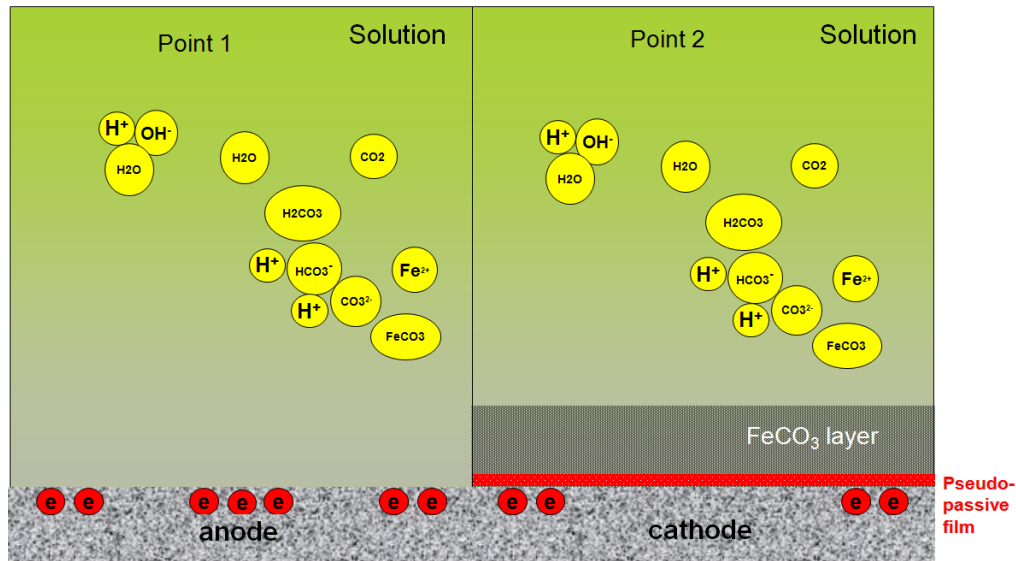


Figure 6. Illustration of corrosion process: depassivation leading to separation of anode and cathode and establishment of potential difference.

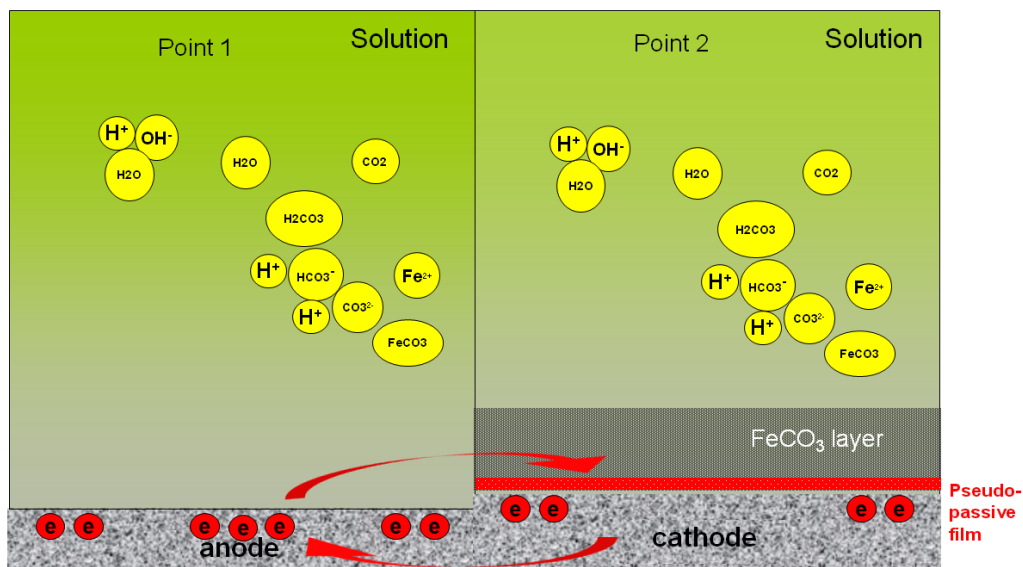


Figure 7. Illustration of corrosion process: Pit propagation.

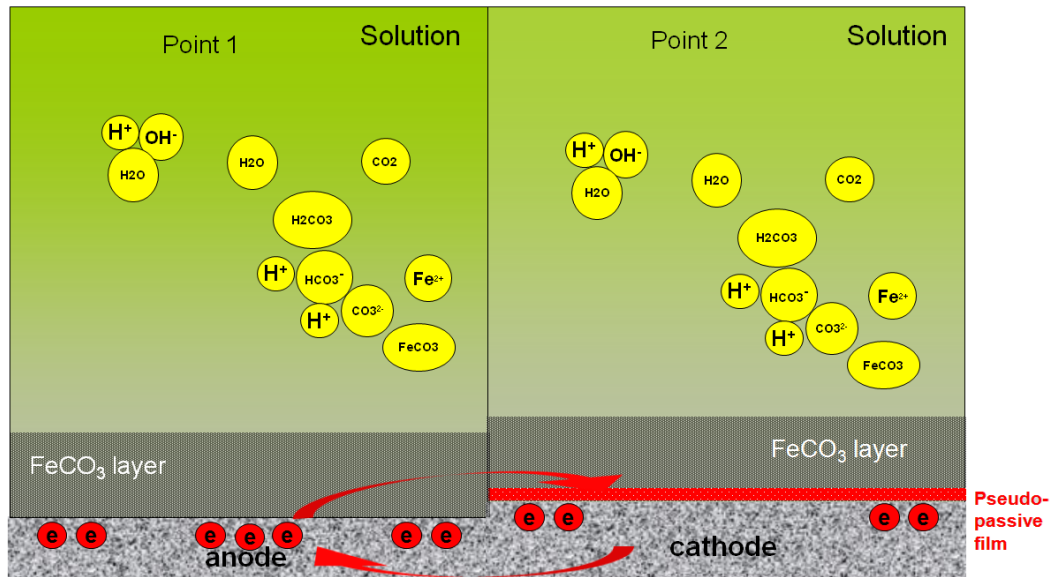


Figure 8. Illustration of corrosion process: FeCO₃ re-precipitation if supersaturation of FeCO₃ is sufficiently high.

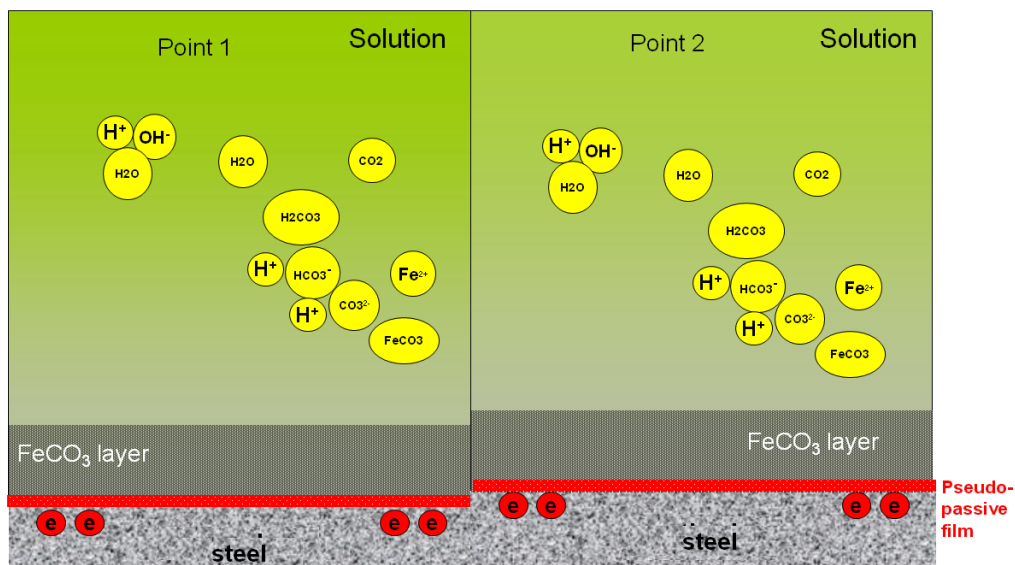


Figure 9. Illustration of corrosion process: Repassivation leading to pit death.

4.3 Physico-chemical Model

Localized CO₂ corrosion is a complex process that involves multiple physico-chemical processes, dependent on each other. These include: chemical reactions, electrochemical reactions, mass transport, FeCO₃ layer formation, pseudo-passivation/repassivation, pit initiation and pit propagation. These factors must be taken into account in the model in order to provide a realistic description of the corrosion process.

4.3.1 Chemical Reactions

Gaseous CO₂ and water are almost always present in various quantities along with oil and gas in pipelines. Various chemical reactions take place in the water phase due to the presence of CO₂. These reactions have to be taken into consideration in order to obtain accurate concentration profiles of corrosive species for further calculation.

It is generally agreed that most chemical reactions proceed much faster than other processes involved in corrosion, such as mass transport and electrochemical reactions. Therefore, many corrosion models neglect the chemical reaction effect by assuming the preservation of chemical equilibrium in the solution. This assumption does not apply in a CO₂ corrosion environment, since CO₂ hydration, (Reaction (28)), has been reported to be a slow step⁹⁴ and in some cases becomes a rate-limiting step in the CO₂ corrosion process. Hence, a local non-equilibrium condition is likely to exist, which alters the corrosion process.

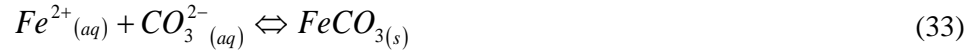
For a CO₂ aqueous system, the following reactions are considered to be present at all times:



In some environments, organic acids, particularly low-molecular-weight organic acids, are found primarily in the water phase and can lead to corrosion of mild steel as well. Acetic acid (CH_3COOH or in shorthand: HAc), the most prevalent type of organic acid found in brines, can be treated as the representative of all other types of organic acids, as similar corrosiveness has been established for all types of low-molecular-weight organic acids.⁹⁵ The HAc partially dissociates in the water phase to release H^+ and Ac^- , as indicated by Reaction (32). It is stronger than H_2CO_3 , and therefore serves as the main source of H^+ when similar concentration of the two acids are encountered.



Another chemical reaction that plays a vital role in CO_2 corrosion is $FeCO_3$ precipitation (Reaction (33)). Precipitation proceeds when the product of concentrations of Fe^{2+} and CO_3^{2-} in aqueous phase exceeds the solubility limit of $FeCO_3$. Unlike other chemical reactions occurring homogeneously in the solution, $FeCO_3$ precipitation is a heterogeneous process. Nucleation of solid iron carbonate occurs preferentially on the steel surface or inside the void space within the present solid layer.¹³ This reaction will be discussed further in section 4.3.4.



For a localized corrosion process, another reaction that merits discussion is Fe^{2+} hydrolysis, shown in Reaction (34). As noted in the literature review, some localized corrosion models are built based on a pit acidification mechanism resulting from metallic ion hydrolysis, particularly in oxygen-containing environments. One aim of this study is to clarify the role of Fe^{2+} hydrolysis in the localized CO_2 corrosion process in terms of pit acidification. If significant H^+ enrichment is caused by this reaction, it must be taken into consideration in the model.



In this work, theoretical calculations are performed based on thermodynamic theory in order to evaluate the significance of Fe^{2+} hydrolysis reaction in oxygen-free CO_2 environments.

At equilibrium, the equilibrium constant of a reaction can be related to Gibbs free energy in the following fashion:

$$RT \ln K^o = -\Delta_r G_m^o \quad (35)$$

where R is universal gas constant; T is absolute temperature; K^o is equilibrium constant for the standard condition and G_m^o is standard Gibbs free energy of a reaction.

Gibbs free energy of a reaction is given by the chemical potentials of species involved in the reaction as:

$$\Delta_r G_m^o = \sum v_i \mu_i^o \quad (36)$$

where ν_i is the stoichiometric coefficient of species in the reaction and μ_i^o is the standard chemical potential of species.

The combination of Equations (35) and (36) yields:

$$\ln K^o = -\frac{\sum \nu_B \mu_B^o}{RT} \quad (37)$$

For Fe^{2+} hydrolysis at 25°C, the equilibrium constant can be obtained by substituting corresponding standard chemical potentials into Equation (37), which yields:

$$\log K^o = -13.29 \quad (38)$$

The equilibrium constant of Reaction (34) can be given as:

$$K^o = \frac{c_{\text{H}^+}^2}{c_{\text{Fe}^{2+}}} \quad (39)$$

Where c_{H^+} and $c_{\text{Fe}^{2+}}$ are concentrations of H^+ and Fe^{2+} respectively.

Combination of Equations (38) and (39) yields:

$$\text{pH} = 0.5 \times (13.29 - \log_{10} c_{\text{Fe}^{2+}}) \quad (40)$$

Equation (40) allows the calculation of equilibrium pH produced by hydrolysis reaction of Fe^{2+} at 25°C. For a saturated solution of FeCl_2 in which Fe^{2+} concentration is around $4.44 \times 10^5 \text{ ppm}$ (8 mol/L), Equation (40) yields a pH of 6.2; for concentration of Fe^{2+} at 50 ppm, which is commonly considered to be a high concentration in oil fields, the equilibrium pH is around 8.2. Clearly, hydrolysis of Fe^{2+} would not lead to substantial solution acidification in a typical CO_2 aqueous environment. Therefore, this reaction can be neglected in the bulk solution as the additional source of H^+ . However, it should be noted that on the corroding metal surface particularly underneath the FeCO_3 layer where

pH increase and Fe^{2+} enrichment are expected, the equilibrium pH of Reaction (34) could be achieved to trigger Fe^{2+} hydrolysis. In fact, Fe^{2+} hydrolysis is proposed in this model to be an essential step to promote pseudo-passivation of carbon steel in CO_2 environments.

4.3.2 Electrochemical reactions

For CO_2 corrosion, several electrochemical reactions are considered to contribute to the overall corrosion rate of mild steel.

4.3.2.1 Anodic reactions

Dissolution of iron is the dominant anodic reaction. This reaction proceeds via a multi-step mechanism that is mildly affected by pH and CO_2 concentration.¹³ Within the range of typical CO_2 corrosion, e.g. $4 < \text{pH} < 6$, the dependency on pH tends to diminish.¹³ Therefore, the dependence of the anodic dissolution rate on pH and CO_2 is neglected in the model. At the corrosion potential (and up to 200 mV above), this reaction is under charge transfer control and the electrochemical behavior can be described using the Butler-Volmer equation as presented in Table 2.



4.3.2.2 Cathodic reactions

H^+ reduction is one of the main cathodic reactions:



This reaction is limited by how fast H^+ can be transported from the bulk solution to the steel surface through the mass transfer layer (including the liquid boundary layer

and the $\text{FeCO}_3(\text{s})$ layer if it exists). Higher corrosion rates are observed for a CO_2 aqueous solution compared to strong acid solutions (such as HCl) at the same pH. However, for a practical CO_2 system where $4 < \text{pH} < 6$, the limiting current of this reaction would be small due to the relatively low concentration of H^+ . This suggests that CO_2 also plays a certain role in H^+ reduction. This can be explained by the fact that the homogeneous dissociation of H_2CO_3 provides an additional reservoir for H^+ ions, which then adsorbs on the steel surface and gets reduced according to Reaction (42). Apparently, any rapid consumption of H^+ can readily be replenished by Reactions (29) and (30). Thus for typical CO_2 corrosion, the presence of CO_2 leads to a much higher corrosion rate than would be found in a strong acid solution with the same pH.

In the vicinity of the steel surface, another electrochemical reaction can take place as well: H_2CO_3 adsorbs at the steel surface and is directly reduced according to Reaction (43). This is referred to as “direct reduction of carbonic acid”.⁹⁴ As argued by Nešić *et al.*¹³, this reaction is just an alternative pathway for the same cathodic reaction - hydrogen evolution because addition of Reactions (29) and (42) leads to Reaction (43). The distinction is only in the pathway, i.e in the sequence of reactions.



The rate of this additional hydrogen evolution reaction due to the presence of CO_2 is mainly controlled by the slow CO_2 hydration step (28) and is a strong function of H_2CO_3 concentration which directly depends on partial pressure of CO_2 .

Acetic acid is known to be one of the species that attacks mild steel. Studies have shown that it is the undissociated (“free”) HAc and not the acetate ion Ac^- that is

responsible for corrosion.⁹⁶ The presence of organic acids is a major corrosion concern, particularly at lower pH and high temperature as more HAc would be generated under these conditions according to Reaction (32).

Like H_2CO_3 , HAc provides an additional source of H^+ , which then adsorbs at the steel surface and reduces according to the cathodic reaction (42).⁹⁶ Following the same reasoning as with H_2CO_3 , it is also possible that the HAc molecule itself is adsorbed at the steel surface and gets reduced,⁹⁷ which is often referred to as the “direct HAc reduction” pathway:



Another possible pathway for hydrogen evolution is the direct reduction of water:



Compared to the cathodic reactions described above, this pathway is very slow and can often be neglected in practical CO_2 corrosion environments. It has been argued that this reaction becomes significant only under very specific conditions, such as those encountered in very low partial pressure of CO_2 ($PCO_2 \ll 0.1$ bar) and high pH (pH >6),¹³ which is not common in oil and gas pipelines. Hence, this reaction is neglected in the model.

Bicarbonate reduction, as shown in Equation (46), has spurred extensive debate as to its significance to the overall corrosion process. Some people argue that this reaction, although much slower than the direct reduction of H_2CO_3 , could happen above a critical pH (around 8) at which H_2CO_3 would be depleted due to insufficient supply from the bulk. This would be due to the slow formation rate of H_2CO_3 , and HCO_3^- becoming the

dominating species underneath the film. Other people considered the kinetics of this reaction to be sufficiently low that, no matter how much HCO_3^- exists underneath the film, it would not be able to contribute to the overall corrosion rate significantly. However, it can be argued for a typical CO_2 environment where bulk pH ranges from 4 to 6 that this reaction is unlikely to change the corrosion rate in an appreciable fashion. For practical purposes (this reaction is difficult to distinguish experimentally and hence theoretically from direct carbonic acid reduction), it is neglected in the model.



4.3.3 Mass transport

Mass transport is an important part of the corrosion process since it strongly interacts with electrochemical reactions on the steel surface. Due to electrochemical reactions, certain species are produced or consumed on the steel surface. The mass transport process sweeps away or replenishes corresponding species changing their surface concentration what alters electrochemical reaction kinetics. Compared to some fast electrochemical reactions, such as H^+ reduction (42), mass transfer of H^+ proceeds much more slowly; therefore, the rate of the overall reaction is likely to be limited by the transport process, i.e. how fast this species can move through the mass transfer boundary layer and porous FeCO_3 layer. It is therefore essential to incorporate mass transport rates into the model in order to obtain an accurate depiction of the overall corrosion process.

Mass transport of species is mainly affected by three mechanisms: molecular diffusion, electro-migration and convection. Molecular diffusion is essentially a result of the Brownian motion of species, which manifests itself as an oriented movement along a

concentration gradient. For example when species are preferentially consumed on a steel surface, the amount of species moving towards the steel surface would be greater than those moving in the opposite direction. From the macroscopic perspective, it would appear that species move in a direction towards the steel surface. By the same token, for species generated on the steel surface, the net effect would be to drive species away from the steel surface.

Electro-migration is caused by the potential gradient established by species with different diffusion speeds. It acts only on charged species by electrostatic attraction force. In an aqueous solution, some species diffuse faster while others lag behind. For example, H^+ usually travels much faster than other species. Due to the positive charge of H^+ , a potential field is established between fast-moving H^+ and other species with negative charges, which tend to fall behind. This potential field accelerates the movement of negatively-charged species and slows down fast-moving species with positive charges, such as H^+ . It should be noted that, although electro-migration acts only on the charged species, it is able to exert a certain impact on non-charged species by changing the chemical reaction rate. For spontaneous uniform corrosion where no external potential field is applied in the solution, the electro-migration effect is usually negligible, since any potential difference established due to variation of diffusion can easily be annihilated by large amounts of supporting electrolytes, such as in a NaCl solution. The simulations using the previous version of the MULTICORP model,¹³ a mechanistic uniform corrosion model (on which the present model is based), have shown that the contribution of electro-migration to overall fluxes of species is small and can be neglected in spontaneous

uniform corrosion. However, when dealing with localized corrosion, a notable potential difference exists between anode and cathode, which affects the electro-migration; therefore, the effect of electro-migration must be accounted for in a localized corrosion scenario.

Convection is the movement of species carried by bulk flow. The convective flow in the direction parallel to the steel surface does not directly contribute to the corrosion process, while that in the direction perpendicular to steel surface contributes due to the mass transport of species. As turbulent eddies penetrate deep into the diffusion layer they shorten the distance over which diffusion and electro-migration take over. It should be stressed that no turbulence can exist in close proximity to the steel surface; species can travel through this region solely by molecular diffusion and electro-migration. In addition, the effect of convection becomes negligible when a porous FeCO_3 layer is present on the steel surface, forming a major diffusion barrier. This is discussed under the following heading.

4.3.4 FeCO_3 precipitation

The FeCO_3 layer, once formed, often controls the rate of corrosion due to substantial mass transfer resistance within the tortuous path of the film. It is well known that the protectiveness of the FeCO_3 layer is a function of corrosion rate and precipitation rate, which can be quantified by the so-called “scaling factor” as shown in (47):⁹⁸

$$ST = \frac{R_{prec}}{CR} \quad (47)$$

Where ST is the scaling factor, R_{prec} is the precipitation rate and CR is the corrosion rate, expressed in the same units. With a scaling factor greater than a critical value (which

means precipitation proceeds faster than corrosion), the FeCO_3 layer is dense and protective; for a scaling factor less than the critical value (which means precipitation is slower than corrosion), FeCO_3 becomes porous and non-protective. Apparently, the protectiveness of FeCO_3 is determined by the competing effects of corrosion and precipitation.

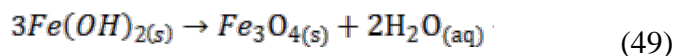
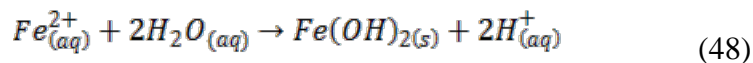
For localized CO_2 corrosion, FeCO_3 affects the corrosion process in four distinct ways. First, as FeCO_3 is formed by precipitation, it acts as the sink for Fe^{2+} and CO_3^{2-} ions by reducing their concentrations in the solution, which leads to local acidification of the solution according to Reaction (30). Second, the tortuous path within the discontinuous FeCO_3 layer poses a significant mass transfer resistance to species moving towards or away from the metal surface and slows down the electrochemical reactions. Third, the presence of non-conductive FeCO_3 layer on the metal surface effectively reduces the surface area exposed to the corrosive environment by covering up parts of the surface, which effectively slows down the electrochemical reactions. Lastly, the conductivity of the solution is reduced with the presence of the FeCO_3 layer by reducing cross-section areas through which conductive species can travel. It is worth mentioning that the effect of FeCO_3 on solution conductivity is negligible in a uniform corrosion process, as solution resistance does not play a significant role due to the close proximity of anode and cathode on the steel surface.

4.3.5 Pseudo-passivation

Research carried out in the past few years¹¹ has revealed that, when FeCO_3 layer forms, carbon steel exhibits a remarkable increase in potential, suggesting the occurrence

of pseudo-passivation on the steel surface. Steel surface analysis has confirmed the existence of magnetite (Fe_3O_4) and/or $\text{Fe}(\text{OH})_2$,¹² species commonly known to be related to passivity.

Pseudo-passivation of carbon steel in CO_2 environments allows for possible occurrence of localized corrosion as it can substantially raise the potential of the metal substrate and create a potential difference once depassivation occurs in localized areas. In the present model, the pseudo-passive film formation is related to formation of magnetite, which forms via a two-step process as shown by Reactions (48) and (49). In this process, $\text{Fe}(\text{OH})_2$ is first formed by Fe^{2+} hydrolysis, which is followed by oxidation of $\text{Fe}(\text{OH})_2$ to form magnetite.



The occurrence of pseudo-passivation can be illustrated in the context of the Pourbaix diagram. Figure 10 shows a Pourbaix diagram for a $\text{Fe}/\text{CO}_2/\text{H}_2\text{O}$ system for 80°C , 1ppm Fe^{2+} . Lines 1 and 2 correspond to Reactions (48) and (49), respectively. Under typical CO_2 environments, the operating point usually falls into the area of Fe^{2+} , indicating an active corrosion process (left of Line 1). At higher pH the solution is favoring FeCO_3 precipitation (right of Line 1), and in that case the surface pH will spontaneously increase beyond the bulk value as the FeCO_3 layer continues to form and present a mass transfer barrier. At some stage the operating point at the steel surface could reach Line 2 and magnetite would form, what is in the current model considered to be the required condition for occurrence of pseudo-passivation.

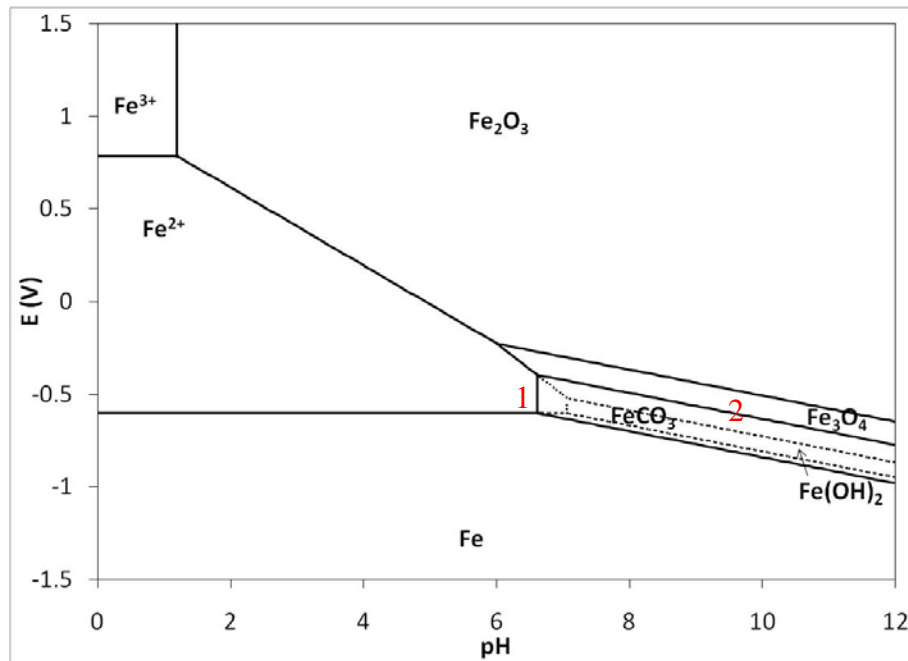


Figure 10. The Pourbaix diagram for Fe/CO₂/H₂O system with temperature 80°C, [Fe²⁺] 1ppm. Courtesy of T. Tanupabrungsun.

It should be noted that in this model, occurrence of pseudo-passivation is assumed to be very fast i.e. once the conditions for magnetite formation are reached it forms immediately, i.e. the kinetics associated with the formation of pseudo-passive film can be neglected.

4.3.6 Depassivation and pit initiation

Pit initiation is caused by depassivation i.e. a loss of protective layers (FeCO₃ layer and the pseudo-passive film) on certain parts of the steel surface leading to bare steel being exposed. This process often exhibits a large extent of scatter with regard to the time and the location. Without a clear understanding of the mechanism, this seemingly random phenomenon is often simulated using statistical approach.

The mechanism of pit initiation of carbon steel in CO₂ environment is an ongoing topic of research at ICMT. Initial inquiry seems to suggest that chemical dissolution of FeCO₃ is the most important factor leading to depassivation. At this stage, the mechanisms involved in film removal are not completely understood so in the current model, the worst case scenario is assumed and the FeCO₃ layer is “artificially” removed some time after pseudo-passivation is achieved. This provides an active anode area and a galvanic cell is established, which could be stable – leading to pit propagation or repassivation could occur leading to pit death.

4.3.7 Repassivation and pit death

Repassivation is a process in which an active steel surface may regain passivity under proper conditions, leading to an arrest in pit growth or so called pit “death”. In a CO₂ environment, repassivation of carbon steel occurs when solution supersaturation with respect to FeCO₃ becomes sufficiently high, which triggers fast precipitation of FeCO₃ on the anode. This would raise the surface pH to a level at which pseudo-passive film formation is favorable. In addition, increased Fe²⁺ concentration from the corrosion process also helps to drop the critical pH required for the formation of Fe(OH)₂. As can be seen in Reaction (48), increased Fe²⁺ favors the formation of Fe(OH)₂. In this model, onset of repassivation is determined by the same thermodynamic criterion as used for pseudo-passivation. This is to say that, once thermodynamic conditions are reached for the formation of magnetite through Reactions (48) and (49), repassivation is assumed to occur immediately.

4.3.8 Pit propagation

For carbon steel corroding in a CO₂ environment, the galvanic coupling mechanism was found to govern pit propagation.¹¹ This theory suggests that once local depassivation takes place on a small area of the steel surface, a potential difference is established between this active surface (anode) and the pseudo-passive surface around it (cathode). Such a potential difference serves as the driving force allowing the pit to propagate. In this process, the cathodic current occurring on the large area of the cathode is balanced by the anodic current on the small area of the anode, leading to a substantial anodic dissolution rate of the steel.

However, it has been found that the potential difference between anode and cathode alone would generate an unrealistically high pit propagation rate (100 mm/y or higher) which is not observed under realistic conditions. This can be explained by the IR potential drop mechanism proposed by Pickering *et al.* to account for the solution resistance between electrodes.^{82,83} In a uniform corrosion scenario, anode and cathode are so close to each other that solution resistance does not play a significant role as long as supporting electrolytes are present. However, in the case of localized corrosion, anode and cathode are separated leading to appreciable solution resistance between them. This solution resistance can sometimes limit the anodic dissolution rate to a large degree. Depending on how far the anode is from the cathode, the pit propagation rate would be different on different parts of anode surface, as solution resistance varies with the distance between electrodes. Figure 11 schematically shows the potential and current variation in a galvanic cell. It is important to note that electrochemical reactions are

driven by the electrode potential, which is defined as the potential difference across the double layer:

$$E = E_{metal} - \phi \quad (50)$$

where E is electrode potential driving electrochemical reactions; E_{metal} is the unique potential of the metal and ϕ is the potential drop across the double layer.

As shown in Figure 11, a potential distribution exists along the metal surface with higher potential on the cathode and lower potential on the anode. The potential difference becomes larger as anode and cathode are separated further away from each other due to higher solution resistance. This potential distribution results in non-uniformly distributed current along the metal surface. Clearly, neglecting the effect of solution resistance would lead to over-prediction of the pitting corrosion rate.

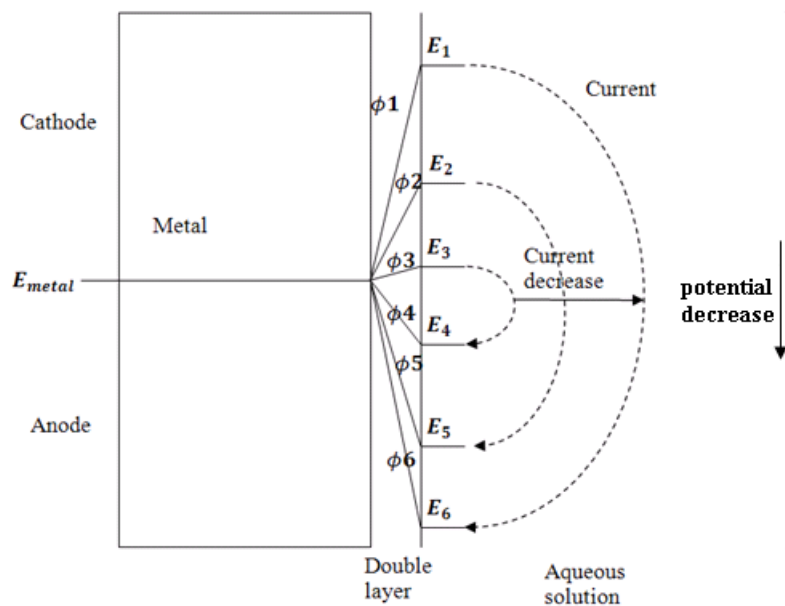


Figure 11. Illustration of potential distribution in a galvanic cell. ϕ_i represents the solution potential drop across the double layer, E_i represents the electrode potential at different locations, E_{metal} represents metal potential.

4.4 Mathematical Model

The theories described in section 4.3 can be mathematically described by corresponding physico-chemical laws. The mechanism involved in pit initiation is not presently available. In this model, the occurrence of pit initiation is triggered simply by removing protective layers on a small area of the steel surface (anode) at a randomly determined point in time.

4.4.1 Chemical reactions

Various chemical reactions occur simultaneously in a CO₂ /H₂O/carbon steel system. The major chemical reactions are shown in Reactions (27) through (31). As mentioned earlier, chemical equilibrium does not always exist in CO₂ corrosion systems as CO₂ hydration is a slow process, and the generation rate of H₂CO₃ by Reaction (28) might lag behind the consumption rate of H₂CO₃ on the steel surface, creating local non-equilibrium conditions, especially near the steel surface. To give a realistic description of the corrosion process, this model calculates the kinetics, i.e. the actual consumption or generation rate of a species through homogenous chemical reactions, without imposing chemical equilibrium. In cases where chemical reaction (both consumption and generation rates of species) are much higher than other processes (transport and electrochemical reactions), the species concentration is virtually unaffected by other

processes and therefore maintained at equilibrium; on the other hand, if the chemical reaction rates are slow (such as CO₂ hydration), the concentration of the involved species is influenced by other processes, which could then lead to non-equilibrium concentrations.

The complexity of mathematically modeling the CO₂ corrosion processes is largely due to the presence of chemical reactions by which various species concentrations are coupled, making the governing equations for mass transports strongly coupled and highly non-linear. The chemical reaction rate pertaining to any given species is calculated as the net consumption/generation rate. For a CO₂ aqueous system, it has been already shown that the following reactions are present:



Reaction (51) is always at equilibrium in CO₂-containing pipelines due to unlimited supply of CO₂ in the gas phase. The net reaction rates of Reactions (52) through (55) can be expressed as the difference between forward and backward reaction rates:

$$R_{hy} = k_{f,hy}c_{CO_2} - k_{b,hy}c_{H_2CO_3} \quad (56)$$

$$R_{ca} = k_{f,ca}c_{H_2CO_3} - k_{b,ca}c_{H^+}c_{HCO_3^-} \quad (57)$$

$$R_{bi} = k_{f,bi}c_{HCO_3^-} - k_{b,ca}c_{H^+}c_{CO_3^{2-}} \quad (58)$$

$$R_{wa} = k_{f,wa} - k_{b,wa}c_{H^+}c_{OH^-} \quad (59)$$

Based on the law of mass conservation, for a specific reaction, the mass consumed must be balanced by that generated. The consumption/generation rate of involved species due to Reactions (52) through (55) can be respectively expressed as:

$$R_{hy} = -R_{CO_2} = R_{H_2CO_3} \quad (60)$$

$$R_{ca} = -R_{H_2CO_3} = R_{H^+} = R_{HCO_3^-} \quad (61)$$

$$R_{bi} = -R_{HCO_3^-} = R_{H^+} = R_{CO_3^{2-}} \quad (62)$$

$$R_{wa} = R_{H^+} = R_{OH^-} \quad (63)$$

Combining the equations above, the net reaction rate of various species can be calculated as:

$$R_{CO_2} = -R_{hy} \quad (64)$$

$$R_{H_2CO_3} = R_{hy} - R_{ca} \quad (65)$$

$$R_{HCO_3^-} = R_{ca} - R_{bi} \quad (66)$$

$$R_{CO_3^{2-}} = R_{bi} \quad (67)$$

$$R_{OH^-} = R_{wa} \quad (68)$$

$$R_{H^+} = R_{ca} + R_{bi} + R_{wa} \quad (69)$$

Equations (64) through (69) present a lengthy and rigid method for calculating the net reaction rate. Nešić *et al.*¹³ proposed a convenient way to group reaction rates together in the form of:

$$R_j = a_{jk}r_k \quad (70)$$

Where R_j is the chemical reaction rate of the j th species; a_{jk} is the stoichiometric coefficient matrix with j being the number of rows in the matrix for the j^{th} specie and k being the number of columns in the matrix for the k^{th} reaction; r_k is the net reaction rate of the k^{th} reaction.

Using equation (70) on a CO₂ system, the chemical reaction rates of species can be expressed as:

$$\begin{bmatrix} R_{CO_2} \\ R_{H_2CO_3} \\ R_{HCO_3^-} \\ R_{CO_3^{2-}} \\ R_{OH^-} \\ R_{H^+} \end{bmatrix} = \begin{bmatrix} -1 & 0 & 0 & 0 \\ 1 & -1 & 0 & 0 \\ 0 & 1 & -1 & 0 \\ 0 & 0 & 1 & 0 \\ 0 & 0 & 0 & 1 \\ 0 & 1 & 1 & 1 \end{bmatrix} \begin{bmatrix} R_{hy} \\ R_{ca} \\ R_{bi} \\ R_{wa} \end{bmatrix} \quad (71)$$

Where the vector on the left side of the equation represents the net chemical reaction rates of various species, the first term on the right side of the equation is the tensor (representing the stoichiometric coefficient of each species in various chemical reactions, with negative values being reactants and positive values being products), and the second term on the right side of the equation is the vector for net reaction rate of the individual reaction (the value of which is related to concentrations of species, as shown in Equations (56) through (59)). The rate constants used in the model were compiled by Nešić *et al.* and can be found in the open literature.¹³

With this technique, additional chemical reactions (such as HAc dissociation, H₂S dissociation and HS⁻ dissociation) can easily be incorporated into the model without increasing numerical difficulty.

The above technique can efficiently handle homogeneous chemical reactions in the bulk solution. However, for heterogeneous reactions, such as FeCO₃ formation and dissolution that occur only on existing solid surfaces, special consideration is required. The FeCO₃ precipitation and dissolution act as the sink and source for Fe²⁺ and CO₃²⁻ respectively. When supersaturation is greater than 1, net FeCO₃ precipitation occurs which consumes Fe²⁺ and CO₃²⁻; when it is less than 1, net FeCO₃ dissolution takes place leading to increased concentrations of Fe²⁺ and CO₃²⁻.

For the precipitation process, the rates of consumption of species read:

$$R_{Fe^{2+}} = R_{CO_3^{2-}} = -R_{prec} \quad (72)$$

For the dissolution process, the rates of generation of species can be obtained by:

$$R_{Fe^{2+}} = R_{CO_3^{2-}} = R_{diss} \quad (73)$$

The precipitation rate of FeCO₃ is given by Sun as:⁹⁹

$$R_{prec} = e^{A - \frac{B}{RT}} \frac{S}{V} K_{sp} (SS - 1) \quad (74)$$

Where R_{prec} is the precipitation rate in mol/m³.s; A and B are constants taking the values of 28.2 and 64.85 respectively; $\frac{S}{V}$ is the surface volume ratio of the FeCO₃ in 1/m; K_{sp} is the solubility limit of FeCO₃ in (mol/L)², which can be obtained by:⁹⁹

$$\log K_{sp} = -59.3498 - 0.041377T - \frac{2.1963}{T} + 24.5724 \log T + 2.5181T^{0.5} - 0.65 \quad (75)$$

Where I is the ionic strength in mol/L and T is the temperature in K; SS is the supersaturation of $FeCO_3$ defined as:

$$SS = \frac{c_{Fe^{2+}}c_{CO_3^{2-}}}{K_{sp}} \quad (76)$$

The dissolution rate of $FeCO_3$ is developed based on the assumption that the dissolution process is always under mass transfer control. This assumption is deemed valid considering that dissolution rate is usually much faster than precipitation rate (5 folds higher or more).¹⁰⁰ This assumption implies saturation of $FeCO_3$ at a dissolving $FeCO_3$ surface ($SS=1$), since fast dissolution would cause accumulation of Fe^{2+} and CO_3^{2-} on the surface; the extent of accumulation, however, cannot exceed the solubility limit of $FeCO_3$, otherwise, $FeCO_3$ precipitation would occur. This assumption allows the derivation of the equation for $FeCO_3$ layer dissolution kinetics as shown by Equation (77). The equation was derived by Lee¹⁰¹ and detailed equation derivation is shown in Appendix 1 for reference.

$$R_{diss} = \frac{-(c_{Fe^{2+}} + c_{CO_3^{2-}}) + \sqrt{(c_{Fe^{2+}} - c_{CO_3^{2-}})^2 + 4K_{sp}}}{2\Delta t} \quad (77)$$

Where R_{diss} is the dissolution rate of $FeCO_3$ in mol/m³.s; Δt is the time interval in seconds over which dissolution occurs.

4.4.2 Electrochemical reactions

Electrochemical reactions considered in this model include:





Electrochemical reactions are heterogeneous reactions that take place only on conductive surfaces (such as a metal surface) in a spontaneous corrosion process. The reaction rates are a function of surface water chemistry and potential. Due to the involvement of electrochemical potential, the reaction rate of an electrochemical reaction is commonly expressed in terms of current density, rather than flux as in a chemical reaction. In a carbon steel localized corrosion scenario, both an active surface (anode) and a pseudo-passive surface (cathode) are present. The different nature of these steel surfaces can lead to significant differences in electrochemical reaction kinetics. Therefore, efforts were made in this work to identify the difference in electrochemical reaction kinetics on active and pseudo-passive surfaces and to develop models to calculate the reaction kinetics on different surfaces.

4.4.2.1 Active surface

In the previously developed uniform corrosion model (MULTICORP V4), the Tafel equation is used to calculate the current densities of electrochemical reactions,¹³ as shown in Equation (82):

$$i = \pm i_o \times 10^{\pm \frac{E - E_o}{b}} \quad (82)$$

Where i is the current density, i_o is a reference current density, E is the corrosion potential, E_o is a reference potential and b is the Tafel slope.

This equation is considered insufficient in modeling localized corrosion because the potentials in a galvanic cell must not exceed the lower and upper limits determined by the reversible potentials of anodic and cathodic reactions respectively. The Tafel equation, however, is not able to provide such limits, at which current becomes zero once the potential reaches the reversible potential. Apparently, the Tafel equation could lead to overprediction of potential on the cathode side and underprediction of potential on anode sides. In this model, the Butler-Volmer equation is used instead to calculate the electrochemical reaction rate in order to yield a more realistic description of potential and current distribution in the galvanic cell. A Butler-Volmer equation reads:

$$i = i_o \left(10^{\frac{E - E_{rev}}{b_a}} - 10^{\frac{E_{rev} - E}{b_c}} \right) \quad (83)$$

Where i is the current density in A/m²; i_o is the exchange current density in A/m²; E is the potential of metal in V; E_{rev} is the reversible potential in V; b_a and b_c are the Tafel slopes for the anodic and cathodic part of an electrochemical reaction, respectively, in V/decade. The difference between the Tafel and Butler-Volmer equations in calculating potential and current distribution can be schematically illustrated in Evans diagrams, as shown in Figure 12 and Figure 13.

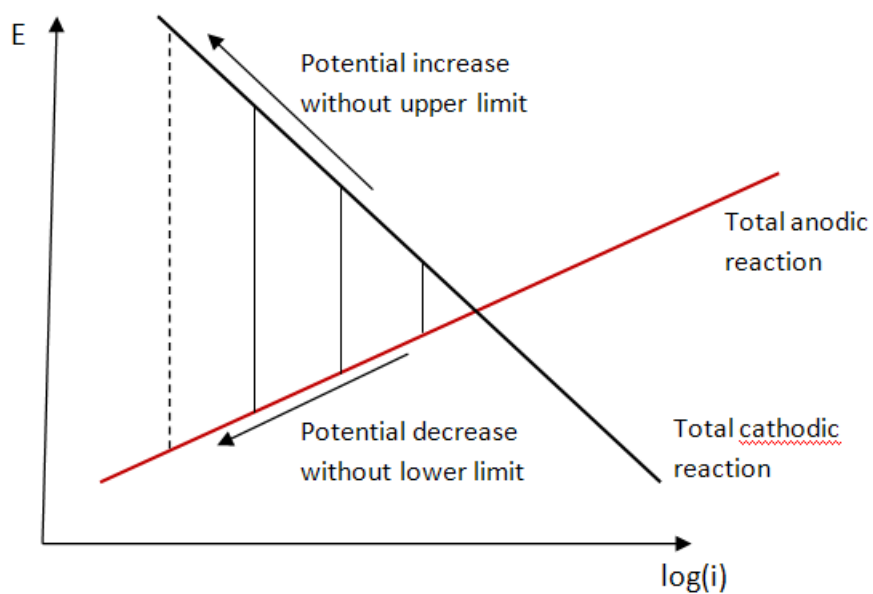


Figure 12. Potential/current distribution predicted by the Tafel equation.

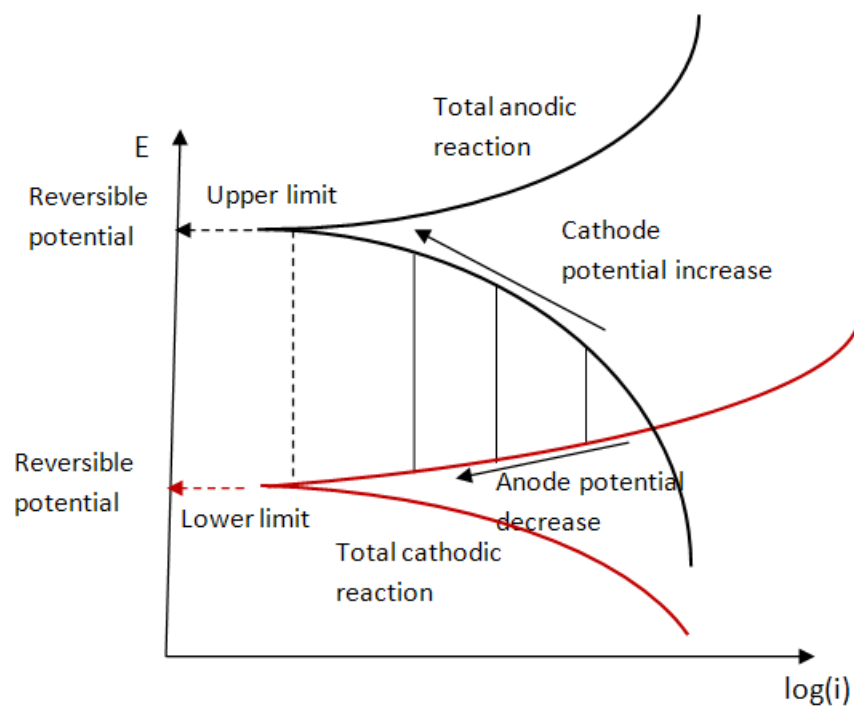


Figure 13. Potential/current distribution predicted by the Butler-Volmer equation.

As argued by Nešić *et al.*, all cathodic reactions in a CO₂ aqueous solution are thermodynamically equivalent to H⁺ reduction (Reaction (79)).¹³ Therefore, the reversible potential of all cathodic reactions can be calculated using the Nernst equation:

$$E_{rev} = E_{rev}^0 - \frac{RT}{F} \ln \frac{p_{H_2}^{0.5}}{c_{H^+}} \quad (87)$$

Where E_{rev}^0 is the reversible potential of H⁺ reduction at standard conditions; p_{H_2} is the partial pressure of hydrogen gas on the steel surface in bar and c_{H^+} is H⁺ concentration at the steel surface in mol/L.

For an anodic reaction, the reversible potential is given by the Nernst equation as:

$$E_{rev} = E_{rev}^0 - \frac{RT}{2F} \ln \frac{1}{c_{Fe^{2+}}} \quad (84)$$

where $c_{Fe^{2+}}$ is the surface concentration of Fe²⁺ in mol/L.

The exchange current densities of electrochemical reactions are functions of the surface concentrations of corresponding species. In the earlier studies, an arbitrary value of current density and potential along the E-i curves of corresponding reactions have been used to formulate the Tafel equations for anodic and cathodic reactions, as shown in Table 1. In this work, in order to construct the Butler-Volmer equation, true reversible potential and exchange current density must be used. The exchange current density of each electrochemical reaction can be obtained with the knowledge of the reversible potential, the reference current and potential along the E-i curve and the Tafel slope. The detailed equation derivation for exchange current densities of anodic and cathodic

reactions are shown in Appendices 2 and 3, respectively. The parameters used for calculating the electrochemical reaction kinetics in this model are listed in Table 2. Compared to the Tafel equation used in the previous model, partial pressure of hydrogen gas here affects both the reversible potential and the exchange current density of the cathodic reactions; Fe^{2+} concentration, on the other hand, impacts the reversible potential and exchange current density of the anodic reaction. This is not surprising because, with the Butler-Volmer equation, the cathodic and anodic reaction kinetics thereby become functions of hydrogen gas oxidation and Fe^{2+} deposition respectively.

Table 1. The electrochemical parameters used for Tafel equation* in the previous model

where the current density is calculated as $i = \pm i_0 \times 10^{\pm \frac{E-E_0}{b}}$

Reaction	$H^+ + e \rightarrow \frac{1}{2}H_2$
Reference current density i_0 /A/m ²	$0.05 \left(\frac{c_{H^+}}{10^{-4}} \right)^{0.5} e^{\frac{-3 \times 10^4}{R} \left(\frac{1}{T} - \frac{1}{25+273.15} \right)}$
Reference potential (E_0)/V	$-\frac{2.303RT}{F} pH$
Tafel slope (b) /V/decade	$\frac{2.303RT}{0.5F}$
Reaction	$H_2CO_3 + e \rightarrow \frac{1}{2}H_2 + HCO_3^-$
Reference current density i_0 /A/m ²	$0.06 \left(\frac{c_{H^+}}{10^{-5}} \right)^{-0.5} \left(\frac{c_{H_2CO_3}}{10^{-4}} \right)^1 e^{\frac{-5 \times 10^4}{R} \left(\frac{1}{T} - \frac{1}{20+273.15} \right)}$
Reference potential (E_0)/V	$-\frac{2.303RT}{F} pH$
Tafel slope (b) /V/decade	$\frac{2.303RT}{0.5F}$
Reaction	$HAc + e \rightarrow \frac{1}{2}H_2 + Ac^-$
Reference current density i_0 /A/m ²	$0.04 \left(\frac{c_{HAc}}{1.42 \times 10^{-3}} \right)^{0.5} e^{\frac{-7.1 \times 10^4}{R} \left(\frac{1}{T} - \frac{1}{20+273.15} \right)}$

Reference potential (E_o)/V	$-\frac{2.303RT}{F}pH$
Tafel slope (b) /V/decade	$\frac{2.303RT}{0.5F}$
Reaction	$Fe \rightarrow Fe^{2+} + 2e$
Reference current density i_o /A/m ²	$1 \cdot e^{-\frac{3.75 \times 10^4}{R} \left(\frac{1}{T} - \frac{1}{(25+273.15)} \right)}$
Reference potential (E_o)/V	-0.488
Tafel slope (b) /V/decade	$\frac{2.303RT}{1.5F}$

* In this Table, concentration is steel surface concentration in the unit of mol/L; T is absolute temperature in K; R is universal gas constant 8.314J/mol.K and F is Faraday constant 96485 C/mol.

Table 2. The electrochemical parameters used for Butler-Volmer equation* in the current

model where current density is calculated as $i = i_o \left(10^{\frac{E-E_{rev}}{b_a}} - 10^{\frac{E_{rev}-E}{b_c}} \right)$

Reaction	$H^+ + e \leftrightarrow \frac{1}{2}H_2$
exchange current density i_o /A/m ²	$0.05 \left(\frac{c_{H^+}}{10^{-4}} \right)^{0.5} p_{H_2}^{0.25} e^{-\frac{3 \times 10^4}{R} \left(\frac{1}{T} - \frac{1}{(25+273.15)} \right)}$
reversible potential (E_{rev})/V	$E_{rev} = E_{rev}^o - \frac{RT}{F} \ln \frac{p_{H_2}^{0.5}}{c_{H^+}}$
Anodic Tafel slope (b_a) /V/decade	$\frac{2.303RT}{0.5F}$
cathodic Tafel slope (b_c) /V/decade	$\frac{2.303RT}{0.5F}$
Reaction	$H_2CO_3 + e \leftrightarrow \frac{1}{2}H_2 + HCO_3^-$
exchange current density i_o /A/m ²	$0.06 \left(\frac{c_{H^+}}{10^{-5}} \right)^{-0.5} \left(\frac{c_{H_2CO_3}}{10^{-4}} \right)^1 p_{H_2}^{0.25} e^{-\frac{5 \times 10^4}{R} \left(\frac{1}{T} - \frac{1}{(20+273.15)} \right)}$
reversible potential (E_{rev})/V	$E_{rev} = E_{rev}^o - \frac{RT}{F} \ln \frac{p_{H_2}^{0.5}}{c_{H^+}}$
Anodic Tafel slope (b_a) /V/decade	$\frac{2.303RT}{0.5F}$
cathodic Tafel slope (b_c) /V/decade	$\frac{2.303RT}{0.5F}$
Reaction	$HAc + e \leftrightarrow \frac{1}{2}H_2 + Ac^-$

exchange current density i_0 /A/m ²	$0.04 \left(\frac{c_{HAc}}{1.42 \times 10^{-3}} \right)^{0.5} p_{H_2}^{0.25} e^{\frac{-7.1 \times 10^4}{R} \left(\frac{1}{T} - \frac{1}{(20+273.15)} \right)}$
reversible potential (E_{rev})/V	$E_{rev} = E_{rev}^o - \frac{RT}{F} \ln \frac{p_{H_2}^{0.5}}{c_{H^+}}$
Anodic Tafel slope (b_a)/V/decade	$\frac{2.303RT}{0.5F}$
cathodic Tafel slope (b_c)/V/decade	$\frac{2.303RT}{0.5F}$

Table 2: continued.

Reaction	$Fe \leftrightarrow Fe^{2+} + 2e$
exchange current density i_0 /A/m ²	$e^{-\frac{835.6}{T}} \cdot c_{Fe^{2+}}^{0.75} e^{\frac{-3.75 \times 10^4}{R} \left(\frac{1}{T} - \frac{1}{(25+273.15)} \right)}$
reversible potential (E_{rev})/V	$E_{rev} = E_{rev}^o - \frac{RT}{2F} \ln \frac{1}{c_{Fe^{2+}}}$
Anodic Tafel slope (b_a) /V/decade	$\frac{2.303RT}{1.5F}$
cathodic Tafel slope (b_c) /V/decade	$\frac{2.303RT}{0.5F}$

* In this table, concentration is steel surface concentration in the unit of mol/L; T is absolute temperature in K; R is universal gas constant 8.314J/mol.K and F is Faraday constant 96485 C/mol.

4.4.2.2 Pseudo-passive surface

Cathodic reactions

Upon pseudo-passivation, the carbon steel surface is covered by a thin but dense and protective oxide film. Unlike an active carbon steel surface, the pseudo-passive film is electrically semi-conductive. It is well-known that semi-conductivity of a passive film dramatically alters the anodic polarization behavior; however, whether a cathodic reaction is impacted on a passive film deserves more attention, since significant changes in cathodic reaction kinetics would result in a different potential on the cathode surface, thus influencing the galvanic effect. In this work, efforts have been made to compare the cathodic reaction rate on pseudo-passive and active steel surfaces. A direct comparison for cathodic reaction kinetics between pseudo-passive and active carbon steel is difficult to achieve through commonly-used electrochemical techniques such as potentiodynamic sweep. This is because the corrosion of carbon steel in CO₂ environments is often subject to mixed charge transfer and chemical reaction limiting control at the corrosion potential;

potentiodynamic sweep cannot provide direct evidence as to the charge transfer rate of a cathodic reaction for an active steel surface. The significant difference in open circuit potential of active and pseudo-passive carbon steel surfaces further prohibits the direct comparison of cathodic reactions. An example of potentiodynamic sweeps performed for stainless steel (a surrogate passive surface) and carbon steel (an active surface) is schematically shown in Figure 14. The overlap of two cathodic sweep curves occurs in the current limiting region, which is not surprising, as bulk concentration and hydrodynamic conditions are the same in both cases. Clearly, no conclusion can be deduced from this figure as to the similarity or dissimilarity of the charge transfer kinetics for cathodic reactions on the two different surfaces. A different strategy is adopted in this work in order to fill in the missing information. A simulation was performed using FREECORP (presented below), a software capable of generating the Evans diagram of a system in which potential vs. current density of electrochemical reactions can be shown. By comparing the experimentally-obtained potentiodynamic sweep for stainless steel with the total cathodic polarization curve generated from the software for carbon steel under the same conditions (as shown in Figure 15), it is evident that the cathodic reaction rate on stainless steel is not significantly different from that on the carbon steel surface. The comparison was repeated under different conditions and similar behavior was observed, as demonstrated in Figure 16. The experiments indicate that the thin passive film existing on the stainless steel surface (mostly chromium oxide) does not remarkably alter the cathodic reaction kinetics. This suggests that cathodic reaction rates are not heavily affected by the state of metal surface. The similar behavior was also reported in

an independent study¹⁰² which shows the similarity of cathodic reaction rates on carbon steel and Alloy 625 surfaces. Therefore, it can be deduced that a pseudo-passive film formed on carbon steel would not significantly affect cathodic reaction. For practical purposes, cathodic reaction rates on pseudo-passive surfaces can be evaluated in the same way as for active surfaces, which are presented in Table 2.

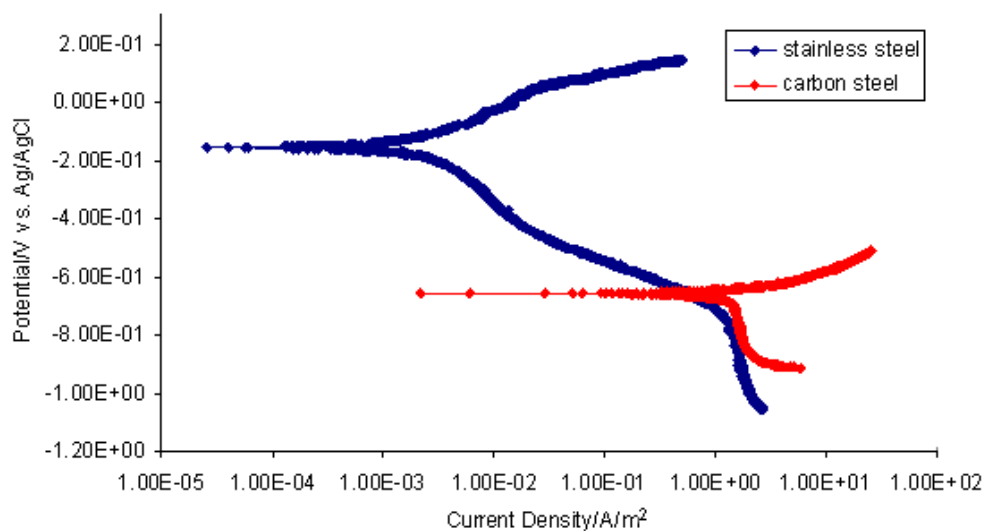


Figure 14. Potentiodynamic sweep on stainless steel and carbon steel. Test condition: $T=25^{\circ}\text{C}$, $\text{pH}=4.1$, $\text{pCO}_2=1$ bar, stagnant solution.

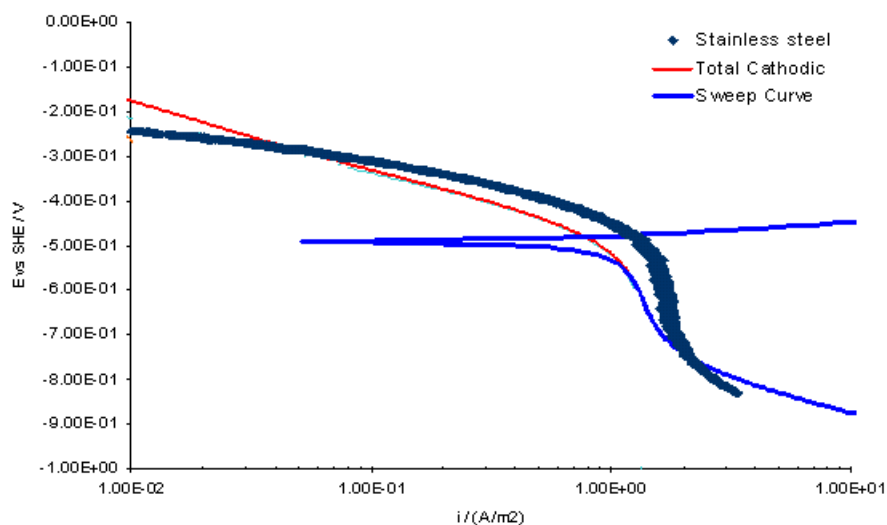


Figure 15. Comparison of potentiodynamic sweep of stainless steel with polarization curves of carbon steel generated from the software. Test conditions: $T=25^{\circ}\text{C}$, $\text{pH}=4$, $\text{NaCl}=1\%$, stagnant solution.

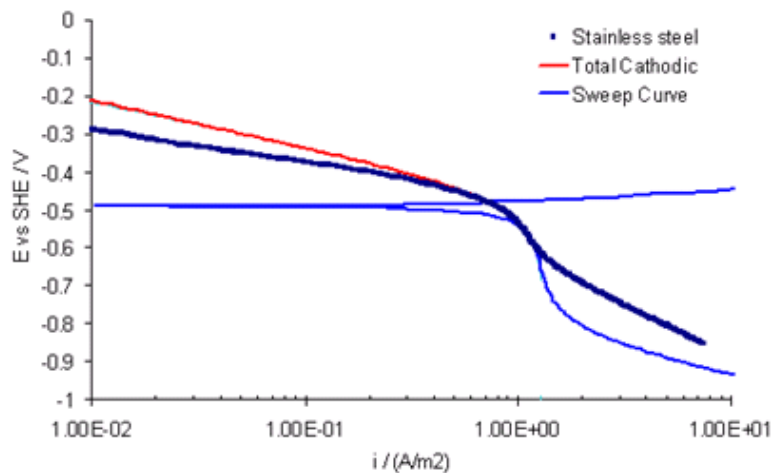


Figure 16. Comparison of potentiodynamic sweep of stainless steel with Polarization curves of carbon steel generated from FREECORP. Test condition: $T=25^{\circ}\text{C}$, $\text{pH}=5$, $\text{NaCl}=1\%$, stagnant solution.

Anodic reaction

Anodic reaction kinetics on a pseudo-passive surface are key in determining localized corrosion rates, as pseudo-passive current density causes a large shift of metal potential towards the positive direction and creates a potential difference between the active surface of the anode and the pseudo-passive surface of the cathode. The smaller the pseudo-passive current density is, the higher the potential difference will be, which translates to a higher localized corrosion rate. Therefore, it is important to understand what parameters affect pseudo-passive current density and how to calculate it.

As the first step in this study, electrochemical tests were conducted in the hope of determining important environmental factors that affect pseudo-passive current density and providing a guide for modeling pseudo-passive current density as a function of relating parameters.

A cyclic polarization technique was utilized in this work to measure the pseudo-passive current density under various conditions. The test procedure follows the ASTM standard G61-86.¹⁰³

In addition to potential, pH, temperature and chloride concentration have been reported to play major roles in determining pseudo-passive current density. In order to understand the effect of individual parameters and any interactions among them, a factorial experimental design technique¹⁰⁴ was adopted to help with test matrix design and the statistical analysis of test results. The test procedure, results and results analysis are presented in Appendix 4.

The results of the factorial effect analysis on pseudo-passive current density are summarized in Table 3. According to the factorial experimental design theory, a higher

value of effect (irrespective of its sign) signifies more effect of the corresponding parameter on the pseudo-passive current density. Clearly, pH and temperature have the most significant effect on pseudo-passive current density, while the effect of Cl^- concentration is marginal. The interaction between pH and temperature seems to be another important factor. Based on the experiments, it can be concluded that the effect of Cl^- concentration on pseudo-passive current density of carbon steel in CO_2 environments is negligible. Judging from the sign of the effects, it is evident that higher pH leads to a smaller pseudo-passive current density, while higher temperature causes an increase in pseudo-passive current density. This implies that a more protective pseudo-passive film is formed under higher pH and lower temperature. It should be mentioned that, as an electrochemical parameter, pseudo-passive current density is inherently related to potential. Therefore, the effect of potential was intentionally excluded in the test matrix in order to reduce the cost and numbers of experiments.

Table 3. Effect of factors on pseudo-passive current density

Factors	Effect
pH	-23.15
T	17.99
pH & T	-18.26
$[\text{Cl}^-]$	2.64
pH & $[\text{Cl}^-]$	-2.61
T & $[\text{Cl}^-]$	5.89
pH & T & $[\text{Cl}^-]$	-5.86

Equipped with the understanding gained from the experiments, a mechanistic model was developed to calculate the pseudo-passive current density as related to pH,

temperature and potential. Apparently, a constant value of pseudo-passive current density is not sufficient to satisfy the modeling needs of a complex CO₂ corrosion system, as surface conditions on a pseudo-passive surface, including pH and potential, change with time. A mechanistic model is expected to provide a more appropriate response of pseudo-passive current to change in environmental parameters.

In this work, pseudo-passive current density is determined by implementing the Point Defect Model, originally developed by Macdonald *et al.*²⁸⁻³¹ and modified by Camacho *et al.*,³⁸ into the carbon steel/CO₂ system. Detailed model development is given in Appendix 5. The model was calibrated against an experimental database in order to obtain the values of parameters used in the model equation. The database contains a number of measured galvanic current densities under different conditions, which were obtained from artificial pit tests.¹⁰⁵ Some comparisons for the predicted and measured galvanic current density are illustrated in section 4.7.2. The derived equation reads:

$$i_{ss} = 2F \cdot 10^{-4} \exp \left[\frac{-0.95(-0.04V + 0.014pH)F}{RT} \right] \quad (85)$$

It can be seen that the model is consistent with the results of factorial experimental analysis. Potential, pH and temperature are the three parameters included in the model equation; and higher pH and lower temperature would lead to a smaller pseudo-passive current density. Equation (85) also suggests that pseudo-passive current density increases with increasing potential, which qualitatively agrees with the classic electrochemical theory.

4.4.3 Mass transport

Mass transport of species in a dilute aqueous solution is governed by the law of mass conservation, also known as Fick's second law. In the presence of porous film, the equation has to be modified to take into account the characteristics (e.g. porosity and tortuosity) of the film:¹³

$$\frac{\partial \varepsilon c_j}{\partial t} = -\nabla \cdot \kappa N_j + \varepsilon R_j \quad (86)$$

Where c_j is the concentration of species, ε is the porosity of FeCO_3 layer, κ is permeability of FeCO_3 layer which is defined as the product of porosity (ε) and tortuosity (ζ) of the film; t is time; N_j is the flux of species and R_j is chemical reaction rate of species.

It should be noted that Equation (86) is a universal equation describing mass transport of species in the solution with and without a porous FeCO_3 layer. In the absence of FeCO_3 layer, the porosity and tortuosity of FeCO_3 in Equation (86) both simply take the constant value of 1.

The first term on the RHS of equation (86), flux of species, is given by:

$$N_j = -D_j^m \nabla c_j - z_j u_j F c_j \nabla \phi + c_j v \quad (87)$$

Where D_j^m is the molecular diffusion coefficient; z_j is the electrical charge; ϕ is the electrostatic potential in the solution; F is the faraday constant; v is the in-situ flow velocity and u_j is the mobility of species. For a dilute solution, the value of mobility is given by:

$$u_j = \frac{D_j^m}{RT} \quad (88)$$

Where R is universal gas constant and T is absolute temperature.

Equation (87) suggests that the flux of species is contributed by three components: molecular diffusion, electro-migration and convection.

In a dilute solution, species can freely diffuse in the solution without coupling with each other. Therefore, modeling molecular diffusion is straightforward, requiring only the knowledge of a molecular diffusion coefficient.

Table 4 lists the molecular diffusion coefficients of species commonly existing in the corrosion system of interest at 25°C. Most of the diffusion coefficients were collected and compiled by Nešić et.al,¹³ with the exception of hydrogen gas. Hydrogen gas is simulated in this model to yield the partial pressure of hydrogen gas at the steel surface, which is required by the Butler-Volmer equation for describing the electrochemical reaction kinetics. The diffusion coefficients are adjusted as functions of temperature and solution viscosity using Einstein-Stokes law:

$$D_j = D_{ref} \frac{T}{T_{ref}} \frac{\mu_{ref}}{\mu} \quad (89)$$

Where D_{ref} is the diffusion coefficient at reference temperature; T and T_{ref} are system temperature and reference temperature in K respectively; μ and μ_{ref} are solution viscosity under system and reference conditions in Pa.s, respectively.

Table 4. Species commonly existing in the system of interest, and the corresponding diffusion coefficient at 25°C

Species	Diffusion coefficient/(m ² /s)	Reference number
CO ₂	1.96×10^{-9}	106
H ₂ CO ₃	2.00×10^{-9}	107
HCO ₃ ⁻	1.105×10^{-9}	108
CO ₃ ²⁻	0.92×10^{-9}	107
H ⁺	9.312×10^{-9}	108
OH ⁻	5.26×10^{-9}	108
Fe ²⁺	0.72×10^{-9}	107
Cl ⁻	2.032×10^{-9}	108
Na ⁺	1.334×10^{-9}	108
Ca ²⁺	0.792×10^{-9}	108
Ba ²⁺	0.847×10^{-9}	108
Sr ²⁺	0.791×10^{-9}	108
HAc	1.24×10^{-9}	106
Ac ⁻	1.089×10^{-9}	108
H ₂ S	1.61×10^{-9}	106
HS ⁻	2.00×10^{-9}	13
S ²⁻	2.00×10^{-9}	13
HSO ₄ ⁻	1.33×10^{-9}	108
SO ₄ ²⁻	1.065×10^{-9}	108
H ₂	1.35×10^{-9}	109

Direct solution for the convection term in Equation (87) is not as straightforward as molecular diffusion since it requires knowledge of the in-situ velocity, which is typically obtained by performing a computational flow dynamics (CFD) simulation. This process is usually time-consuming and poses enormous numerical difficulty when

coupled with mass transport simulation. This is mainly due to the fact that the flow boundary layer is much thicker than the diffusion boundary layer for a water system. Therefore, special solving strategies must be pursued for proper coupling of CFD and mass transport simulation. To reduce the numerical effort and expedite the calculation, Nešić *et al.* have suggested a simplified way to estimate the convection effect,¹³ which is adopted in this model. This is achieved by replacing the convective flux with a turbulent diffusive-like flux in the computation domain, as shown in Equation (90):

$$c_j v = -D_j^t \frac{\partial c_j}{\partial x} \quad (90)$$

Where D_j^t is the turbulent diffusion coefficient, which is a function of the distance from the solid surface (bare steel or FeCO_3 layer) and can be calculated as:

$$D_j^t = \begin{cases} 0 & \text{for } x < \delta_f \\ 0.18 \left(\frac{x - \delta_f}{\delta - \delta_f} \right)^3 \frac{\mu}{\rho} & \text{for } x > \delta_f \end{cases} \quad (91)$$

Where δ is the diffusion layer thickness in m; δ_f is the thickness of FeCO_3 layer in m; and x the distance away from solid surface in m.

Combining Equations (87) and (90), the fluxes of species can then be calculated by:

$$N_j = -D_j^{eff} \nabla c_j - z_j u_j F c_j \nabla \phi \quad (92)$$

Where D_j^{eff} is the effective diffusion coefficient account for both molecular diffusion and turbulent diffusion effects and is given by $D_j^m + D_j^t$.

Within the porous FeCO_3 layer it is argued that there is no flow and turbulence and species can travel through the pores driven only by molecular diffusion and electro-migration.¹³

The flux due to electro-migration can usually be neglected in cases of uniform corrosion. The potential gradient generated by different diffusion rates of species is easily annihilated by large amounts of supporting species, such as Na^+ and Cl^- . However, it would be unacceptable to neglect the electro-migration effect in localized corrosion due to the fact that significant potential difference might exist between anode and cathode which could drive charged species to move at appreciably different rates.

The second term on the RHS of Equation (86) accounts for chemical reaction rates of species. As shown earlier, various species are coupled together in Reactions (52) through (55); therefore, mass transport equations for various species have to be solved simultaneously. The mathematical technique used to account for the chemical reaction rates is given by Nešić *et al.*¹³ and has been previously described in section 4.4.1.

Calculation of mass transport is carried out in a pre-defined domain, the height of which equals the thickness of diffusion boundary layer. The thickness of diffusion boundary layer is given as:¹¹⁰

$$\delta - \delta_f = 25 \text{Re}^{-7/8} d \quad (93)$$

Where δ is the thickness of diffusion boundary layer, δ_f is the thickness of FeCO_3 layer, Re is the Reynolds number and d is the hydraulic diameter.

Although a 2D domain would be preferable for simulating a galvanic cell, mass transport equations are solved in two 1D domains for the anode and the cathode

separately, stretching from the steel surface to the diffusion boundary layer/ bulk solution interface. Anode and cathode are then coupled together to solve the potential/current distribution in a 2D domain. This simplification is made due to the lack of CFD (computational fluid dynamic) simulation in the model, which would be required for the convective flow in the streamwise direction (convective flow in normal-wall direction can be approximated by turbulent diffusivity) if a 2D domain were to be used for mass transport simulation. This simplification is considered acceptable because the concentration gradients in the direction normal to the metal surface are much larger than that those in the streamwise direction. Therefore, neglecting mass transport in the direction parallel to the metal surface would not significantly affect the electrochemical reaction kinetics on the metal surface.

Outside the diffusion boundary layer, all species are considered to be well-mixed by turbulent flow; therefore, little concentration gradients are expected. For this reason, the boundary conditions for the upper end of the computational domain are taken as the bulk concentrations of species. The fluxes of species are used to specify the boundary condition at the metal surface. For species not involved in electrochemical reactions, zero flux is imposed; for corrosion-related species, e.g. H^+ , H_2 , H_2CO_3 , HCO_3^- , HAc , Ac^- and Fe^{2+} , etc., fluxes can be obtained from electrochemical reaction rates:

$$N_j = \frac{i_j}{z_j F} \quad (94)$$

Where i_j is the electrochemical reaction rate, which is dependent on the surface concentration of corrosive species and on the metal surface potential, as illustrated in Table 2.

As a transient simulation, initial conditions for mass transport equations are taken to be the concentrations with which chemical equilibrium is satisfied.

Figure 17 shows the computational domain together with the governing equation used in the model.

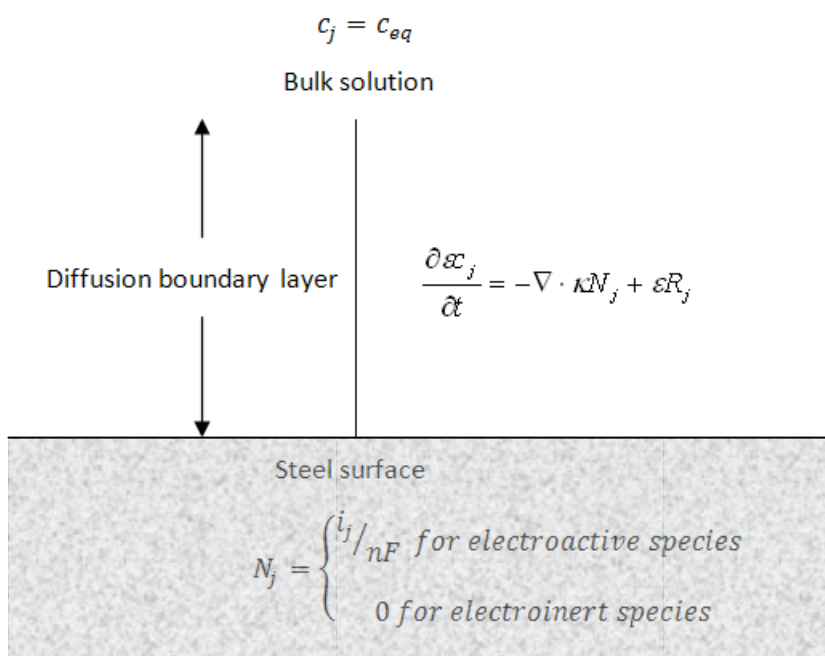


Figure 17. Illustration of computation domain and governing equation for mass transport simulation.

4.4.4 $FeCO_3$ layer Growth

The equation governing $FeCO_3$ layer growth was previously developed by Nešić *et al.*¹⁴ based on mass conservation of $FeCO_3$ in the solution, as shown in Equation (95).

In this equation FeCO_3 layer growth is characterized by the change in porosity. The higher the porosity, the more porous the FeCO_3 layer, and vice versa. The value of porosity is bounded between 0 and 1. A value of 1 indicates that no FeCO_3 layer is present, while a value of 0 implies that the space is completely sealed by FeCO_3 layer and no species can travel through. This equation suggests that growth of FeCO_3 layer is attributed to two factors: FeCO_3 precipitation and corrosion. Depending on the relative values of these two terms, FeCO_3 layer can be either protective or non-protective, which is consistent with the concept of scaling tendency.⁶⁵ It is important to note that when supersaturation of FeCO_3 is less than 1, the precipitation rate in Equation (95) is replaced with the dissolution rate. Detailed information regarding this equation can be found in the original paper¹⁴ and will not be described here.

$$\frac{\partial \varepsilon}{\partial t} = -\frac{M_{\text{FeCO}_3(S)}}{\rho_{\text{FeCO}_3(S)}} R_{\text{FeCO}_3(S)} - CR \frac{\partial \varepsilon}{\partial x} \quad (95)$$

Where $M_{\text{FeCO}_3(S)}$ and $\rho_{\text{FeCO}_3(S)}$ are the molar mass and density of FeCO_3 respectively, CR is the corrosion rate in proper unit, ε is the porosity of FeCO_3 layer, t and x are the coordinates in time and space.

As explained by Nešić *et al.*, the second term on the RHS of Equation (95) accounts for the moving boundary created by the corrosion process, which poses a convective-like effect in the equation.¹⁴ It is well-recognized that a convective term contributes to numerical instability in solving a partial differential equation. The simplest and most common way to avoid numerical instability is by implementing a first-order upwind scheme in which interfacial parameters are evaluated by the corresponding values

in the neighboring upstream grid.¹¹¹ However, this scheme has only first-order accuracy and could easily lead to “false diffusion”.¹¹¹ As argued by Lee,¹¹² for equations lacking a physical diffusion term, a simple upwinding scheme would generate significant numerical diffusion and introduce an unacceptable level of numerical error due to the hyperbolic nature of the equation and the very small CFL number ($CFL = CR \cdot \Delta t / \Delta x \approx 10^{-3}$). In recent years, much attention has been directed to this issue and a number of higher-order schemes have been proposed to achieve both accuracy and stability associated with convective terms. In the previous model, the second-order Koren scheme with a flux limiter function was used to deal with the convective term (CR) in Equation (95). In this work, efforts were made to investigate the performance of this scheme against other higher-order schemes. A total of 6 schemes (2nd order upwind,^{113,114} KOREN,^{115,116} HOAB,¹¹⁷ Superbee,¹¹⁸ OSPRE,¹¹⁹ MUSCL^{120,121}) are compared in the context of Equation (95). All of the schemes evaluate the interfacial parameter using a specific form of second-order flux limiter functions; the implementation of these schemes is well-explained by Waterson and Deconinck.¹²² Figure 18 shows one example of predictions made using various schemes. Figure 19 shows the corresponding corrosion rate history predicted using different schemes. It can be seen that, apart from the second-order upwind, all schemes provide comparable predictions on FeCO₃ layer morphology and corrosion rate. Therefore it was decided that the Koren scheme should be kept in the model as a means of dealing with the convective term in Equation (95).

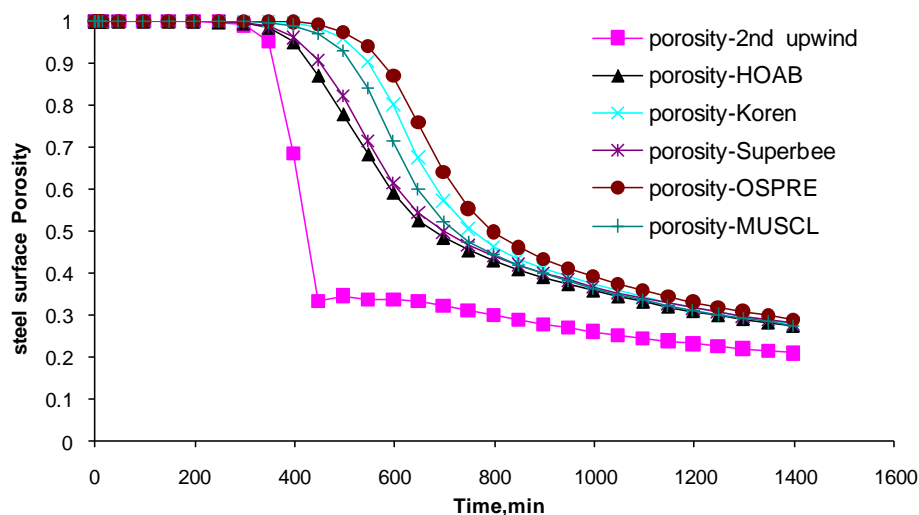


Figure 18. Comparison of surface porosity of FeCO_3 layer with different high-order schemes for convective term in Equation (95). Simulation condition: temperature 80°C , CO_2 partial pressure 1 bar, liquid velocity 1m/s , pipe diameter 0.1m , bulk super saturation of FeCO_3 about 0.5 and bulk pH 6.5.

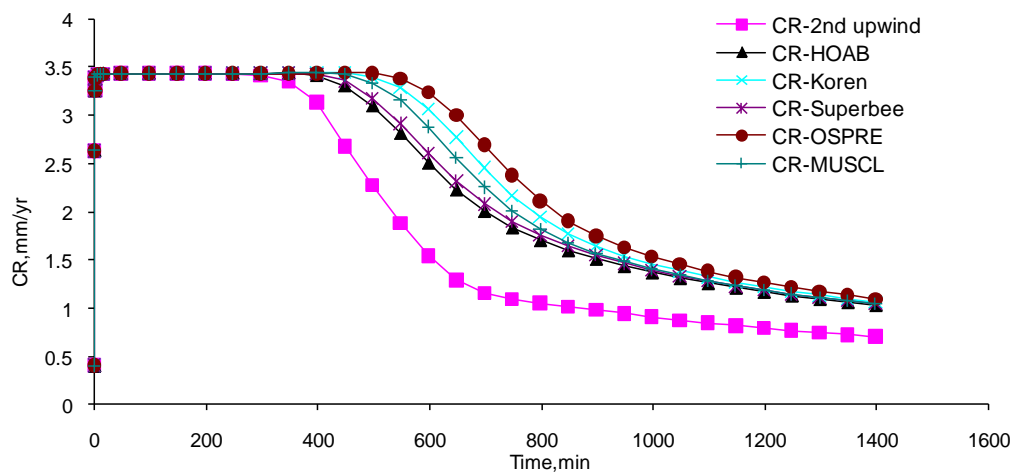


Figure 19. Comparison of corrosion rate with different high-order schemes for convective term in Equation (95). Simulation condition: temperature 80°C , CO_2 partial pressure 1 bar, liquid velocity 1m/s , pipe diameter 0.1m , bulk super saturation of FeCO_3 about 0.5 and bulk pH 6.5.

Equation (95) is solved in the same 1D domain as that used for the mass transport equation (Equation (86)). As argued by Nešić and Lee,¹⁴ although the detailed structure of a FeCO_3 layer in a 2D or even 3D domain would be hard to simulate, it is the overall effect of FeCO_3 layer that matters; therefore, 1D simulation of FeCO_3 layer growth is considered to be sufficient for CO_2 corrosion modeling.

At the FeCO_3 layer / metal surface interface, the porosity is considered to be 1, as the corrosion process, although slow, continuously creates voids underneath the FeCO_3 layer. At the other boundary (between the diffusion boundary layer and the bulk solution), it is assumed that no FeCO_3 can grow onto the boundary and out of the domain; therefore, porosity of FeCO_3 maintains at 1.

Figure 20 shows the computational domain along with the governing equation for FeCO_3 layer-growth simulation.

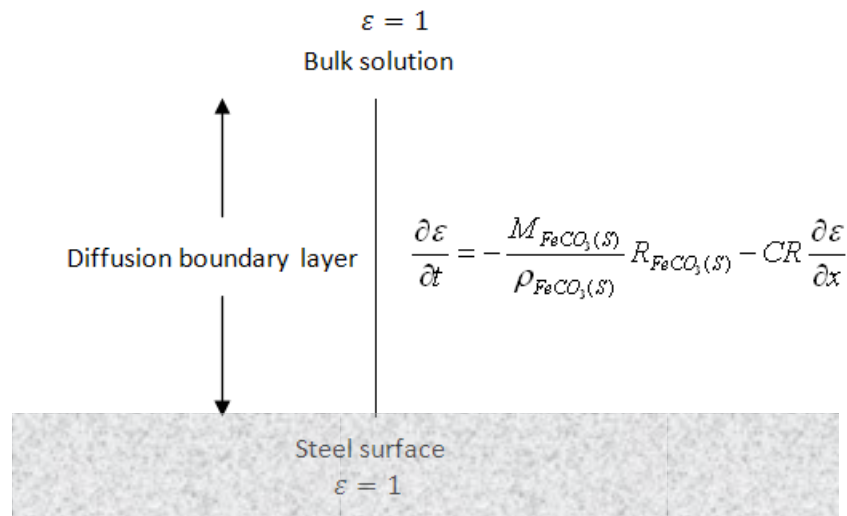
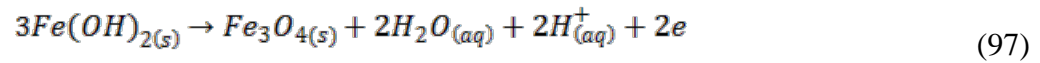
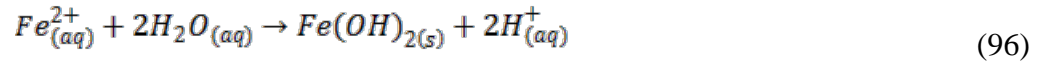


Figure 20. Illustration of computation domain and governing equation for FeCO_3 layer-growth simulation.

4.4.5 Pseudo-passivation/repassivation

Pseudo-passivation of carbon steel is considered to be a fast process, the occurrence of which is determined based on thermodynamic criteria. Pseudo-passivation of carbon steel in CO₂ environments has been ascribed to the existence of magnetite.¹² A two-step process leading to the generation of magnetite is proposed in this model, as shown in Equations (96) and (97):



The thermodynamic conditions for Reactions (96) and (97) can be evaluated in terms of Gibbs free energy. The Gibbs free energy of any species can be calculated based on the Gibbs-Helmholtz equation:

$$\Delta^{\circ}G(T) = \Delta H^{\circ}(T) - T \cdot \Delta^{\circ}S(T) \quad (98)$$

Where T is temperature in Kelvin, *G*, *H* and *S* are the Gibbs free energy, enthalpy and entropy, respectively.

As shown by Cheng *et al.*¹²³, Equation (98) can be transformed into a more practical form by relating heat capacity of the species to enthalpy and entropy:

$$G^{\circ}(T) - G^{\circ}(298) = \int_{298}^T c_p^{\circ}(T) dT - T \int_{298}^T \frac{c_p^{\circ}(T)}{T} dT - (T - 298) \cdot S^{\circ}(298) \quad (99)$$

Where $G^{\circ}(298) = \sum v \cdot G_f^{\circ}(298)$; $c_p^{\circ}(T)$ is heat capacity.

Empirical correlations are usually available for heat capacity of various species as a function of temperature, which can be found in many thermodynamic handbooks. For

ionic species involved in Reactions (96) and (97), namely, H^+ and Fe^{2+} , the correlation proposed by Criss and Cobble¹²⁴ is used:

$$c_p^\circ(T) = \frac{S^\circ(T) - S^\circ(298)}{\ln \frac{T}{298}} \quad (100)$$

$$S^\circ(T) = a(T) + b(T)S_{abs}^\circ(298) \quad (101)$$

$$S_{abs}^\circ(298) = S_{conv}^\circ(298) - 5.0 \cdot Z \quad (102)$$

Where a and b are entropy constants; S_{conv}° is the standard state entropy, S_{abs}° is the ionic entropy on the absolute scale and Z is the ionic charge.

Table 5 lists the entropy constants (a and b in Equation (101)) for different types of ionic species, originally given by Criss and Cobble.¹²⁴

Polynomial equations were obtained to calculate a and b by performing linear regression on the data listed in Table 5.

$$a(T) = 0.1374T - 42.602 \quad (103)$$

$$b(T) = -0.0017T + 1.5319 \quad (104)$$

Combining Equations (99) through (102), the Gibbs free energy of ionic species at any temperature is given by:¹²³

$$G^\circ(T) = G^\circ(298) + c_p^\circ(T) \left]_{298}^T \cdot \left(T - 298 - T \ln \frac{T}{298} \right) - (T - 298) \cdot S_{abs}^\circ(298) \quad (105)$$

For elements and compounds involved in Reactions (96) and (97) such as H_2O , Fe_3O_4 and $Fe(OH)_2$, heat capacity can be calculated as a polynomial function of temperature:

$$c_p = a + bT + \frac{c}{T^2} \quad (106)$$

By substituting Equation (106) into Equation (99), the Gibbs free energy of elements and compounds can be calculated as:¹²³

$$G^\circ(T) = G^\circ(298) + \left[\left(a + bT + \frac{c}{T^2} \right) \right] \frac{T}{298} - T \left[a \ln T + bT - \frac{c}{2T^2} \right] \frac{T}{298} - (T - 298) \cdot S^\circ(298) \quad (107)$$

The parameters used in this model to calculate the Gibbs free energy of the species involved in Reactions (96) and (97) are listed in Table 5.

Table 5. Parameters used for determination of the Gibbs free energy of species associated with pseudo-passivation

Species		Ionic species		Elements and compounds		
		H ⁺	Fe ²⁺	H ₂ O	Fe ₃ O ₄	Fe(OH) ₂
$G^\circ(298)$, x10 ⁻³ J/mol		0	-78.9	-237.129	-1012.57	-491.98
$S^\circ(298)$, J/mol.K		0	-137.7	70	146.1	88
$S^\circ(T)$, J/mol.K (EQ. (101))	a	0.1374T - 42.602		N/A	N/A	N/A
	b	-0.0017T + 1.5319		N/A	N/A	N/A
c_p , J/mol.K (EQ. (106))	a	N/A	N/A	20.4	91.6	116.1
	b x10 ³	N/A	N/A	109.2	202	8.6
	c x10 ⁻⁶	N/A	N/A	2.0	N/A	-2.9
$G^\circ(T)$, J/mol		EQ. (105)		EQ. (107)		

With Gibbs free energy available, the reversible potential for the electrochemical Reaction (97) or the chemical equilibrium constant for the chemical Reaction (96) at the

desired temperature can easily be calculated using Equations (108) and (109), respectively:

$$\Delta G^o = -nFE_{rev}^o \quad (108)$$

$$\Delta G^o = -RT \ln K_{eq} \quad (109)$$

The following equations are then used to determine the equilibrium pH or potential at which pseudo-passive film would form in the solution of interest by taking into account the effect of species concentrations:

$$K_{eq} = \frac{a_{H^+}^2}{a_{Fe^{2+}}} \quad (110)$$

$$E_{rev} = E_{rev}^o - \frac{RT}{nF} \ln \frac{a_{red}}{a_{ox}} \quad (111)$$

Where n is number of moles of electrons involved in the electrochemical reactions, E_{rev} and E_{rev}^o are the reversible potential for electrochemical reactions at real and standard conditions, respectively, and K_{eq} is the equilibrium constant for chemical reactions, a_{H^+} and $a_{Fe^{2+}}$ are the activities of H^+ and Fe^{2+} , respectively, which are estimated by the corresponding concentrations.

4.4.6 Pit initiation

Since the mechanism governing pit initiation for carbon steel in CO_2 environments is not clearly understood at present, in this model, a pit is initiated by artificially removing the protective layer at a randomly determined point in time. The stochastic nature of pit initiation is simulated using a Weibull distribution random function. Ascher¹²⁵ defines the initiation time for each of the pits on a coupon as the time

at which the first failure of the system occurs. Following his reasoning, the Weibull distribution function seems to be a good option for simulating random behavior of pit initiation as it is the most widely used function in the field of failure analysis. For example, DNV standard RP G101 describes a means of determining the probability of failure based on the Weibull distribution.¹²⁶ One of the unique advantages of Weibull distribution function is that, depending on the parameters provided, this function can exhibit the characteristics of other commonly used distribution functions such as normal, lognormal, etc. This provides flexibility in controlling how pit initiation behaves with respect to time.

It should be pointed out that, since this model performs calculations for only two points (anode and cathode) on a metal surface, it is not intended to simulate the random behavior related to the location of pit initiation.

A two-parameter Weibull distribution function is defined as:

$$We(x) = \frac{\beta}{\alpha} \left(\frac{x}{\alpha} \right)^{\beta-1} e^{-\left(\frac{x}{\alpha} \right)^{\beta}} \quad (112)$$

Where We is the Weibull function, x is the independent variable, α is the scale parameter, β is the shape parameter.

The scale and shape parameters are related to mean and standard deviation of the distribution in the following ways:

$$\mu = \alpha \Gamma \left(1 + \frac{1}{\beta} \right) \quad (113)$$

$$\sigma^2 = \alpha^2 \left[\Gamma\left(1 + \frac{2}{\beta}\right) - \Gamma^2\left(1 + \frac{1}{\beta}\right) \right] \quad (114)$$

Where μ is the mean value, σ is the standard deviation, Γ is the gamma function, which is defined as:

$$\Gamma(z + 1) = \int_0^{\infty} t^z e^{-t} dt \quad (115)$$

Scale parameter and shape parameter can be obtained by solving Equations (113) and (114) based on the values of mean and standard deviation. Once scale and shape parameters are obtained, a Weibull distribution random number can be generated based on a uniform distribution random number,¹²⁷ which is normally given as a built-in function in most software packages, as shown in Equation (116):

$$y = \alpha \cdot [-\ln(1 - x)]^{\frac{1}{\beta}} \quad (116)$$

Where y is the Weibull distribution random number and x is the uniform distribution random number between 0 and 1.

Currently, a mean value of 2 hours after pseudo-passivation and a standard deviation of 0.5 hours are used to generate the time for pit initiation. These values are arbitrarily set and can easily be changed according to experimental findings.

4.4.7 Pit propagation

Pit propagation is driven by the potential difference between anode and cathode. The pit propagation rate is governed by the metal potential at the steel surface. Due to the galvanic effect, the metal potential can accelerate the corrosion rate on the anode and decelerate that on the cathode. Due to the separation of anode and cathode, the solution

resistance between anode and cathode also plays an important role in the pit propagation stage.

The potentials on the metal surface and in the liquid layer above the metal can be obtained by solving the Laplace equation governing potential distribution in a conductive medium:

$$\nabla \cdot (\kappa_{eff} \nabla \phi) = 0 \quad (117)$$

Where κ_{eff} is the effective conductivity of the electrolyte account for the presence of non-conductive FeCO_3 layer, which is given by Bruggeman's equation as:⁹¹

$$\kappa_{eff} = \kappa_0 \varepsilon^{1.5} \quad (118)$$

Where ε is the porosity of FeCO_3 layer and κ_0 is the conductivity of electrolyte without FeCO_3 layer, which can be calculated as:¹⁰⁸

$$\kappa_0 = F^2 \sum_j z_j^2 u_j c_j \quad (119)$$

Where F is Faraday constant, z_j is the ionic charge, u_j is the mobility and c_j is the concentration.

Considering:

$$i = -\kappa_{eff} \nabla \phi \quad (120)$$

Equation (117) suggests:

$$\nabla \cdot i = 0 \quad (121)$$

Equation (121) indicates that there is no net current change in the solution and that the solution always maintains electro-neutrality.

It should be noted that the accurate form of the governing equation for electrostatic potential distribution is given by Poisson's equation:¹⁰⁸

$$\nabla^2\phi = -\frac{F}{\xi} \sum_j z_j c_j \quad (122)$$

where ξ is the permittivity of the electrolyte. This equation implies that potential distribution is related to the charge separation of species in the solution. However, it has been argued that in an electrochemical system, potential distribution occurs on a much shorter time scale than mass transfer. Heppner⁸⁰ estimated that the time required to electrically neutralize an electrolyte is 10^{-8} seconds. For water system, the quotient of F/ξ is very large, which physically indicates that any small separation of charge would generate a significant potential gradient which tends to rapidly restore the system to the state of electro-neutrality. The strong force resulting from a large electrostatic potential gradient can eliminate any charge imbalance at a speed much faster than that of mass transport. Therefore, it is common practice to assume that electroneutrality is preserved at any point of time. Mathematically, this means that Equation (122) can be safely replaced with Equation (117) without introducing major errors.

Unlike in a mass transport process where a 1D domain is acceptable, a significant potential gradient can be present both in directions perpendicular and parallel to the metal surface. Therefore, it is essential to calculate the potential distribution in a 2D domain as shown in Figure 21; the height of which is equal to the thickness of the liquid layer.

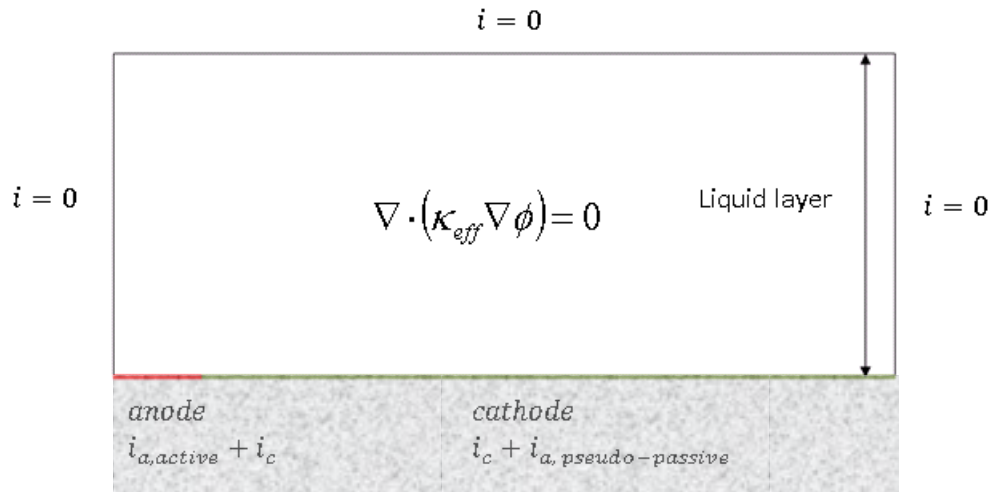


Figure 21. Computation domain and governing equation with boundary conditions for electrostatic potential distribution in aqueous solution.

The boundary condition on the steel surface is given by Kirchhoff's law:

$$\sum i_j = -\kappa \nabla \phi \quad (123)$$

Where i_j is the current density of individual electrochemical reactions on the metal surface, which can be calculated by the equations presented in Table 2.

For other boundaries (the left, right and upper walls of the computation domain), normal current density is set to zero. The right wall is far away from the metal surface and charged species would therefore not be able to reach the boundary; the upper wall defines the location where liquid phase (and therefore charged species) ends; the left boundary maintains zero current density due to symmetrical configuration.

It is worth mentioning that although Equation (117) applies to both uniform and localized corrosion, it is not solved for uniform corrosion in the model. This is because the potential is uniformly distributed on the steel surface due to the close proximity of

anode and cathode in a uniform corrosion cell. This uniform potential can be readily obtained based on the charge balance of anodic and cathodic reactions, as shown in Equation (124):

$$\sum_{anodic} i = \sum_{cathodic} i \quad (124)$$

where i is current density of anodic or cathodic reactions.

With the knowledge of metal potential, the anodic dissolution rate can be calculated using the iron oxidation reaction shown in Table 2.

For localized corrosion cases, potential is calculated on multiple points along the anode and cathode surfaces. In order to couple the 2D simulation of potential distribution with the 1D simulation of mass transport, the average current density on the anode or cathode surface is calculated to provide the boundary conditions for mass transport Equation (86). This is done by replacing Equation (94) with:

$$N_j = \frac{\sum i_{ij} \cdot A_i}{A \cdot z_j F} \quad (125)$$

where i_{ij} is the current density related to the j^{th} species at the i^{th} location, A_i is the steel surface area at the i^{th} location and A is the total area of anode or cathode.

4.5 Numerical technique

The governing equations for mass transport and FeCO_3 layer growth are solved in two 1D domains as sketched in Figure 17 and Figure 20. It should be noted that one mass transport equation is needed for each species in solution. To simulate a real system, multiple mass transport equations are coupled and solved simultaneously. Simulating a

CO₂ aqueous system typically requires solving 10 equations or more. The governing equations are discretized using the control volume method in the predefined 1D domain with a non-uniform grid as sketched in Figure 22. Denser control volumes are placed near the steel surface where the highest fluxes are expected; as the grid approaches the bulk, less control volumes are used. With the control volume method described by Patankar,¹¹¹ the governing partial differential equations are converted into a series of algebraic equations in each control volume. Equations (86) and (95) can be respectively discretized as:

$$\varepsilon_P (c_{j,P} - c_{j,P}^o) \frac{\Delta x_P}{\Delta t} = -\kappa_{P+1/2} N_{j,P+1/2} + \kappa_{P-1/2} N_{j,P-1/2} + \varepsilon_P R_{j,P} \Delta x_P \quad (126)$$

$$(\varepsilon_P - \varepsilon_P^o) \frac{\Delta x_P}{\Delta t} = -\frac{M_{FeCO_3}}{\rho_{FeCO_3}} R_{FeCO_3} \Delta x_P - CR(\varepsilon_{P+1/2} - \varepsilon_{P-1/2}) \quad (127)$$

where subscripts P , $P-1/2$ and $P+1/2$ represent the control volume P and its adjacent upstream and downstream interfaces respectively as illustrated in Figure 22. Superscript “o” signifies the known variables from the previous time step and the variables without “o” refer to the present time, which are unknowns and are to be solved for.

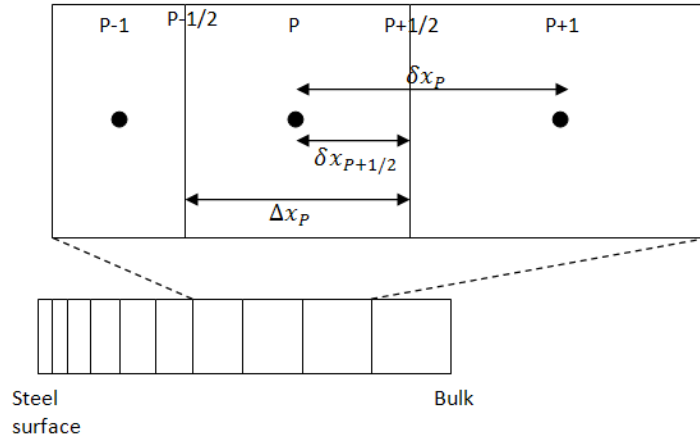


Figure 22. Schematic of control volumes used for discretizing the governing equations for mass transport and FeCO_3 layer growth.¹³

The interfacial parameters in Equation (126) are obtained by the harmonic mean interpolation method.¹¹¹ For instance, the interfacial diffusion coefficient ($D_{j,P+1/2}$) embedded in $N_{j,P+1/2}$ is evaluated by:

$$D_{j,P+1/2} = \left(\frac{1 - f_{P+1/2}}{D_{j,P}} + \frac{f_{P+1/2}}{D_{j,P+1}} \right)^{-1} \quad (128)$$

where $f_{P+1/2}$ is a factor related to the distance from the center of the control volume to the adjacent interface, which is calculated as:

$$f_{P+1/2} = \frac{\delta x_{P+1/2}}{\delta x_P} \quad (129)$$

The interfacial parameter in Equation (127) is evaluated using the second-order Koren scheme^{115,116} due to its association with convective-like terms. For example, $\varepsilon_{P+1/2}$ is evaluated as:

$$\varepsilon_{P+1/2} = \varepsilon_P + \frac{\Delta x_P}{2} \Psi(r_P) \left(\frac{\partial \varepsilon}{\partial x} \right)_{P-1/2} \quad (130)$$

where $\Psi(r_P)$ is the flux-limiting function given by:

$$\Psi(r_P) = \text{Max} \left(0, \text{Min} \left(2r_P, \left(\frac{1}{3} + \frac{2}{3} r_P \right), 2 \right) \right) \quad (131)$$

and r_P can be calculated as:

$$r_P = \frac{\varepsilon_{P+1} - \varepsilon_P + 1e - 20}{\varepsilon_P - \varepsilon_{P-1} + 1e - 20} \quad (132)$$

In Equations (126) and (127), a fully-implicit time discretization scheme is implemented; the parameters in the center of a control volume ($c_{j,P}$ and ε_P) are evaluated by its neighboring parameters at the current time step - implicitly. This is different from the explicit time discretization scheme in which parameters in a control volume are functions of its neighboring parameters at past time step. As illustrated by Patankar,¹¹¹ an explicit time scheme is easier to implement, but could suffer from instability; conversely, an implicit time scheme is harder to implement, but numerically more stable.

As mentioned above, the mass transport equation is highly non-linear mainly owing to the existence of chemical reaction rates. Various species are coupled together through the chemical reaction term in a non-linear fashion, as shown in section 4.4.1. The non-linearity is further aggravated by the implementation of implicit boundary conditions on the steel surface. As shown in Equation (94), fluxes of electroactive species are given by current densities on steel surface, which are correlated with corresponding species concentrations in a non-linear fashion. All the nonlinear terms in the governing

equation(s) are linearized using Taylor series expansion, keeping only the constant and the linear term. As an example, the chemical reaction term can be linearized as:

$$R_{j,P} = R_{j,P}^o + \sum_j \left(\frac{\partial R_{j,P}}{\partial c_{j,P}} \right)^o (c_{j,P} - c_{j,P}^o) \quad (133)$$

Where $\left(\frac{\partial R_{j,P}}{\partial c_{j,P}} \right)^o$ is the derivative of chemical reaction rate with respect to involved species concentrations, which is evaluated at the concentrations obtained at the previous time step.

The discretized first-order algebraic equations are assembled into a matrix in the form of $AX=B$ and solved simultaneously to obtain the concentrations and porosity of FeCO_3 in all control volumes. In this model, an LU method is implemented to solve the matrix.

The governing equation for potential distribution (Equation (117)) is solved in a 2D domain as shown in Figure 21. A line-by-line method is implemented to solve the equation.¹¹¹ In this method, the governing equation is discretized in the same way as presented above:

$$\begin{aligned} \frac{\Delta x_P}{\Delta y_n} \kappa_n \phi_N + \frac{\Delta x_P}{\Delta y_s} \kappa_s \phi_S - \left(\frac{\Delta x_P}{\Delta y_n} \kappa_n + \frac{\Delta x_P}{\Delta y_s} \kappa_s + \frac{\Delta y_P}{\Delta x_e} \kappa_e + \frac{\Delta y_P}{\Delta x_w} \kappa_w \right) \phi_P \\ = - \frac{\Delta y_P}{\Delta x_e} \kappa_e \phi_E - \frac{\Delta y_P}{\Delta x_w} \kappa_w \phi_W \end{aligned}$$

where upper case subscripts (E , W , N , S , and P) refer to the center of control volume and lower case subscripts (e , w , n and s) represent the interfaces. Δx and Δy are the size of the control volumes in the E - W and N - S directions, respectively. The notations are schematically illustrated in Figure 23.

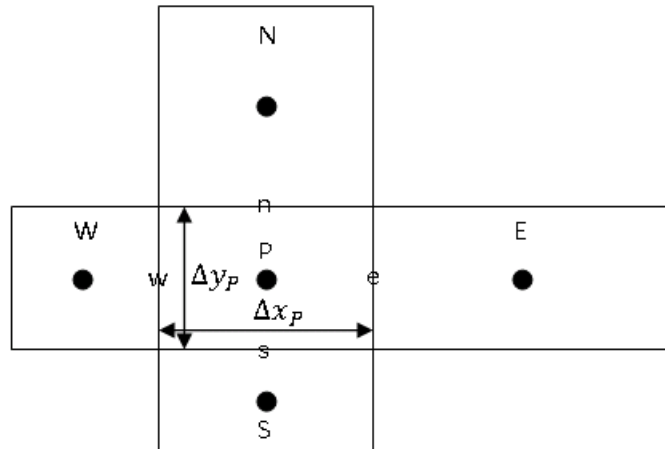


Figure 23. Schematic of the 2-D control volumes used for discretizing governing equations for potential distribution.

By using the values obtained in the previous iteration for the neighboring parameters in one direction, e.g. east-west, Equation (134) can be solved for the other direction (i.e. north-south) as if it were a 1D simulation. This procedure is performed line-by-line by sweeping in a given direction, and iterates until the following criterion is satisfied:

$$\sqrt{\frac{\sum_i \sum_j (\Phi_{ij} - \Phi_{o,ij})^2}{N_i \cdot N_j}} < 0.001 \quad (135)$$

$$\frac{\sum_i \sum_j \Phi_{ij}}{N_i \cdot N_j}$$

Where Φ and Φ_o are potentials at current and previous time step respectively, N is the total number of control volumes in a specific direction, subscripts i, j refer to the nodes in N - S and E - W directions, respectively.

4.6 Solving strategy

Figure 24 shows the calculation flow chart used in this model. The program starts with the calculation of metal potential under initial conditions (temperature, pressure, water chemistry, water velocity, etc.). This is followed by solving mass transport equations for various species and FeCO_3 layer growth equations in the predefined 1D domains for anode and cathode sequentially. In solving mass transport equations, the metal potential is used to generate fluxes of species, which are used to define the boundary conditions for the governing equations. The Laplace equation for potential is then solved in a predefined 2D domain in order to obtain the potential distribution. The updated potentials allow for the calculation of anodic and cathodic reaction rates, which can be used to generate the corrosion rate. The calculation then advances in time and starts another cycle of calculations. Throughout the calculation, steel surface pH and potential are constantly monitored. When surface conditions are such that pseudo-passivation is favored, the electrochemical reaction kinetics for pseudo-passive surface will be used to calculate the current densities. Once pseudo-passivity is achieved, the Weibull distribution random function is activated, which will at some point in time activate removal of the protective layer on the anode and initiate the pit. Upon pit initiation, electrochemical reaction kinetics on the anode are switched to those for active surface, while pseudo-passivity is maintained on the cathode.

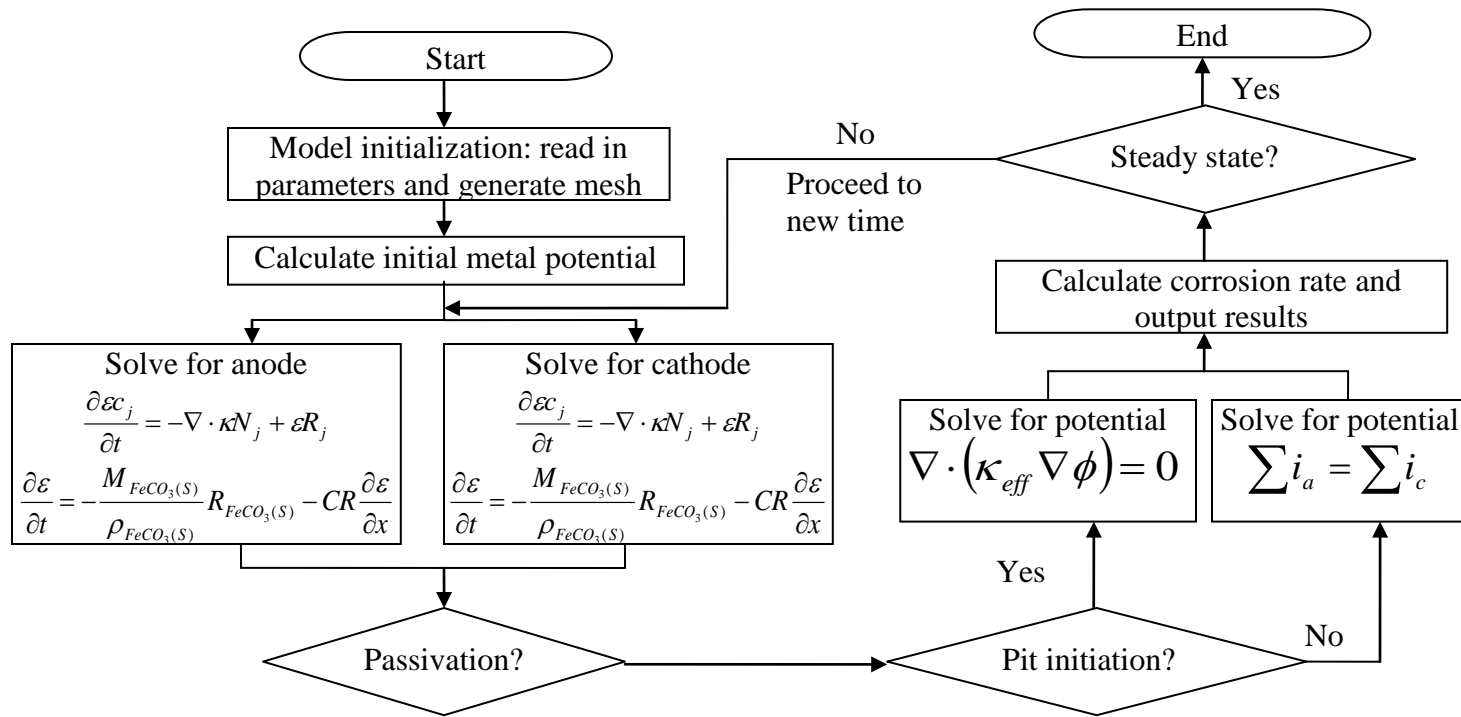


Figure 24. Flow chart used in the localized corrosion model.

4.7 Model verification and parametric study

Although the present model targets CO₂ localized corrosion, it has the capability of predicting uniform corrosion as well, as all the phenomena involved in the uniform corrosion process (i.e. mass transfer, chemical reactions, electrochemical reactions and FeCO₃ layer growth) are present in localized corrosion. Based on the previously-built uniform corrosion model (MULTICORP V4), a completely new version of the corrosion prediction software package was developed (MULTICORP V5) based on the present work with entirely new source codes designed to simulate uniform corrosion as well as CO₂ localized corrosion. A number of improvements, both in the physico-chemical and numerical models were made for uniform corrosion simulation. New physics governing CO₂ localized corrosion was incorporated. The major improvement is in the description of electrochemical reaction kinetics, which is now done through the use of the Butler-Volmer equation with true exchange current density and reversible potential. This change results in a more reasonable potential distribution in a galvanic cell, which is critical in calculating galvanic current density. In terms of numerical changes, the main improvement was in the use of an implicit time marching scheme in solving the governing equation for FeCO₃ layer growth (Equation (95)). This improvement enhances the stability of the model, which would accommodate a bigger time step in the calculation leading to less simulation time. Due to the rebuilding of the entire source code, the new model needed to be recalibrated against with a large number of experimental data points for uniform corrosion and with what limited data exist for localized corrosion (all contained in the experimental database at ICMT). Overall the

verification showed good agreement. A few comparisons are illustrated in the section below to facilitate further discussion of the model's performance.

4.7.1 Uniform corrosion verification

4.7.1.1 Film free condition

Figure 25 shows the comparisons between the model and experiments for two important factors, pH and velocity. Good agreement is evident under all conditions. This is not surprising considering the fact that CO₂ uniform corrosion is relatively well-understood and mechanistically implemented in this model. It can be seen that corrosion rate increases with increasing velocity and reaches a maximum value at a certain velocity, which becomes flow-independent at still higher flow rates. This is an indication that the corrosion process switches from mass transfer limiting to charge transfer limiting. The model also suggests that corrosion becomes progressively less flow-independent as pH increases. This is because, at a higher pH, corrosion is predominantly contributed by H₂CO₃ reduction, a reaction controlled by CO₂ hydration rate rather than by mass transfer.

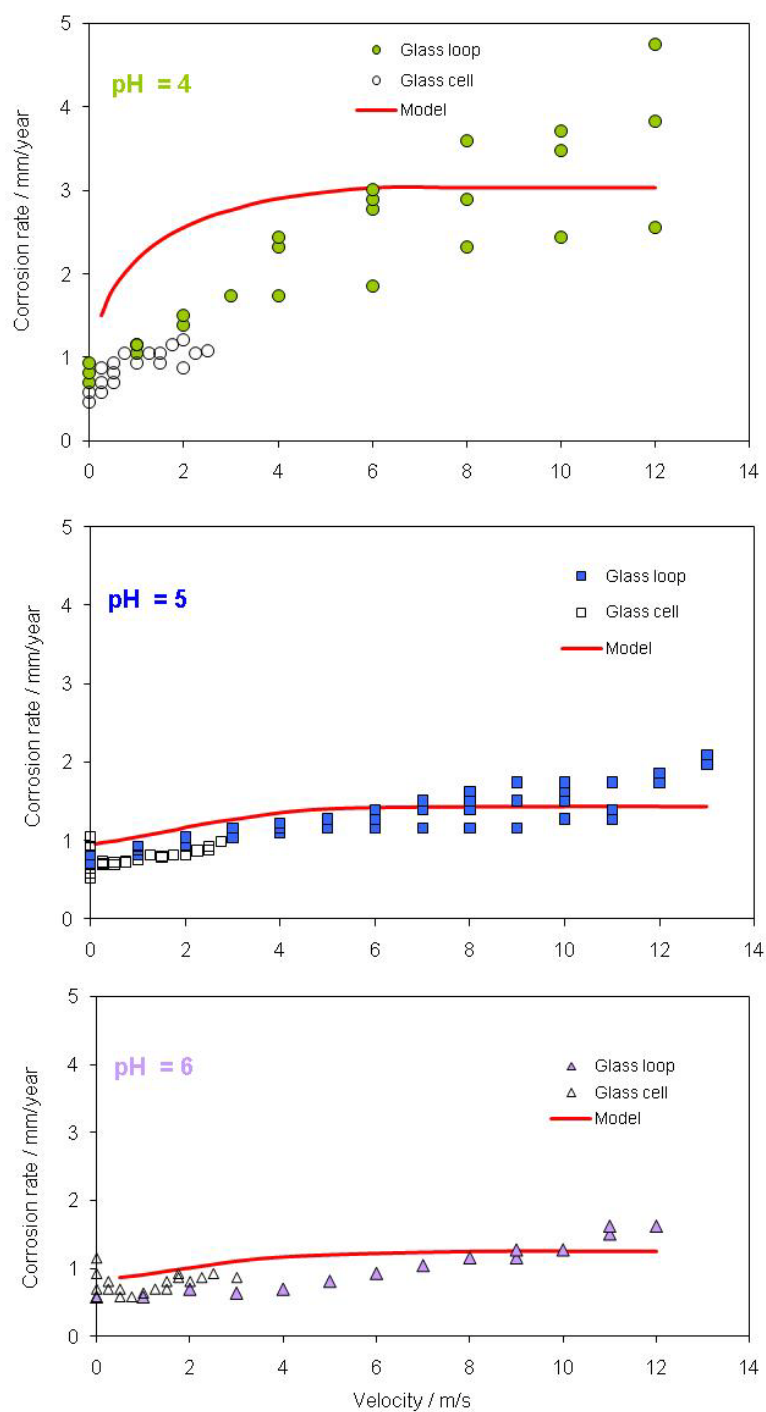


Figure 25. Comparisons between model and experiments for 1 bar CO₂, 20°C and various pHs and velocities.

4.7.1.2 FeCO_3 layer forming condition

Stagnant condition

Figure 26 compares the model and experiment for FeCO_3 layer forming conditions in a stagnant solution. Bulk supersaturation with respect to FeCO_3 is around 37. The high supersaturation combined with high temperature leads to fast precipitation of FeCO_3 , which causes a decrease in the corrosion rate. The measured corrosion rate vs. time trend is well-captured by the model. The sharp decrease at the beginning of the simulation is due to the initially high corrosion rate, which generates a large amount of Fe^{2+} that does not readily move away from the metal surface in a stagnant solution.

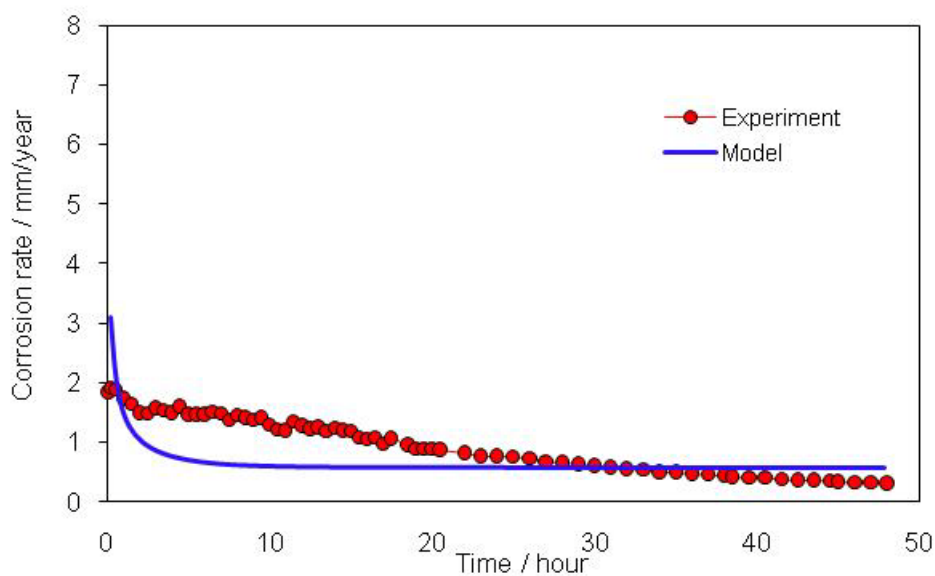


Figure 26. Comparison between model and experiments for FeCO_3 layer forming condition at temperature 80°C , 0.53bar CO_2 , $\text{pH } 6.3$ and bulk Fe^{2+} concentration 50ppm , stagnant.

Flowing conditions

Figure 27 compares the model prediction with a set of experiments conducted in a glass cell with flowing conditions. Clearly, predictions fall among the variations of experimental data, revealing the capability of the model in simulating FeCO_3 growth kinetics and their effect on the corrosion process.

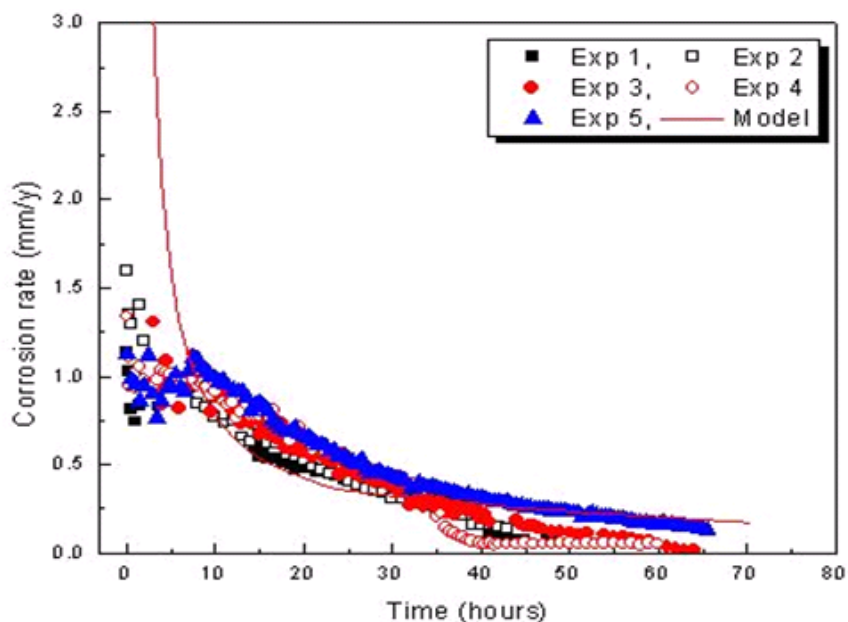


Figure 27. Comparisons between the model and the experiments for flowing FeCO_3 layer-forming condition at temperature 80°C , pH 6.6, 0.53bar CO_2 , 10ppm bulk Fe^{2+} and 1000rpm rotation speed.

4.7.2 Localized corrosion verification

Limited experimental data is available in the open literature for localized corrosion rates of carbon steel corroding in CO_2 solutions. More importantly, it is not uncommon for information to be missing in open literature, and for simulation purposes

some assumptions have to be made. To raise the confidence level, the measurements conducted at ICMT are adopted as the data source for model calibration. The data were obtained in a series of artificial pit experiments conducted by Han *et al.*¹⁰⁵ In these experiments, a large ring-shaped electrode is pre-corroded in a solution with high pH and temperature to allow the formation of dense FeCO_3 layer and spontaneous pseudo-passivation on the electrode surface. Once a stable FeCO_3 layer is obtained, the electrode is transferred into the solution of interest, and a small electrode with a freshly polished active surface is then inserted into the hole at the center of the large electrode, forming a galvanic cell with electric connection between two electrodes. The galvanic current is then measured as a function of time. The test equipment is schematically shown in Figure 28. The detailed test conditions and procedures can be found in the original paper.¹⁰⁵ It should be stressed that these experiments recorded only the galvanic current. This should not be confused with the anodic current density which is directly related to the localized corrosion rate. The galvanic currents in the experiments are defined as the difference between total anodic and cathodic current at the metal potential. From Figure 29 it is apparent that the galvanic current (represented by I_{galvanic}) is smaller than the anodic current (symbolized as $I_{\text{corr}}^{\text{couple}}$). Since the potential is non-uniformly distributed along the metal surface, the model takes the average galvanic current density over the anode surface to be used for comparison. Figure 30 shows an example of comparison between anodic current density and galvanic current density. Anodic current density is evidently higher than galvanic current density throughout the simulation.

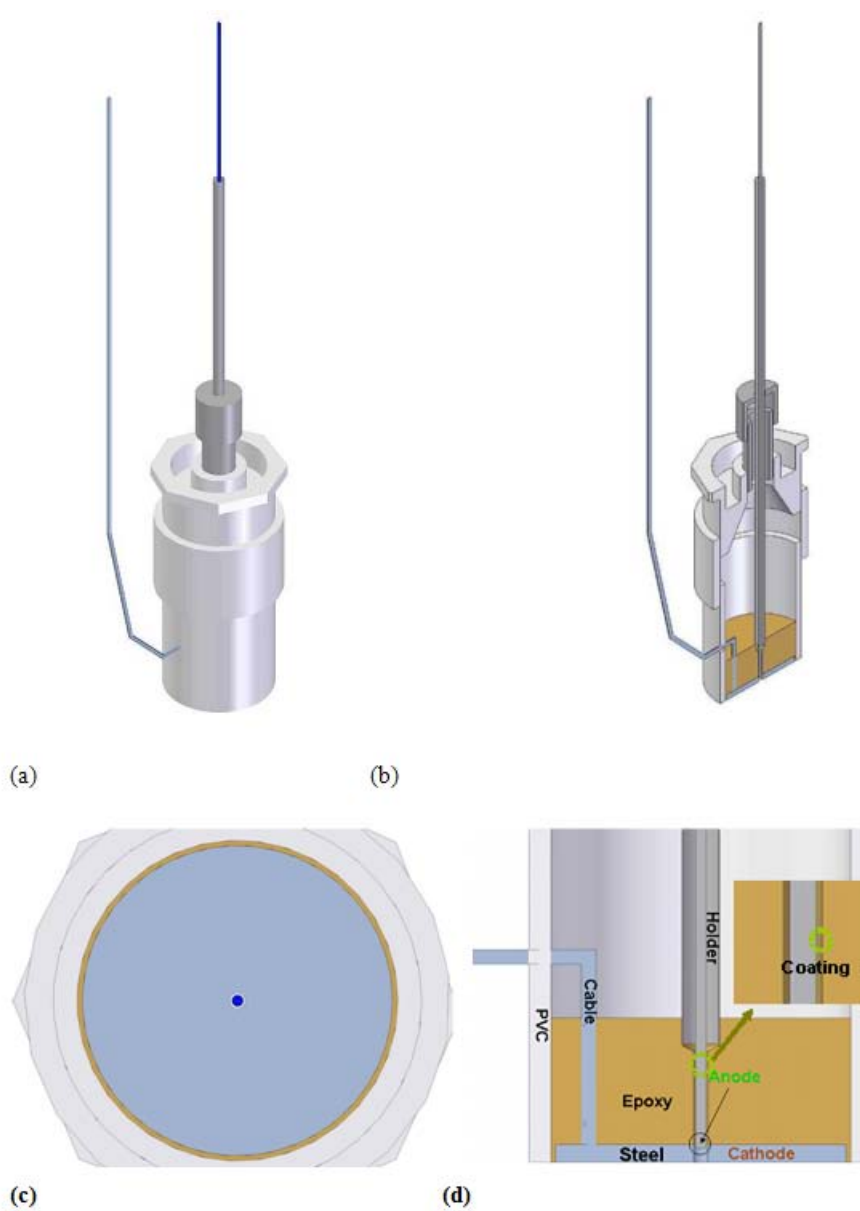


Figure 28. Schematic illustration of the artificial pit unit used in Han *et al.* experiments (a) fully assembled artificial pit, (b) cutaway side view, (c) enlarged bottom view of cathode; center hole for anode, (d) detailed cross section view.¹⁰⁵

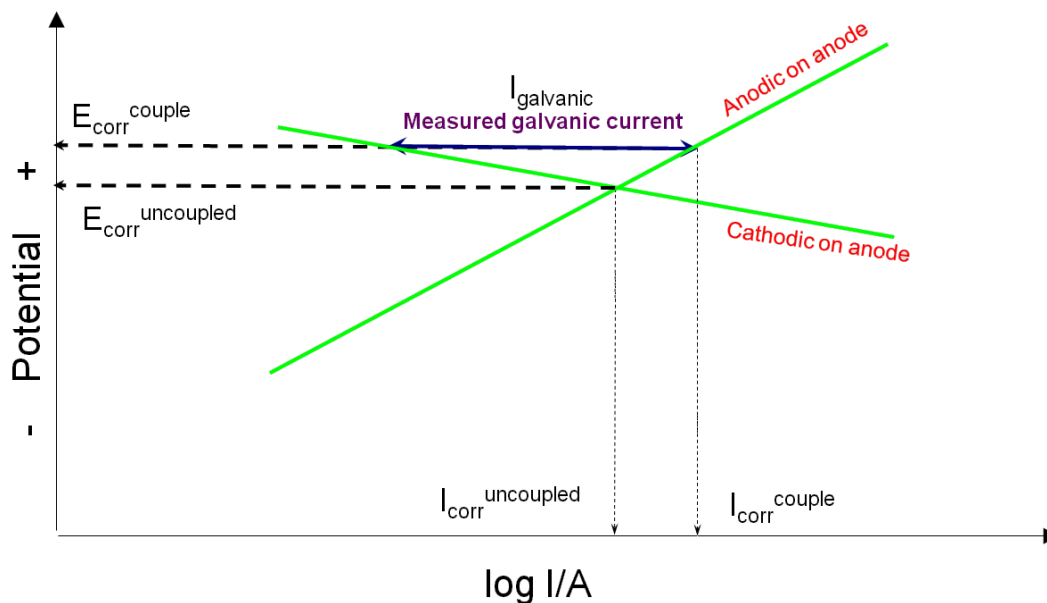


Figure 29. Evans diagram depicting relationship of galvanic current and anodic current. Galvanic current is represented by I_{galvanic} and anodic current is symbolized by $I_{\text{corr}}^{\text{couple}}$.

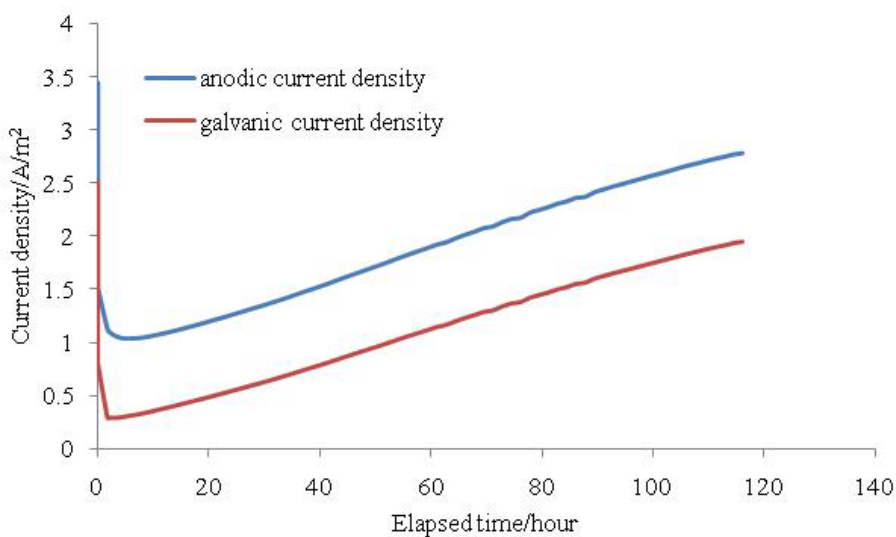


Figure 30. Comparison of anodic current density and galvanic current density. Simulation conditions: Supersaturation of FeCO_3 0.3–0.9, T 80 °C, CO_2 0.53bar, pH 5.9–6.1, 1wt % NaCl, stagnant.

4.7.2.1 Stagnant condition

Figure 31 shows the measured and predicted galvanic current density in a stagnant solution. Both model and experiments suggest pit propagation under these conditions where supersaturation is around 1 (the condition known as the “grey zone”¹). The galvanic current density starts off at a high value and quickly drops within short period of time. It then slowly creeps up and reaches around 1A/m^2 at the end of the simulation. The sharp drop in galvanic current density at the beginning is due to the establishment of mass transfer limitation which is induced by the high galvanic current density at the moment of galvanic coupling. In a stagnant solution, the corrosion product (Fe^{2+}) generated from the corrosion process tends to stay at the metal surface, leading to a large increase in supersaturation and resulting in fast precipitation on the metal surface. In such a process, CO_3^{2-} is continuously consumed by the precipitation process. In the mean time, supplemental CO_3^{2-} from the bulk solution is compromised by the large mass transfer resistance due to the absence of convective flow. Therefore, substantial reduction of CO_3^{2-} concentration is experienced near the steel surface, which drives Reaction (30) to give up more H^+ in the solution adjacent to the anode surface. The increased solution acidity raises the potential of the anode and leads to increased anode current density as the corrosion process evolves. It can be expected that, as the precipitation process continuously draws CO_3^{2-} out of the solution, a shortage of CO_3^{2-} will eventually be experienced particularly in the vicinity of the metal surface, which will decrease the supersaturation of FeCO_3 . Excessive Fe^{2+} on the steel surface will then start raising the surface pH to maintain charge balance in the solution. The competing effect of

precipitation and charge balance will eventually reach the balance where pit propagation can continue at a relatively stable rate. Figure 32 shows the history of a predicted surface pH and potential at an anode to support the above arguments.

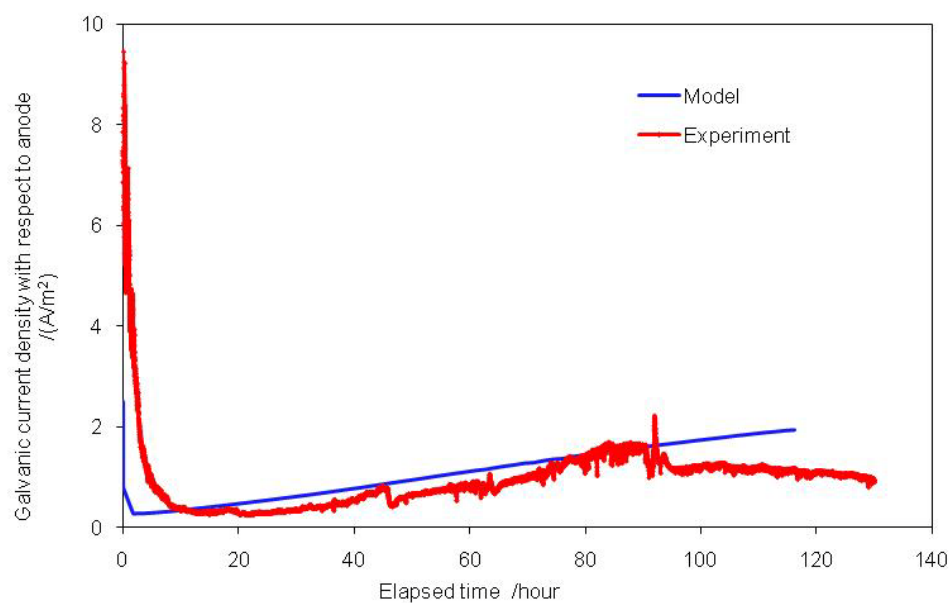


Figure 31. Comparison of galvanic current density between model and experiments for the conditions: Supersaturation of FeCO_3 0.3–0.9, Temperature 80 °C, CO_2 0.53bar, pH 5.9–6.1, 1wt % NaCl, stagnant.

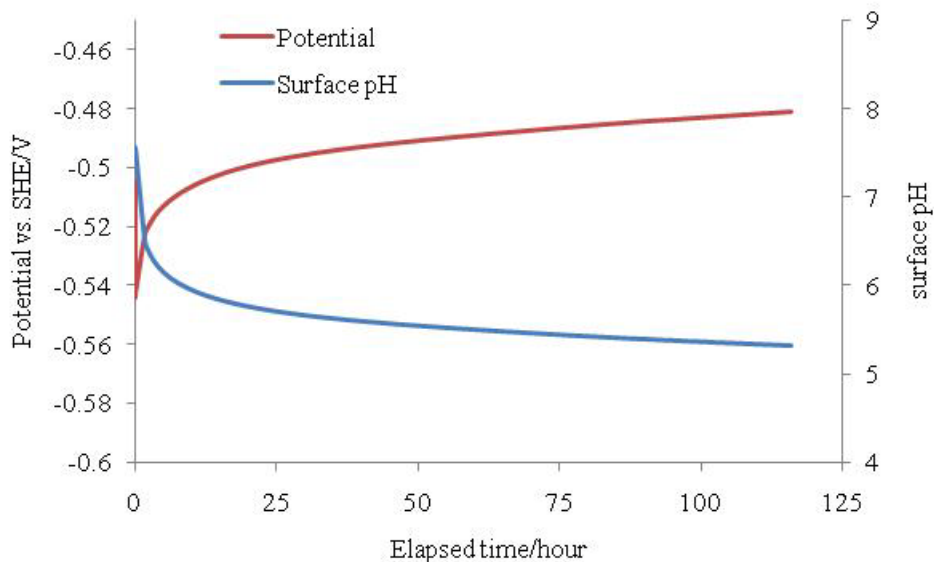


Figure 32. Surface pH and potential as a function of time. Simulation conditions: Supersaturation of FeCO_3 0.3–0.9, T 80 °C, CO_2 0.53bar, pH 5.9-6.1, 1wt % NaCl, stagnant.

Figure 33 illustrates a case of pit death at FeCO_3 supersaturation above 1. Mimicking the trend exhibited in the measurement, the model predicts a progressively-decreasing galvanic current density which eventually diminishes after about 40 hours. The decreasing galvanic current density is due to the formation of FeCO_3 layer on the anode surface as a result of FeCO_3 supersaturation above 1. The FeCO_3 layer formation is greatly enhanced by the slow mass transfer of Fe^{2+} in the stagnant solution. Still, it is striking that a medium level of supersaturation in this case would cause such a rapid decrease of galvanic current. This case further justifies the “grey zone” theory, which suggests that a pit propagates when supersaturation of FeCO_3 is around unity.

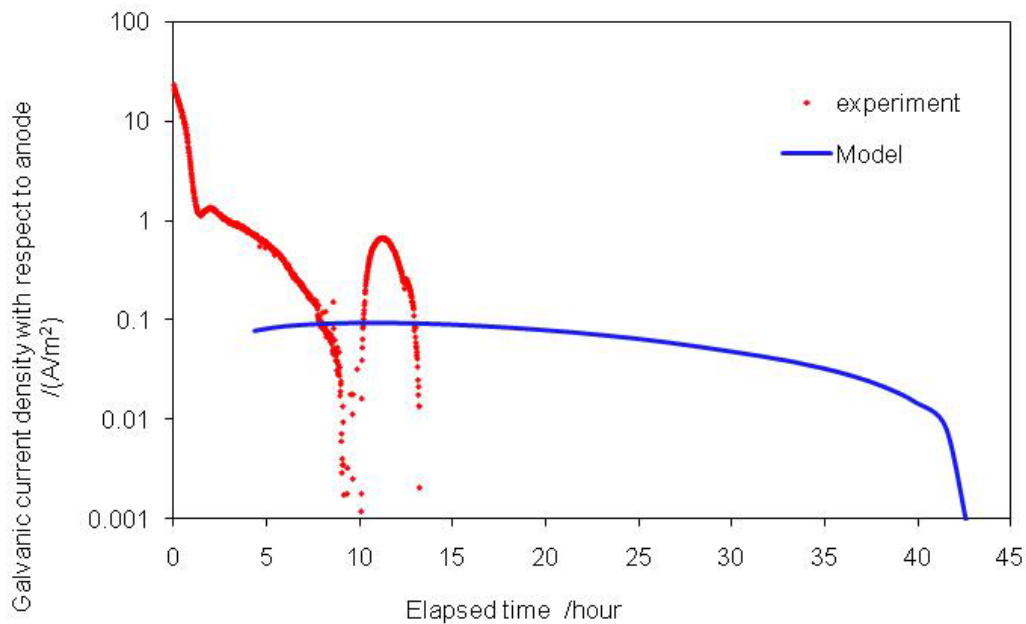


Figure 33. Comparison between the model and the experiment for the conditions: Supersaturation of FeCO_3 3–9, T 80 °C, $p\text{CO}_2$ 0.53bar, pH 5.6, $[\text{NaCl}] = 1\text{wt}\%$, stagnant.

4.7.2.2 Flowing condition

Figure 34 illustrates the measured and simulated galvanic current densities in a flowing solution. It is notable that pit propagation prevails in this case with the supersaturation value within the “grey zone”. The galvanic current density initializes at a high value and quickly drops to about 4A/m^2 due to mass transfer limitation. The galvanic current density is then stabilized at that level in the rest of the simulation. It worth mentioning that under flowing conditions, the galvanic current density does not increase with time as galvanic corrosion proceeds. This is because the flow greatly enhances the mass transfer and carries away the corrosion product (Fe^{2+}) on the metal

surface, which prevents the large consumption of CO_3^{2-} and resulting acidity in the near-metal solution. Conversely, the model predicts a slightly higher surface pH compared to the bulk value (pH 5.9) due to existence of excessive Fe^{2+} on the metal surface, as shown in *Figure 35*. The surface pH variation is consistent with the trend of galvanic current, which reflects the amounts of Fe^{2+} produced in the corrosion process.

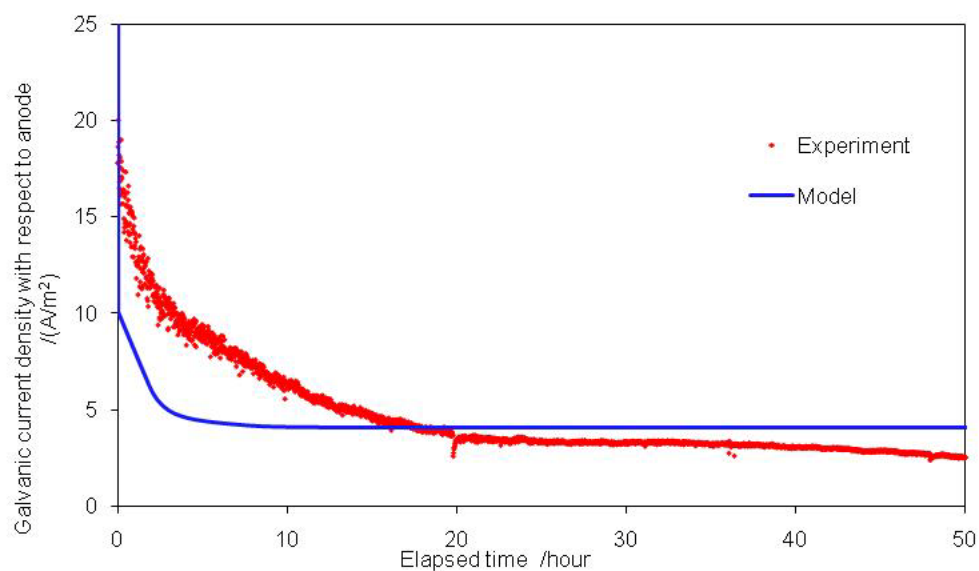


Figure 34. Comparison between model and experiments for the conditions: Supersaturation of FeCO_3 0.8–4, T 80 °C, CO_2 0.53bar, pH 5.9, 1wt % NaCl, 500rpm.

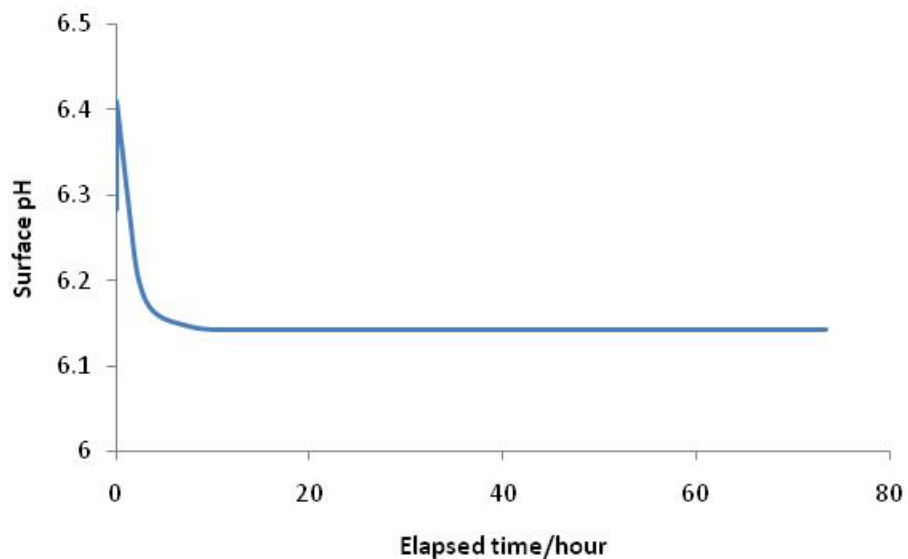


Figure 35. Anode surface pH vs. time for the condition: Supersaturation of FeCO_3 0.8–4, T 80 °C, CO_2 0.53bar, pH 5.9, 1wt % NaCl, 500rpm.

4.7.3 Parametric study

4.7.3.1 Effect of supersaturation of FeCO_3

It has been repeatedly observed in the experiments that supersaturation is a key indicator for pit propagation potential. The so-called “grey zone” theory suggests that a pit can propagate in a CO_2 environment around FeCO_3 saturation point, i.e. when under/super-saturation is in the range of 0.5-2.¹ Although no strict criterion has been imposed in the model, *Figure 31* and *Figure 33* clearly shows that the model is able to properly capture the concept of the “grey zone” and predict reasonable corrosion behavior as observed in the experiments. In this subsection, two simulation cases are made to demonstrate the effect of supersaturation on localized corrosion behavior. The

simulation conditions are: temperature 80°C, CO₂ partial pressure 0.52 bar, liquid velocity 0.5 m/s, 0.1 wt% NaCl, bulk pH 6, bulk supersaturation of FeCO₃ 1 and 10 respectively.

Figure 36 compares the corrosion rates for different supersaturation levels. It can be seen that a higher supersaturation evidently shortens the time required for pseudo-passivation, as indicated by the sharp drop in the corrosion rate at about 70 hours for supersaturation of 10. The pseudo-passivation is attributed to FeCO₃ precipitates on the metal surface, which increases the mass transfer resistance to various species moving towards or away from the metal surface. Particularly, this leads to a lower concentration of H⁺ or higher pH on the metal surface. The onset of pseudo-passivation is triggered upon achievement of a critical surface pH where formation of magnetite is favored, as discussed in section 4.4.5. The sudden jump of corrosion rate shortly after pseudo-passivation is due to pit initiation, which is achieved by artificially removing the protective films on the anode surface, including FeCO₃ layer and pseudo-passive film. In this process, the bare active anode surface is exposed to the corrosive solution, leading to a lower potential while the cathode remains pseudo-passivated. A galvanic cell is therefore established between the active anode and the pseudo-passivated cathode, which drives the anode to corrode at a substantially higher rate. It can be seen that the two simulation cases exhibit quite different corrosion behaviors after the pit is initiated. With lower supersaturation, pit is able to propagate in the remainder of simulation time, while pit death is experienced with higher supersaturation irrespective of repeated pit initiation triggered by artificial film removal. The stable pit propagation at supersaturation 1 is due

to the balance between FeCO_3 precipitation rate and corrosion rate, which leaves the anode surface relatively free of film coverage. At an elevated supersaturation, however, FeCO_3 precipitation proceeds faster than corrosion, which builds a more protective FeCO_3 layer on the anode surface leading to a decreasing potential difference between anode and cathode, at some point in time, the potential difference is vanished due to repassivation on the anode surface. The potential differences for two cases are demonstrated in Figure 37.

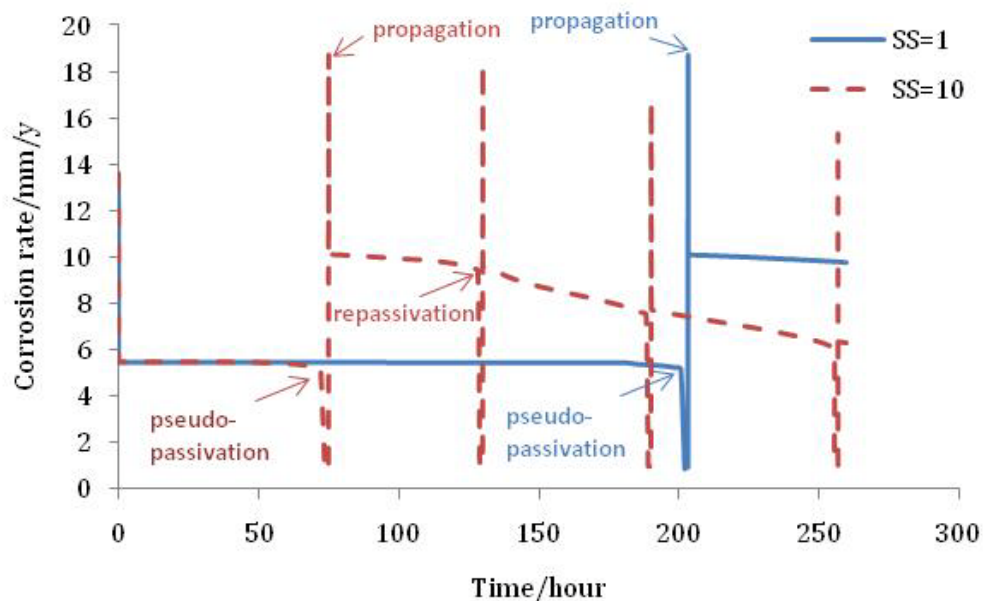


Figure 36. Effect of supersaturation on localized corrosion rate. Simulation conditions: temperature 80°C , CO_2 partial pressure 0.52bar, 0.1 wt% NaCl, velocity 0.2m/s, bulk pH 6.

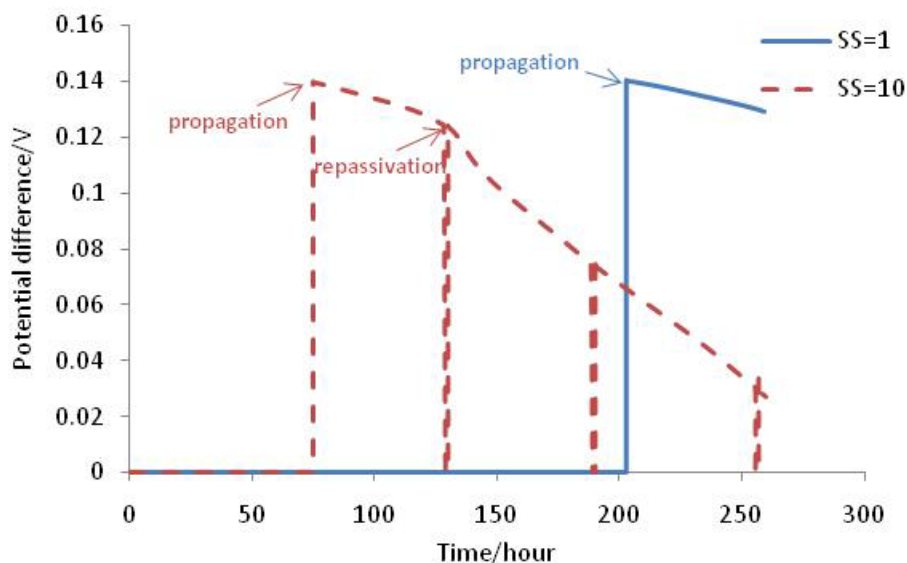


Figure 37. Potential difference between anode and cathode for two simulation cases with supersaturation 1 and 10 respectively. Simulation conditions: temperature 80°C, CO₂ partial pressure 0.52bar, 0.1 wt% NaCl, velocity 0.5m/s, bulk pH 6.

4.7.3.2 Effect of velocity

Velocity is an important factor in a uniform corrosion process by enhancing mass transfer rate of corrosive species. This subsection is intended to demonstrate how velocity can affect localized corrosion process. It should be noted that flow effect on pit initiation is not yet built in the model. Therefore, it is not the intention of this case to discuss the scenario related to flow induced localized corrosion. Rather, the emphasis is placed on flow effect on pit propagation. Figure 38 shows the corrosion rate change for bulk velocity of 0.5m/s and 1m/s. The simulation conditions are: temperature 80°C, CO₂ partial pressure 0.53bar, 0.1 wt% NaCl, bulk pH 6, bulk supersaturation of FeCO₃ 10.

It can be seen that higher velocity largely delays pseudo-passivation. This is due to the enhanced mass transfer rate in a fast-flowing fluid which swiftly carries away Fe²⁺

on the metal surface and effectively reduces the supersaturation of FeCO_3 . As a result, a slower precipitation process is experienced with higher velocity. It can be seen that under higher velocity, the reduced precipitation rate slows down FeCO_3 layer buildup on the anode surface irrespective of high supersaturation of FeCO_3 in the bulk solution. This leads to pit propagation throughout the simulation. On the other hand, in the lower velocity case, pit death is predicted shortly after pit initiation. The pit death at low velocity is due to the accumulation of Fe^{2+} on metal surface leading to increased surface supersaturation and consequent precipitation of FeCO_3 , which overpowers undermining effect. This case clearly demonstrates that, once initiated, a pit tends to propagate in a fast-moving solution but its growth is arrested in a slow-moving solution.

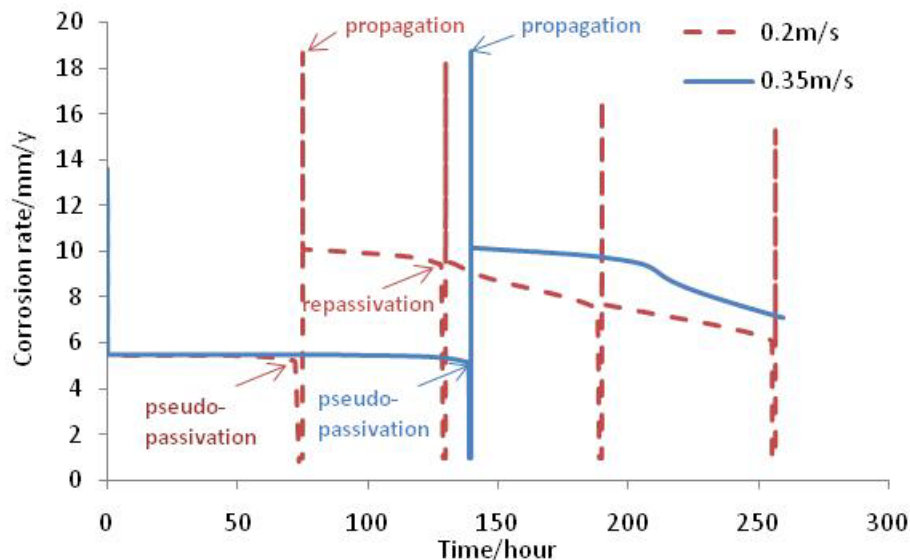


Figure 38. Corrosion rate comparison for bulk liquid velocity at 0.5m/s and 1m/s. Simulation conditions: temperature 80°C, CO₂ partial pressure 0.52bar, 0.1 wt% NaCl, bulk pH 6, bulk supersaturation of FeCO₃ 10.

4.7.3.3 Effect of solution conductivity

Solution conductivity plays a significant role in galvanic corrosion, as it affects potential and current distribution in a galvanic cell. Lower solution conductivity leads to a more non-uniformly distributed potential and smaller current, while higher conductivity results in a more spreading pattern of potential distribution and higher current. Without the consideration of solution conductivity, the localized corrosion rate would be largely overestimated, with the exception of the cases where solution conductivity is very high. In this model, potential distribution is solved with solution conductivity, mass transfer and charge transfer effect coupled together; in other words, tertiary potential distribution can be obtained with the model. Figure 39 compares the galvanic current density of the anode in solutions with different conductivity. Pronounced differences can be seen for

different salt concentrations. It can be seen that progressively smaller current density increase is experienced with increasing salt concentrations. This is because when conductivity becomes high enough, it stops being the limiting factor for the corrosion rate. It can be expected that further increase of conductivity would not lead to significant change of the galvanic current density.

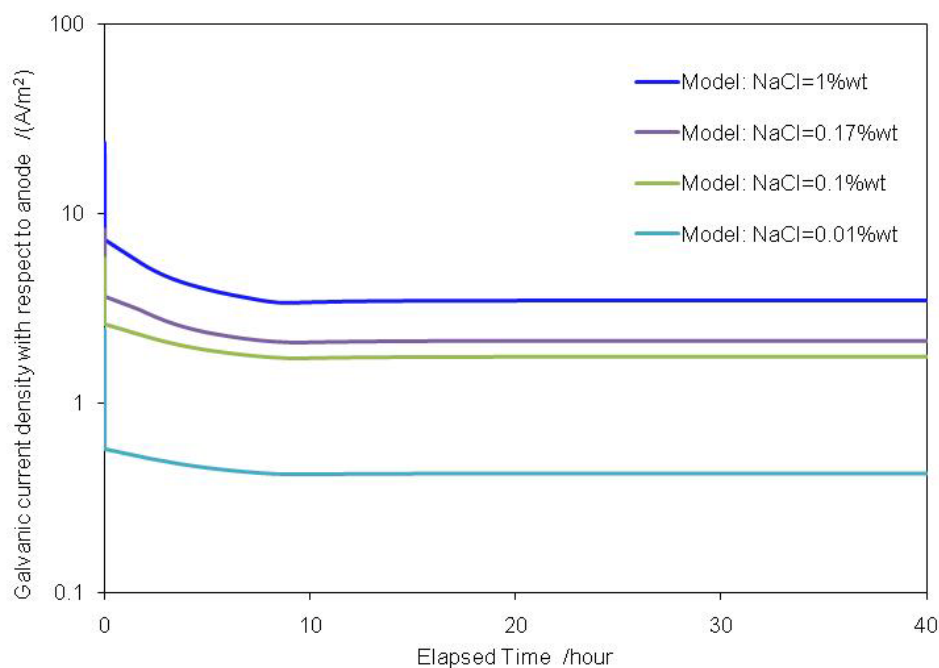


Figure 39. Galvanic current densities for solutions with different conductivity. Simulation conditions: pH 5.9, T 80°C, CO₂ 0.53bar, FeCO₃ supersaturation 2, 0.25m/s.

4.8 Model limitations

This model is built based on a series of fundamental laws allowing the exploration of related process parameters involved in corrosion, such as water chemistry and electrochemistry, in order to elucidate the mechanism(s) governing localized corrosion of

carbon steel in a CO₂ environment. Calculated results have shown good agreement with experimental results. However, like any model, the present model has certain assumptions and limitations that must be appreciated by users in order to achieve confident predictions.

Limitations of the current model are listed below:

- This model is a “2-point model” for mass transport (1D simulation performed for two individual points: anode and cathode) coupled with a 2D model for potential/current distribution. Concentration gradients in the direction parallel to the metal surface are assumed to be unimportant and are neglected.
- An ideal solution is assumed, e.g., concentrations instead of activities are used for calculation, and species independently diffuse in the solution.
- Pit initiation is arbitrarily triggered, as the exact theory is still under development; therefore, kinetics of pit initiation are not properly included.
- As a pit propagates, the anode surface progressively recedes. The moving boundary increases the distance over which diffusion occurs, which enhances the mass transfer resistance. The effect of a moving boundary is neglected in the current model.

5. Conclusions

A transient mechanistic model has been built “from the ground up” to simulate the CO₂ localized corrosion process of carbon steel. The new model (MULTICORP V5¹) is built upon the previously developed uniform corrosion model (MULTICORP V4), in

¹ Since the availability of the source code and the application software based on the present model (MULTICORP V5) is limited to the sponsoring companies, an effort was made to provide the broader corrosion community with a free mechanistic model for internal corrosion prediction of carbon steel pipelines, built around the same theoretical concepts. This was achieved by building FREECORP software with an open source code, which is described in Appendix 6.

which mass transfer, water chemistry, surface electrochemistry, FeCO_3 layer formation are taken into account. New physics governing localized corrosion, such as pseudo-passivation/repassivation, galvanic coupling with solution resistance effect have been added into the model to enable the prediction of both uniform and localized corrosion. Due to the unavailability of a mechanistic pit initiation theory, in this model pits are triggered by artificially removing the protective layer on the anode at a randomly determined point in time.

Apart from water chemistry and uniform/localized corrosion rate, this model is able to predict the time at which pseudo-passivation is invoked based upon thermodynamic equilibrium governing the formation of magnetite. Pseudo-passive current density is mechanistically determined as a function of potential, surface pH and temperature, which change as the corrosion process proceeds. Upon initiation of a pit, the model can predict the evolution of a localized corrosion process and determine whether the pit will propagate or be arrested (die), as physico-chemical conditions at the steel surface evolve over time. Species, potential and current distribution in the computation domain can be extracted from the model at any point in time to facilitate the understanding of the localized corrosion process.

The model has been fully verified with a database containing a large number of measurements for uniform corrosion. Good agreement is extensively obtained between model predictions and measurements.

The model has also been calibrated against limited localized corrosion measurements that were obtained through the measurements of galvanic current in an

artificial pit test unit. Better adjustment of parameters can be anticipated as more reliable test results become available for localized corrosion of carbon steel in the system of interest.

The parametric study shows that pit propagation prevails when supersaturation of FeCO_3 is around unity (i.e. near saturation). At supersaturation well above unity, a pit tends to die due to precipitation of FeCO_3 on the anode. High flow rate tends to maintain pit propagation while low flow rate facilitates pit death. Solution conductivity plays a significant role in determining pit propagation rate. Appreciable increase of localized corrosion rates has been seen with increasing solution conductivity, however this effect diminishes as conductivity approaches a certain high value where solution resistance is no longer a limiting factor.

REFERENCES

1. Y. Sun, "Localized CO₂ Corrosion in Horizontal Wet Gas Flow", PhD. Dissertation, Ohio University, 2003.
2. I. Matsushima, "Carbon steel-Atmopheric Corrosion", Uhlig's Corroison Handbook (John Wiley & Sons, Inc., second edition, 2006).
3. R. Nyborg, "Overview of CO₂ Corrosion Models for Wells and Pipelines", Corrosion/2002, Paper No. 02233 (Houston, TX: NACE, 2002).
4. R.C. Woollam, S. E. Hernandez, "Assessment and Comparison of CO₂ Corrosion Prediction Models", SPE International Oilfield Corrosion Symposium, Paper 100673-MS, 2006.
5. C. de Waard, D. E. Milliams, "Prediction of Carbonic Acid Corrosion in Natural Gas Pipelines", First International Conference on the Internal and External Protection of Pipes, Paper F1 (Cranfield, UK: BHRA Fluid Engineering, 1975).
6. C. de Waard, U. Lotz, D. E. Milliams, "Predictive Model for CO₂ Corrosion Engineering in Wet Natural Gas Pipelines", Corrosion, Vol. 47, No. 12, p. 976, 1991.
7. C. de Waard, U. Lotz, "Prediction of CO₂ Corrosion of Carbon Steel", CORROSION/93, Paper No. 69, (Houston, TX: NACE International, 1993).
8. C. de Waard, U. Lotz, A. Dugstad, "Influence of Liquid Flow Velocity on CO₂ Corrosion: A Semi-Empirical Model", CORROSION/95, Paper No. 128, (Houston, TX: NACE International, 1995).
9. A. M. K. Halvorsen, T. Søntvedt, "CO₂ Corrosion Model for Carbon Steel Including a Wall Shear Stress Model for Multiphase Flow and Limits for Production Rate to Avoid Mesa Attack", CORROSION/99, Paper No. 42, (Houston, TX: NACE International, 1999).
10. NORSOK standard No. M-506, "CO₂ Corrosion Rate Calculation Model", <http://www.nts.no/norsok>, (Oslo: Norwegian Technology Standards Institution, 1998).
11. J. Han, Y. Yang, B. Brown, S. Nešić, "Roles of Passivation and Galvanic Effects in Localized CO₂ Corrosion of Mild Steel", CORROSION/2008, Paper no. 332 (Houston, TX: NACE, 2008).

12. J. Han, D. Young, H. Colijn, A. Tripathi and S. Nešić, "Chemistry and Structure of the Passive Film on Mild Steel in CO₂ Corrosion Environments", *Industrial & Engineering Chemistry Research*, 2009. 48 (13): p. 6296-6302.
13. M. Nordsveen, S. Nešić, A. Stangeland, "A Mechanistic Model for Carbon Dioxide Corrosion of Mild Steel in the Presence of Protective Iron Carbonate Films—Part 1: Theory and Verification," *Corrosion*, 2003. 59(5): p.443-456.
14. S. Nešić, K.L.J. Lee, "A Mechanistic Model for Carbon Dioxide Corrosion of Mild Steel in the Presence of Protective Iron Carbonate Films—Part 3: Film Growth Model", *Corrosion*, 2003. 59 (7): p.616-627.
15. H. Li, B. Brown, S. Nešić, "Predicting Localized CO₂ Corrosion in Carbon Steel Pipelines", *Corrosion/2011*, Paper no. 253 (Houston, TX: NACE 2011)
16. S. Nešić, H. Li, J. Huang, D. Sormaz, "An Open Source Mechanistic Model for CO₂ / H₂S Corrosion of Carbon Steel", *Corrosion/2009*, Paper no. 572 (Houston, TX: NACE 2009)
17. T. Zakroczymski, C.J. Fan, Z. Szklarskasmialowska, "Passive Film Formation on Iron and Film Breakdown in A Sodium-Hydroxide Solution Containing Chloride-Ions", *Journal of the Electrochemical Society*, 1985.132(12): p. 2868-2871.
18. N. Boucherit, A.H.L. Goff, S. Joiret, "Raman Studies of Corrosion Films Grown on Fe and Fe-Mo in Pitting Conditions", *Corrosion Science*, 1991. 32(5-6): p. 497-507.
19. E.B. Castro, J.R. Vilche, A.J. Arvia, "Iron Dissolution and Passivation in K₂CO₃-KHCO₃ Solutions - Rotating-Ring-Disk Electrode and XPS Studies", *Corrosion Science*, 1991. 32(1): p. 37-50.
20. Y.F. Cheng, J.L. Luo, "Passivity and Pitting of Carbon Steel in Chromate Solutions", *Electrochimica Acta*, 1999. 44(26): p. 4795-4804.
21. P.M.L. Bonin, M. S. Odziemkowski, E. J. Reardon, R. W. Gillham, "In Situ Identification of Carbonate-Containing Green Rust on Iron Electrodes in Solutions Simulating Groundwater", *Journal of Solution Chemistry*, 2000. 29(10): p. 1061-1074.
22. L. Legrand, S. Savoye, A. Chausse, R. Messina, "Study of Oxidation Products Formed on Iron in Solutions Containing Bicarbonate/Carbonate", *Electrochimica Acta*, 2000. 46(1): p. 111-117.
23. M. Fleischmann, H.R. Thirsk, "The Growth of Thin Passivating Layers on Metallic Surfaces", *Journal of Electrochemical Society*, 1963. 110(6).

24. N. Sato, M. Cohen, "The Kinetics of Anodic Oxidation of Iron in Neutral Solution", *Journal of Electrochemical Society*, 1964. 111(5).
25. G.L. Griffin, "A Simple Phase-Transition Model For Metal Passivation Kinetics", *Journal of the Electrochemical Society*, 1984. 131(1): p. 18-21.
26. C. Sarasola, T. Fernandez, Y. Jimenez, "Potentiodynamic Passivation of Iron in KOH Solution - Application of The Layer-Pore Resistance Model", *Electrochimica Acta*, 1988. 33(10): p. 1295-1301.
27. D. Devilliers, F. Lantelme, M. Chemla, "Surface Processes - Effect of Ohmic Polarization on Potentiodynamic V/I Curves", *Electrochimica Acta*, 1986. 31(10): p. 1235-1245.
28. D.D. Macdonald, "The Point-Defect Model for The Passive State", *Journal of the Electrochemical Society*, 1992. 139(12): p. 3434-3449.
29. C.Y. Chao, L.F. Lin, D.D. Macdonald, "A Point-Defect Model for Anodic Passive Films.1. Film Growth-Kinetics", *Journal of the Electrochemical Society*, 1981. 128(6): p. 1187-1194.
30. L.F. Lin, C.Y. Chao, D.D. Macdonald, "A Point-Defect Model for Anodic Passive Films.2. Chemical Breakdown and Pit Initiation", *Journal of the Electrochemical Society*, 1981. 128(6): p. 1194-1198.
31. C.Y. Chao, L.F. Lin, D.D. Macdonald, "A Point-Defect Model for Anodic Passive Films.3. Impedance Response", *Journal of the Electrochemical Society*, 1982. 129(9): p. 1874-1879.
32. D.D. Macdonald, "Passivity - the key to our metals-based civilization", *Pure and Applied Chemistry*, 1999. 71(6): p. 951-978.
33. D.B. Hibbert, S.V. Murphy, "Kinetic-Model of Iron Corrosion and Passivity", *Journal of the Electrochemical Society*, 1991. 138(8): p. L30-L32.
34. I. Epelboin, C. Gabrielli, M. Keddam, H. Takenouti, "Model of Anodic Behavior of Iron in Sulfuric-Acid Medium", *Electrochimica Acta*, 1975. 20(11): p.913-916.
35. S.I. Pyun, M.H. Hong, "A Model Describing the Growth-Kinetics of Passivating Oxide Film Prepared Under Potentiostatic Conditions", *Electrochimica Acta*, 1992. 37(2): p. 327-332.
36. P. Meakin, T. Jossang, J. Feder, "Simple Passivation and Depassivation Model for Pitting Corrosion", *Physical Review E*, 1993. 48(4): p. 2906-2916.

37. F. Reis, J. Stafiej, J.P. Badiali, "Scaling Theory in A Model of Corrosion and Passivation", *Journal of Physical Chemistry B*, 2006. 110(35): p. 17554-17562.
38. O. R. Camacho, M.U. Macdonald, D. D. Macdonald, "Deterministic Modeling of the Corrosion of Low-Carbon Steel by Dissolved Carbon Dioxide and the Effect of Acetic Acid. I-Effect of Carbon Dioxide", in 215th ECS meeting. May 2009, the Electrochemical Society: San Francisco, CA.
39. S. Papavinasam, R. W. Revie, W. I. Friesen, A. Doiron, T. Panneerselvam, "Review of Models to Predict Internal Pitting Corrosion of Oil and Gas Pipelines", *Corrosion Reviews*, 2006. 24(3-4): p. 173-230.
40. S.M. Sharland, "A Review of the Theoretical Modeling of Crevice and Pitting Corrosion", *Corrosion Science*, 1987. 27 (3): p.289-323.
41. J.W. Oldfield and W.H. Sutton, "Crevice Corrosion of Stainless-Steels .1. Mathematical Model", *British Corrosion Journal*, 1978. 13(1): p. 13-22.
42. J.R. Galvele, "Transport Processes and Mechanism of Pitting of Metals", *Journal of the Electrochemical Society*, 1976. 123(4): p. 464-474.
43. K. Hebert, R. Alkire, "Dissolved Metal Species Mechanism for Initiation of Crevice Corrosion of Aluminum .1. Experimental Investigations in Chloride Solutions", *Journal of the Electrochemical Society*, 1983. 130(5): p. 1001-1007.
44. K. Hebert, R. Alkire, "Dissolved Metal Species Mechanism for Initiation of Crevice Corrosion of Aluminum .2. Mathematical Model", *Journal of the Electrochemical Society*, 1983. 130(5): p. 1007-1014.
45. T. Okada, "A Theory of Perturbation-Initiated Pitting", *Journal of the Electrochemical Society*, 1985. 132(3): p. 537-544.
46. D.E. Williams, C. Westcott, M. Fleischmann, "Stochastic-Models of Pitting Corrosion of Stainless-Steels .1. Modeling of the Initiation and Growth of Pits at Constant Potential", *Journal of the Electrochemical Society*, 1985. 132(8): p. 1796-1804.
47. J.L. Dawson, M.G.S. Ferreira, "Electrochemical Studies of The Pitting of Austenitic Stainless-Steel", *Corrosion Science*, 1986. 26(12): p. 1009-1026.
48. D.D. Macdonald, M. Urquidimacdonald, "Distribution-Functions for The Breakdown of Passive Films", *Electrochimica Acta*, 1986. 31(8): p. 1079-1086.

49. J.A. Bardwell, B. Macdougall, "Pitting of Iron by Chloride in Borate Buffer Solution - Role of The Anodic Oxide Film", *Journal of the Electrochemical Society*, 1988. 135(9): p. 2157-2161.
50. B. Baroux, "The Kinetics of Pit Generation on Stainless-Steels", *Corrosion Science*, 1988. 28(10): p. 969-986.
51. E. McCafferty, "A Competitive Adsorption Model for The Inhibition of Crevice Corrosion and Pitting", *Journal of the Electrochemical Society*, 1990. 137(12): p. 3731-3737.
52. T. Nagatani, "Dynamic Scaling of Pit-Size Distribution in Corrosion Patterns", *Physical Review Letters*, 1992. 68(10): p. 1616-1619.
53. T. Shibata, M.A.M. Ameer, "Stochastic-Processes of Pit Generation on Zirconium with an Anodic Oxide Film", *Corrosion Science*, 1992. 33(10): p. 1633-1643.
54. Y. Xu, M.H. Wang, H.W. Pickering, "On Electric-Field-Induced Breakdown of Passive Films and The Mechanism of Fitting Corrosion", *Journal of the Electrochemical Society*, 1993. 140(12): p. 3448-3457.
55. R.S. Lillard, J.R. Scully, "Modeling of The Factors Contributing to the Initiation and Propagation of the Crevice Corrosion of Alloy 625", *Journal of the Electrochemical Society*, 1994. 141(11): p. 3006-3015.
56. K. Darowicki, S. Krakowiak, "The Current Threshold Value in Potentiodynamic Determination of The Breakdown Potential", *Electrochimica Acta*, 1997. 42(16): p. 2559-2562.
57. Y.F. Cheng, M. Wilmott, J.L. Luo, "The Role of Chloride Ions in Pitting of Carbon Steel Studied by the Statistical Analysis of Electrochemical Noise", *Applied Surface Science*, 1999. 152(3-4): p. 161-168.
58. G. Schmitt, C. Bosch, M. Mueller, G. Siegmund, "A Probabilistic Model for Flow Induced Localized Corrosion," *CORROSION/2000*, Paper no. 49 (Houston, TX: NACE, 2000).
59. Y. Yang, B. Brown, S. Nešić, M. E. Gennaro, B. Molinas, "Mechanical Strength and Removal of a Protective Iron Carbonate Layer Formed on Mild Steel in CO₂ Corrosion", *Corrosion/2010*, Paper no. 383 (Houston, TX: NACE, 2010)
60. M. Ergun, L. Akcay, "Investigation of Pitting Potential of Carbon Steel Using Experimental Design Method", *British Corrosion Journal*, 2002. 37(3): p. 235-238.

61. Z. Szklarska-Smialowska, "Mechanism of Pit Nucleation by Electrical Breakdown of the Passive Film", *Corrosion Science*, 2002. 44(5): p. 1143-1149.
62. R. Nyborg, A. Dugstad, "Understanding and Prediction of Mesa Corrosion Attack", *Corrosion/2003*, Paper no. 642(Houston, TX: NACE, 2003).
63. S. Nešić, M. Nordsveen, R. Nyborg, A. Stangeland , "A Mechanistic Model for CO₂ Corrosion with Protective Iron Carbonate Films", *Corrosion/2001*, Paper no. 40(Houston, TX: NACE, 2001).
64. X. Ying, "A Two-dimensional Stochastic Model for Prediction of Localized Corrosion," M.S. Thesis, Ohio University, 2004.
65. E.W.J. Van Hunnik, B.F.M. Pots, "The Formation of Protective FeCO₃ Corrosion Product Layers in CO₂ Corrosion", *Corrosion* 96, Paper No.6.
66. P. Marcus, V. Maurice, H.H. Strehblow, "Localized Corrosion (Pitting): a Model of Passivity Breakdown Including the Role of the Oxide Layer Nanostructure", *Corrosion Science*, 2008. 50(9): p. 2698-2704.
67. H.W. Pickering, R.P. Frankent, "Mechanism of Localized Corrosion of Iron and Stainless-Steel .1. Electrochemical Studies", *Journal of the Electrochemical Society*, 1972. 119(10): p. 1297-.
68. R. Alkire, D. Ernsberger, D. Damon, "Role of Conductivity Variations Within Artificial Pits During Anodic-Dissolution", *Journal of the Electrochemical Society*, 1976. 123(4): p. 458-464.
69. R. Alkire, D. Siitari, "Location of Cathodic Reaction During Localized Corrosion", *Journal of the Electrochemical Society*, 1979. 126(1): p. 15-22.
70. J.N. Harb, R.C. Alkire, "Transport and Reaction During Pitting Corrosion of Ni in 0.5m NaCl .1. Stagnant Fluid", *Journal of the Electrochemical Society*, 1991. 138(9): p. 2594-2600.
71. J.N. Harb, R.C. Alkire, "Transport and Reaction During Pitting Corrosion of Ni in 0.5m NaCl .2. Flowing Fluid", *Journal of the Electrochemical Society*, 1991. 138(12): p. 3568-3575.
72. J.R. Galvele, "Transport Processes and Mechanism of Pitting of Metals", *Journal of the Electrochemical Society*, 1976. 123(4): p. 464-474.
73. J.R. Galvele, "Transport Processes in Passivity Breakdown.2. Full Hydrolysis if the Metal-Ions", *Corrosion Science*, 1981. 21(8): p. 551-579.

74. S.M. Gravano, J.R. Galvele, "Transport Processes in Passivity Breakdown .3. Full Hydrolysis Plus Ion Migration Plus Buffers", *Corrosion Science*, 1984. 24(6): p. 517-534.
75. E., R. Bardal, Johnsen, P.O. Gartland, "Prediction of Galvanic Corrosion Rates and Distribution by Means of Calculation and Experimental-Models", *Corrosion*, 1984. 40(12): p. 628-633.
76. J.W. Fu, S.K. Chan, "A Finite-Element Method for Modeling Localized Corrosion Cells", *Corrosion*, 1984. 40(10): p. 540-544.
77. A. Benrais, J.C. Sohm, "Aluminum Pit Propagation in Acidic Media .2. Theoretical-Model", *Corrosion Science*, 1985. 25(11): p. 1047-1056.
78. S.M. Sharland, P.W. Tasker, "A Mathematical-Model of Crevice and Pitting Corrosion .1. The Physical Model", *Corrosion Science*, 1988. 28(6): p. 603-620.
79. S.M. Sharland, "A Mathematical-Model of Crevice And Pitting Corrosion .2. The Mathematical Solution", *Corrosion Science*, 1988. 28(6): p. 621-630.
80. K. Heppner, "Development of Predictive Models of Flow Induced and Localized Corrosion," Ph. D. Dissertation, University of Saskatchewan, May 2006.
81. J.C. Walton, G. Cragolino, S.K. Kalandros, "A Numerical Model of Crevice Corrosion for Passive and Active Metals", *Corrosion Science*, 1996. 38(1): p. 1-18.
82. Y. Xu, H.W. Pickering, "The Initial Potential and Current Distributions of the Crevice Corrosion Process", *Journal of the Electrochemical Society*, 1993. 140(3): p. 658-668.
83. M.H. Wang, H.W. Pickering, Y. Xu, "Potential Distribution, Shape Evolution, and Modeling of Pit Growth for Ni In Sulfuric-Acid", *Journal of the Electrochemical Society*, 1995. 142(9): p. 2986-2995.
84. M. H. Achour, J. Kolts, A. H. Johannes, G. Liu, "Mechanistic Modeling of Pit Propagation in CO₂ Environment under High Turbulence Effects", *Corrosion/93*, Paper No. 87 (Houston, TX: NACE, 1993)
85. G. Engelhardt, D.D. Macdonald, "Estimation of Corrosion Cavity Growth Rate for Predicting System Service Life", *Corrosion Science*, 2004. 46(5): p. 1159-1187.
86. N.J. Laycock, S.P. White, "Computer Simulation of Single Pit Propagation in Stainless Steel under Potentiostatic Control", *Journal of the Electrochemical Society*, 2001. 148(7): p. B264-B275.

87. N. J. Laycock, Noh, J. S., White, S. P., Krouse, D. P., "Computer Simulation of Pitting Potential Measurements", *Corrosion Science*, 2005. 47(12): p. 3140-3177.
88. B. Malki, B. Baroux, "Computer Simulation of the Corrosion Pit Growth", *Corrosion Science*, 2005. 47(1): p. 171-182.
89. S. Scheiner and C. Hellmich, "Stable Pitting Corrosion of Stainless Steel as Diffusion-Controlled Dissolution Process With A Sharp Moving Electrode Boundary", *Corrosion Science*, 2007. 49(2): p. 319-346.
90. A.S. Agarwal, U. Landau, J.H. Payer, "Modeling Particulates Effects on the Cathode Current Capacity in Crevice Corrosion", *Journal of the Electrochemical Society*, 2008. 155(5): p. C269-C278.
91. D. A. G. Bruggeman, *Annals of Physics*, 1935. 24: p.636.
92. J. Han, S. Nešić, B. Brown, "Galvanic Model for Localized CO₂ Corrosion", ICC (International Corrosion Congress) 2008, paper no. 2687(Houston, TX: NACE, 2009).
93. J. Amri, E. Gulbrandsen, R.P. Nogueira, "Numerical Simulation of A Single Corrosion Pit in CO₂ and Acetic Acid Environments", *Corrosion Science*, 2010. 52(5): p. 1728-1737.
94. E. Eriksrud, T. Sontvedt, "Effect of Flow on CO₂ Corrosion Rates in Real and Synthetic Formation Waters", in *Advances in CO₂ Corrosion, Vol.1. Proc. Corrosion/83 Symp. CO₂ Corrosion in the Oil and Gas Industry*, eds. R.H.Hausler, H.P.Goddard (Houston, TX: NACE,1984), p:20.
95. V. Fajardo N. R., "Localized CO₂ Corrosion in the Presence of Organic Acids", MS Thesis, Ohio University, March 2011.
96. K. George, S. Nešić, "Electrochemical Investigation and Modeling of Carbon Dioxide Corrosion of Carbon Steel in the Presence of Acetic Acid", *Corrosion/2004*, Paper no. 04379. (Houston, TX: NACE 2004)
97. Y. Garsany, D. Pletcher, B. Hedges, "The Role of Acetate in CO₂ Corrosion of Carbon Steel: Has the Chemistry Been Forgotten?" *CORROSION/2002*, Paper no. 273, (Houston, TX: NACE 2002).
98. E.W.J. van Hunnik, B.F.M. Pots, E.L.J.A. Hendriksen, "The Formation of Protective FeCO₃ Corrosion Product Layers in CO₂ Corrosion," *CORROSION/96*, paper no. 6 (Houston, TX: NACE, 1996).

99. W. Sun, S. Nešić, "Kinetics of Corrosion Layer Formation: Part 1 - Iron Carbonate Layers on Carbon Dioxide Corrosion", *Corrosion*, 2008. 64(4): p. 334-346.
100. J.W. Mullin, *Crystallization*, 3rd ed. (Oxford, U.K.: Oxford Press, 1993).
101. J. K. L. Lee, "MULTICORP v4.0", CCJIP Board Meeting presentation, Institute for Corrosion and Multiphase Technology, Ohio University, October 2007.
102. J. R. Vera, D. Shirah, F. Song, "Laboratory Evaluation of Galvanic CO₂ Corrosion and Inhibition of Carbon Steel Piping Partially Clad With Alloy 625", NACE/2009, Paper no. 566 (Houston, TX: NACE, 2009).
103. ASTM G61-86(1998) Standard Test Method for Conducting Cyclic Potentiodynamic Polarization Measurements for Localized Corrosion Susceptibility of Iron-, Nickel-, or Cobalt-Based Alloys.
104. D. C. Montgomery, G. C. Runger, N. F. Hubele, *Engineering Statistics*, 4th edition (John Wiley, 2007).
105. J. Han, B. Brown, S. Nešić, "Investigation of the Galvanic Mechanism for Localized Carbon Dioxide Corrosion Propagation Using the Artificial Pit Technique", *Corrosion*, 2010. 66(9).
106. R.H. Perry, D. Green, *Perry's Chemical Engineers' Handbook*, 50th edition, New York, NY: McGraw-Hill, 1984.
107. J. Kvarekvål, "A Kinetic Model for Calculating Concentration Profiles and Fluxes of CO₂-Related Species across the Nernst Diffusion Layer", *CORROSION/97*, paper no. 5 (Houston, TX: NACE, 1997).
108. J.S. Newman, *Electrochemical Systems*, 2nd edition (Englewood Cliffs, NJ: Prentice Hall, 1991).
109. R.T. Ferrell, D.M. Himmelbl, "Diffusion Coefficients of Hydrogen and Helium in Water", *AICHE Journal*, 1967. 13(4): p. 702-&.
110. J.T. Davies, *Turbulence Phenomena* (London, U.K.: Academic Press, 1972).
111. S. Patankar, *Numerical Heat Transfer and Fluid Flow*, 1st edition (Taylor & Francis, 1980).
112. K.L.J. Lee, "A Mechanistic Modeling of CO₂ Corrosion of Mild Steel in The Presence of H₂S", PhD dissertation, Ohio University, November 2004.

113. G. Papadakis, G. Bergeles, "A Locally-Modified Second-Order Upwind Scheme for Convection-Term Discretization", in: Taylor (Ed.), Proceedings of the Eighth International Conference on Numerical Methods in Laminar and Turbulent Flow, Swansea, July, Pineridge Press, Swansea, 1993, p. 577.
114. R.F. Warming, R.M. Beam, "Upwind Second-order Difference Schemes and Application in Aerodynamics Flows", American Institute of Aeronautics and Astronautics Journal, 14 (9) (1976) p. 1241-1249.
115. B. Koren, "Upwind Discretization of the Steady Navier–Stokes Equations", International Journal of Numerical Methods in Fluids, 1990. 11 (1): p. 99-117.
116. B. Koren, "A Robust Upwind Discretization Method for Advection, Diffusion and Source Terms", in: Vreugdenhil, Koren (Eds.), Numerical Methods for Advection–Diffusion Problems, Vieweg, Braunschweig, 1993, p. 117.
117. J. J. Wei, B. Yu, W. Q. Tao, Y. Kawaguchi, H.S. Wang, "A New High-order Accurate and Bounded Scheme for Incompressible Flow", Numerical Heat Transfer, Part B 43, 2003, p. 19.
118. P.L. Roe," Some Contributions to the Modeling of Discontinuous Flows", in: Engquist, Osher, Somerville, (Eds.), Lectures in Applied Mathematics, Large-scale Computations in Fluid Mechanics (AMS-SIAM Summer Seminar, La Jolla, CA, USA, 1983), American Mathematical Society, Part 2, 1985, p. 163.
119. N.P. Waterson, H. Deconinck, "A Unified Approach to the Design and Application of Bounded Higher-order Convection Schemes", in Taylor, Durbetaki (Eds.), Proceedings of the Ninth International Conference on Numerical Methods in Laminar and Turbulent Flow, Atlanta, July, Pineridge Press, Swansea, 1995, p. 203.
120. B. van Leer, "Towards the Ultimate Conservative Difference Scheme. II. Monotonicity and Conservation Combined in A Second-Order Scheme", Journal of Computational Physics, 1974. 14: p.361.
121. B. van Leer, "Towards the Ultimate Conservative Difference Scheme. IV. A New Approach to Numerical Convection", Journal of Computational Physics, 1977. 23: p.276.
122. N.P. Waterson, H. Deconinck, "Design Principles for Bounded Higher-order Convection Schemes - A Unified Approach", Journal of Computational Physics, 2007. 224(1): p. 182-207.
123. C.M. Chen, K. Aral, "A Computer Program for Constructing Stability Diagrams in Aqueous Solutions at Elevated Temperatures", Corrosion,38(4): p.183-190.

124. C. M. Criss, J. W. Cobble, "The Thermodynamic Properties of High-Temperature Aqueous Solutions. IV. Entropies of the Ions up to 200° and the Correspondence Principle", *Journal of the American Chemical Society*, 1964a. 86(24): p.5385-90.
125. H. Ascher, *Repairable Systems Reliability— Modeling, Inference, Misconceptions and Their Causes* (New York, Marcel Dekker, 1984).
126. DNV RP G101, "Risk Based Inspection of Offshore Topsides Static Mechanical Equipment", DET NORISK VERITAS, Norway (January 2002).
127. J. E. Gentle, *Statistics and Computing: Random Number Generation and Monte Carlo Method*, (Springer-Verlag New York, Inc., 1998).
128. W. Gao, N. M. Sammes, "An introduction to Electronic and Ionic Materials", (World Scientific Publishing Co. Pte.Ltd., 1999).
129. J.D.V. Horn," Electronic Table of Shannon Ionic Radii. 2001", Available from: <http://v.web.umkc.edu/vanhornj/Radii.xls>, cited March 2010.
130. D.D. Macdonald, M. Urquidimacdonald, "*Theory of Steady-State Passive Films*", *Journal of the Electrochemical Society*, 1990. 137(8): p. 2395-2402.
131. S. Nešić, J. Postlethwaite, S. Olsen, "An Electrochemical Model for Prediction of Corrosion of Mild Steel in Aqueous Carbon Dioxide Solutions", *Corrosion*, 1996. 52(4): p. 280-294.
132. W. Sun, S. Nešić, "A Mechanistic Model of H₂S Corrosion of Mild Steel", *Corrosion/2007*, Paper no. 655. (Houston, TX: NACE 2007)
133. J. Oddo and M. Tomson, "Simplified calculation of CaCO₃ saturation at high temperatures and pressures in brine solutions", SPE of AIME (Richardson, TX: Society of Petroleum Engineers, 1982), 1583-1590.
134. D. A. Palmer, R. van Eldik, "The Chemistry of Metal Carbonate and Carbon-Dioxide Complexes", *Chemical Reviews*, 1983. 83(6): p. 651-731.
135. S. Nešić, B.F.M. Pots, J. Postlethwaite , N. Thevenot, "Superposition of diffusion and chemical reaction controlled limiting currents - Application to Corrosion", *The Journal of Corrosion Science and Engineering*, Vol.1, paper no. 3, 1995.
136. F.P. Berger, K.-F.F.-L. Hau, "Mass-Transfer in Turbulent Pipe-Flow Measured by Electrochemical Method", *International Journal of Heat and Mass Transfer*, 1977. 20(11): p.1185-1194.

137. D.R.Lide, CRC Handbook of Chemistry and Physics, 75th edition (New York, NY: CRC Press, 1995).

138. FREECORP user manual, Ohio University,
<http://www.corrosioncenter.ohiou.edu/freecorp/pdfs/FREECORP-Background.pdf>

139. I. H. Omar, Y. M. Gunaltun, J. Kvarekval, A. Dugstad, "Corrosion of Carbon Steel under Simulated Kashagan Field Conditions", paper no. 300. (Houston, TX: NACE 2005)

APPENDIX 1: DERIVATION OF THE EQUATION FOR FeCO_3 LAYER DISSOLUTION

FeCO_3 layer dissolution, Equation (136), is based on the assumption that the process is under mass transfer control implying that supersaturation of FeCO_3 on the film surface is maintained at 1.¹⁰¹



Let Δc mol/L FeCO_3 dissolves during the time period of Δt , due to mass balance:

$$\Delta c = \Delta c_{\text{Fe}^{2+}} = \Delta c_{\text{CO}_3^{2-}} \quad (137)$$

The supersaturation of FeCO_3 at film surface is given by:

$$SS_{\text{FeCO}_3} = \frac{(c_{\text{Fe}^{2+}} + \Delta c)(c_{\text{CO}_3^{2-}} + \Delta c)}{Ksp_{\text{FeCO}_3}} = 1 \quad (138)$$

Solution of Equation (138) for Δc yields:

$$\Delta c = \frac{-(c_{\text{Fe}^{2+}} + c_{\text{CO}_3^{2-}}) + \sqrt{(c_{\text{Fe}^{2+}} - c_{\text{CO}_3^{2-}})^2 + 4Ksp_{\text{FeCO}_3}}}{2} \quad (139)$$

By definition, the dissolution rate of FeCO_3 is given by:

$$R_{dis} = \frac{dc}{dt} \quad (140)$$

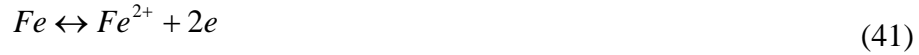
Substitute Equation (139) into (140) yields:

$$R_{dis} = \frac{-(c_{\text{Fe}^{2+}} + c_{\text{CO}_3^{2-}}) + \sqrt{(c_{\text{Fe}^{2+}} - c_{\text{CO}_3^{2-}})^2 + 4Ksp_{\text{FeCO}_3}}}{2\Delta t} \quad (141)$$

Where R_{dis} is FeCO_3 dissolution rate in $\text{mol}/(\text{m}^3 \cdot \text{s})$; $c_{\text{Fe}^{2+}}, c_{\text{CO}_3^{2-}}$:concentration of Fe^{2+} and CO_3^{2-} in mol/m^3 ; SS_{FeCO_3} is supersaturation of FeCO_3 ; $K_{sp_{\text{FeCO}_3}}$ is the solubility limit of FeCO_3 , t is time in sec.

APPENDIX 2: DERIVATION OF THE EXCHANGE CURRENT DENSITY FOR
IRON OXIDATION

For Fe oxidation:



The reversible potential is given by the Nernst equation as:

$$\begin{aligned} E_{rev} &= E_{rev}^o - \frac{RT}{2F} \ln \frac{1}{c_{Fe^{2+}}} \\ &= E_{rev}^o + \frac{RT}{2F} \ln c_{Fe^{2+}} \end{aligned} \quad (41)$$

For a reaction kinetics following Tafel behavior as shown in Figure 40,

$$E_0 - E_{rev} = b_a \cdot (\log i_0 - \log i_{rev}) \quad (142)$$

In the previous model, E_0 , i_0 and b_a are respectively given as:¹³

$$E_0 = -0.488V \quad (143)$$

$$i_0 = 1 \cdot e^{-\frac{\Delta H}{R} \left(\frac{1}{T} - \frac{1}{T_{ref}} \right)} \quad (144)$$

$$b_a = \frac{2.303RT}{1.5F} \quad (145)$$

Substituting Equations (41) and (143) through (145) into Equation (142) yields:

$$-0.488 - E_{rev}^o - \frac{RT}{2F} \ln c_{Fe^{2+}} = \frac{2.303RT}{1.5F} \cdot (\log e^{-\frac{\Delta H}{R} \left(\frac{1}{T} - \frac{1}{T_{ref}} \right)} - \log i_{rev}) \quad (146)$$

$$\frac{-0.488 - E_{rev}^o - \frac{RT}{2F} \ln c_{Fe^{2+}}}{\frac{2.303RT}{1.5F}} = 2.303 \cdot \left(\log e^{e^{-\frac{\Delta H}{R} \left(\frac{1}{T} - \frac{1}{T_{ref}} \right)}} - \log i_{rev} \right) \quad (147)$$

$$\frac{-0.488 - E_{rev}^o - \frac{RT}{2F} \ln c_{Fe^{2+}}}{\frac{RT}{1.5F}} = \ln e^{-\frac{\Delta H}{R} \left(\frac{1}{T} - \frac{1}{T_{ref}} \right)} - \ln i_{rev} \quad (148)$$

$$\frac{-(0.488 + E_{rev}^o)}{\frac{RT}{1.5F}} - \frac{1.5}{2} \ln c_{Fe^{2+}} = -\frac{\Delta H}{R} \left(\frac{1}{T} - \frac{1}{T_{ref}} \right) - \ln i_{rev} \quad (149)$$

$$\ln i_{rev} = \frac{835.6}{T} + \ln c_{Fe^{2+}}^{0.75} - \frac{\Delta H}{R} \left(\frac{1}{T} - \frac{1}{T_{ref}} \right) \quad (150)$$

$$i_{rev} = e^{\frac{835.6}{T}} \cdot c_{Fe^{2+}}^{0.75} \cdot e^{-\frac{\Delta H}{R} \left(\frac{1}{T} - \frac{1}{T_{ref}} \right)} \quad (151)$$

Where E_{rev} : reversible potential of Fe oxidation, V; E_{rev}^o : reversible potential of Fe oxidation at standard conditions, -0.44V vs. SHE; R : universal gas constant, 8.3145 J/mol.K; T : temperature, Kelvin; F : Faraday constant, 96485C/mol; $c_{Fe^{2+}}$: surface concentration, mol/L; E_0 : a reference potential, -0.488V; i_0 : anodic current density at the reference potential, A/m²; i_{rev} : exchange current density at the reversible potential, A/m²; ΔH : activation energy for Fe oxidation, 37.5kJ/mol; b_a : anodic Tafel slope for Fe oxidation; T_{ref} : reference temperature for Fe oxidation, K.

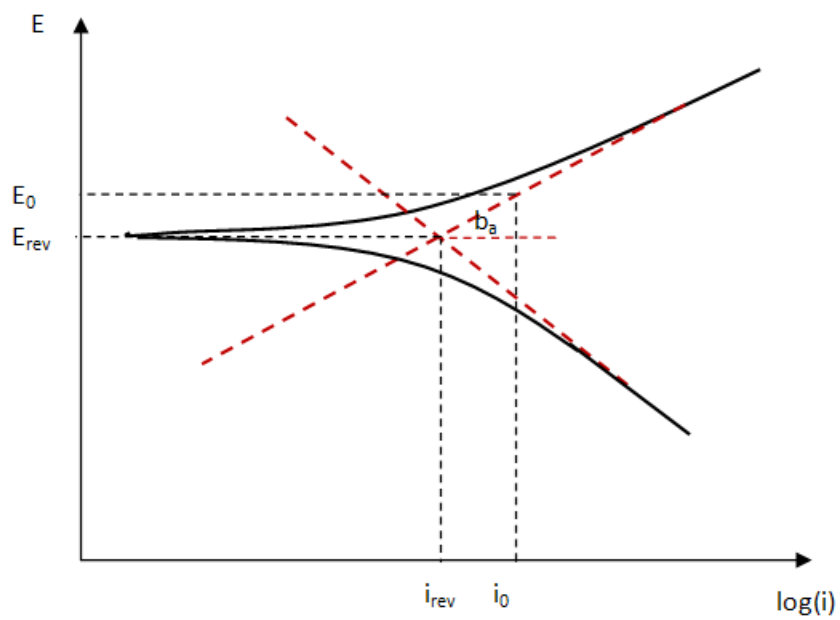


Figure 40. E-i diagram for Fe oxidation. i_{rev} can be obtained from the point (E_0, i_0) , the Tafel slope b_a and E_{rev} .

APPENDIX 3: DERIVATION OF THE EXCHANGE CURRENT DENSITY FOR H⁺ REDUCTION

For H⁺ reduction,



The reversible potential is given by the Nernst equation as:

$$\begin{aligned} E_{rev} &= E_{rev}^o - \frac{RT}{F} \ln \frac{p_{H_2}^{0.5}}{c_{H^+}} \\ &= \frac{RT}{F} \ln(p_{H_2}^{0.5} \cdot c_{H^+}) \end{aligned} \quad (153)$$

For a cathodic reaction kinetics following Tafel behavior as shown in Figure 41:

$$\frac{E_{rev} - E_0}{\log i_{rev} - \log i_0} = b_c \quad (154)$$

E_0 , i_0 and b_c have been respectively given as:

$$E_0 = \frac{RT}{F} \ln(c_{H^+}) \quad (155)$$

$$i_0 = i_{ref} \cdot e^{-\frac{\Delta H}{R} \left(\frac{1}{T} - \frac{1}{T_{ref}} \right)} \quad (156)$$

$$b_c = \frac{2.303RT}{0.5F} \quad (157)$$

Substituting Equations (153) and (155) through (157) and into Equation (154)

yields:

$$\frac{\frac{RT}{F} \ln(p_{H_2}^{0.5} \cdot c_{H^+}) - \frac{RT}{F} \ln(c_{H^+})}{\log i_{rev} - \log i_0} = \frac{2.303RT}{0.5F} \quad (158)$$

$$\frac{\ln(p_{H_2}^{0.5} \cdot c_{H^+}) - \ln(c_{H^+})}{\ln(i_{rev}) - \ln(i_0)} = 2 \quad (159)$$

$$\ln\left(\frac{p_{H_2}^{0.5} \cdot c_{H^+}}{c_{H^+}}\right) = 2 \ln\left(\frac{i_{rev}}{i_0}\right) \quad (160)$$

$$p_{H_2}^{0.5} = \left(\frac{i_{rev}}{i_0}\right)^2 \quad (161)$$

$$i_{rev} = i_0 \cdot p_{H_2}^{0.25} \quad (162)$$

Where E_{rev} : reversible potential of H^+ reduction, V; E_{rev}^o : reversible potential of H^+ reduction at standard conditions, 0V vs. SHE; R : universal gas constant, 8.3145 J/mol.K; T : temperature, Kelvin; F : Faraday constant, 96485C/mol; c_{H^+} : surface concentration of H^+ , mol/L; p_{H_2} : partial pressure of Hydrogen gas at metal surface, Pa; E_0 : a reference potential; i_0 : anodic current density at the reference potential, A/m²; i_{rev} : exchange current density at the reversible potential, A/m²; ΔH : activation energy for Fe oxidation, 37.5kJ/mol; b_c : cathodic Tafel slope for Fe oxidation; T_{ref} : reference temperature for Fe oxidation, K.

Note: although this derivation is demonstrated for H^+ reduction, it can be shown that similar expressions can be obtained for H_2CO_3 reduction and HAc reduction due to thermodynamic equivalence of these reactions.

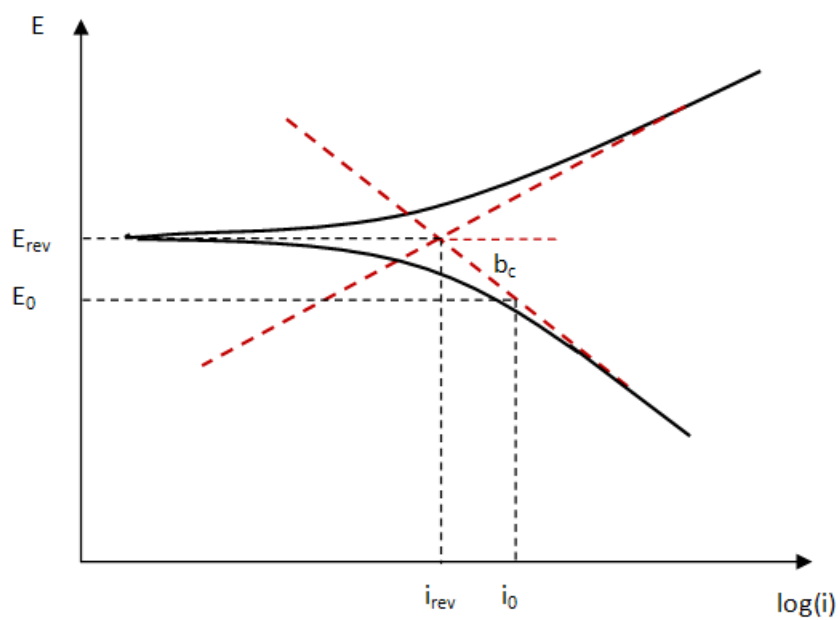


Figure 41. E-i diagram for H^+ reduction. i_{rev} can be obtained from the point (E_0, i_0) , the Tafel slope b_c and E_{rev} .

APPENDIX 4: DETERMINATION OF THE ENVIRONMENTAL PARAMETERS AFFECTING PSEUDO-PASSIVE CURRENT DENSITY OF CARBON STEEL BY CYCLIC POLARIZATION TECHNIQUE

A4.1 Test Procedure and Test Matrix

In these experiments, cyclic polarization technique was utilized to measure the pseudo-passive current density under various combinations of pH, temperature and chloride concentration. The test procedure is given by ASTM G61-1998¹⁰³ and a brief description of the procedure is presented here.

- Prepare the solution, and raise the temperature to the desired level.
- Purge solution with high purity CO₂ gas (purity>99.99%) for at least 1 hour. Then adjust solution pH to the appropriate value with HCl or NaCO₃ solution.
- Wet grind cylindrical coupon made from carbon steel C1018 using 150-grit sand paper followed by 600-grit sand paper made of silicon carbide. Rinse the coupon with deionized water and iso-propanol, respectively.
- Dry the coupon in cool air. Set the coupon in still in the solution for at least 1 hour before the test.
- Anodically polarize the coupon at the rate of 0.6V/hour starting from the open circuit potential, until current reaches 54 mA or potential reaches the level at which water oxidation occurs, and then cathodically polarize back towards the open circuit potential.

The test is terminated whenever open circuit potential is reached or hysteresis loop of the polarization curve is closed. The test conditions are listed in Table 6.

Table 6. Test conditions for cyclic polarization test

Test method	cyclic polarization
Test equipment	Glass cell
Test specimen	C1018
Total Pressure	1bar
Temperature	60 °C and 80 °C
pH	7 and 8
Velocity	stagnant
NaCl concentration	0.2 mol/L and 2 mol/L
Sweep rate	0.1667mV/s (ASTM G61)

To facilitate the analysis of test results and obtain quantitative information for the tested parameters, the factorial experiment design technique was used to formulate the test matrix.¹⁰⁴ A 2^3 test matrix was designed, where two extreme levels of values were assigned to each parameter. All possible combinations of parameters were tested, which gives a total number of 8 tests. The test matrix is listed in Table 7.

Table 7. Test matrix for factorial design experiments

Test number	pH	Temp/°C	NaCl/ mol/L
1	7	60	0.2
2	8	60	0.2
3	7	80	0.2
4	8	80	0.2
5	7	60	2
6	8	60	2
7	7	80	2
8	8	80	2

A4.2 Test Results

Figure 42 through Figure 49 show the cyclic polarization curves obtained for each condition.

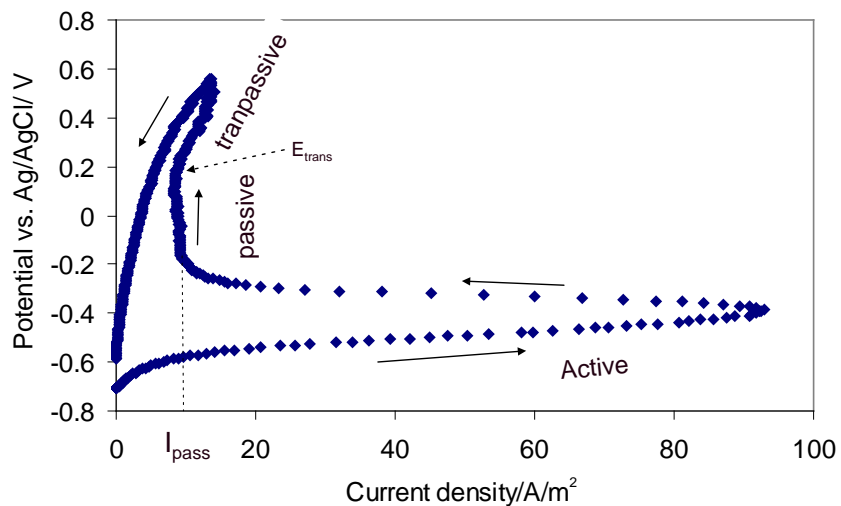


Figure 42. Cyclic polarization curve of C1018. Test conditions: T=60°C, pH=7, NaCl=0.2 mol/L.

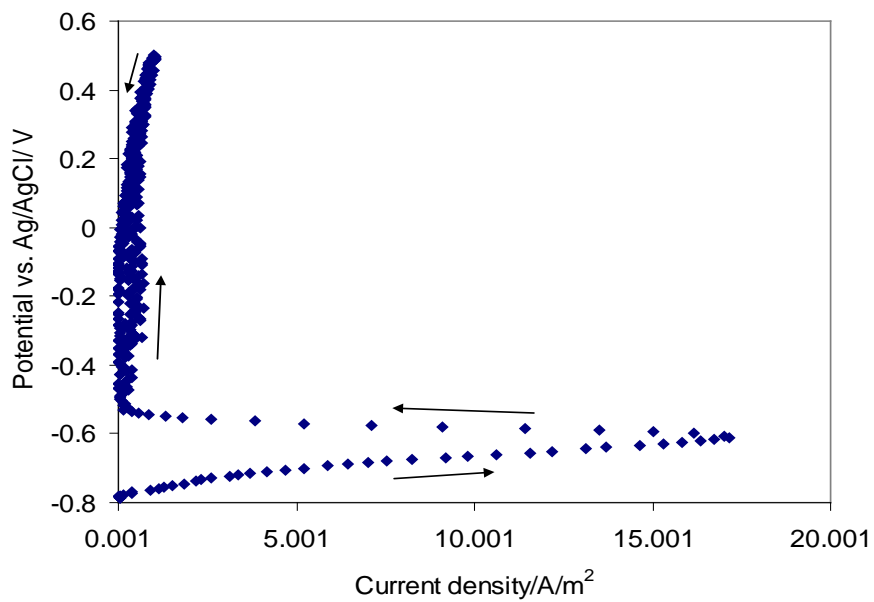


Figure 43. Cyclic polarization curve of C1018. Test conditions: T=60°C, pH=8, NaCl=0.2 mol/L.

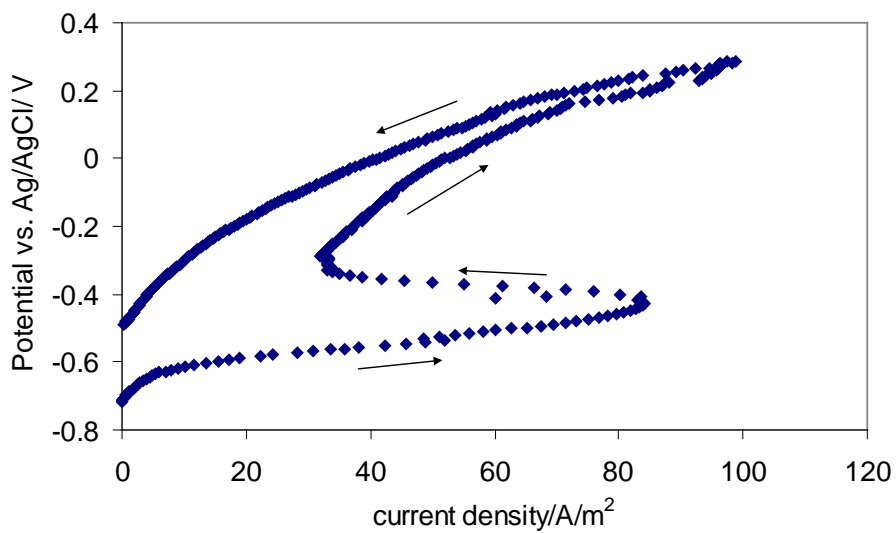


Figure 44. Cyclic polarization curve of C1018. Test conditions: T=80°C, pH=7, NaCl=0.2 mol/L.

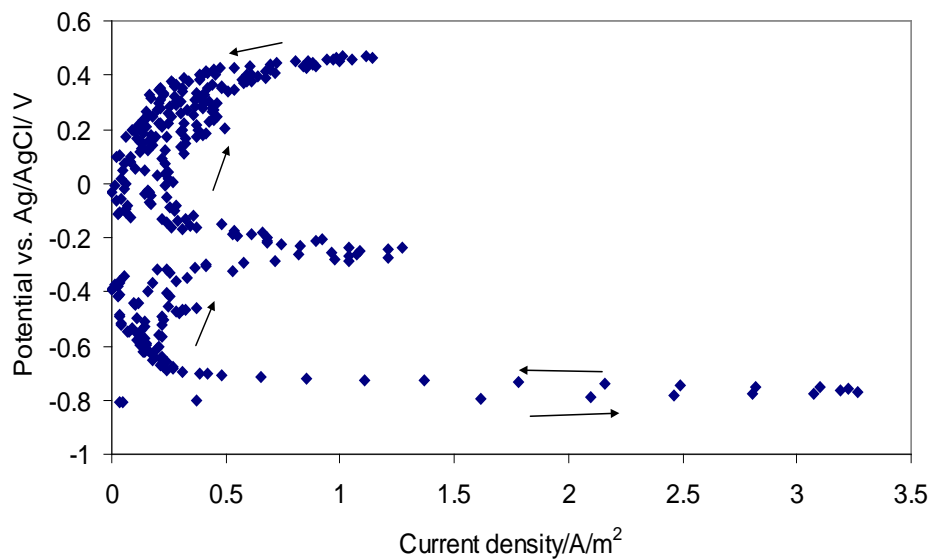


Figure 45. Cyclic polarization curve of C1018. Test conditions: T=80°C, pH=8, NaCl=0.2 mol/L.

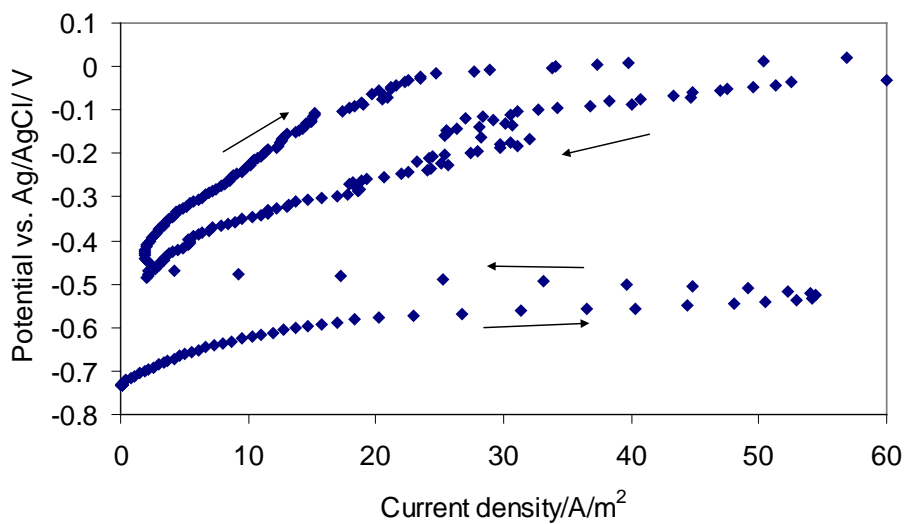


Figure 46. Cyclic polarization curve of C1018. Test conditions: T=60°C, pH=7, NaCl=2 mol/L.

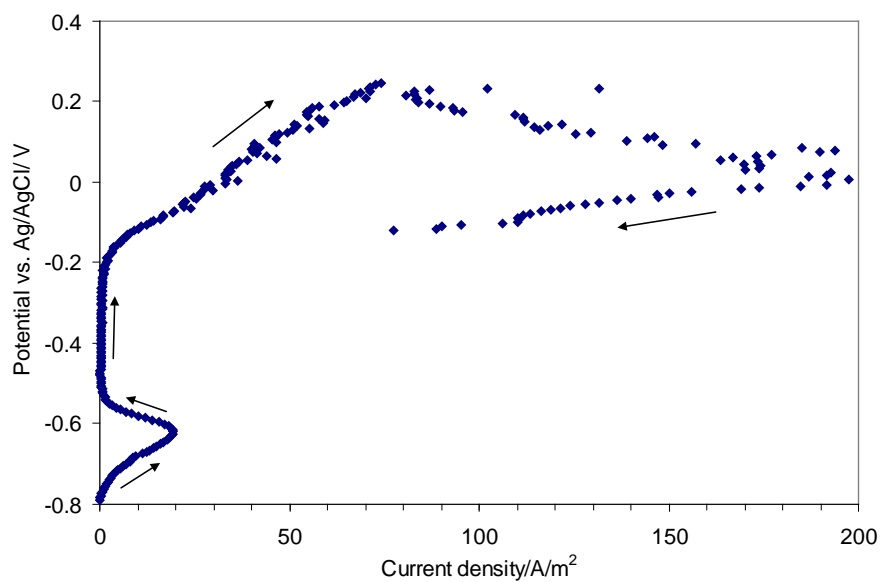


Figure 47. Cyclic polarization curve of C1018. Test conditions: T=60°C, pH=8, NaCl=2 mol/L.

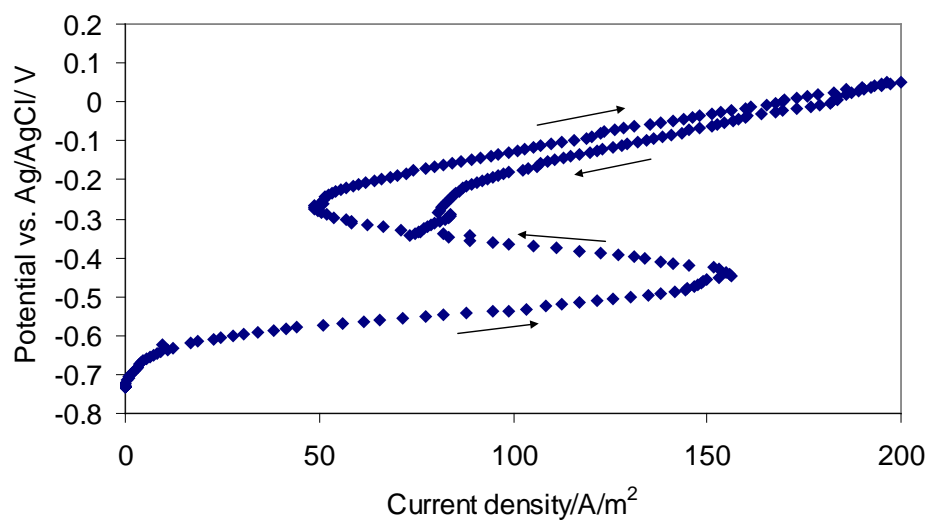


Figure 48. Cyclic polarization curve of C1018. Test conditions: T=80°C, pH=7, NaCl=2 mol/L.

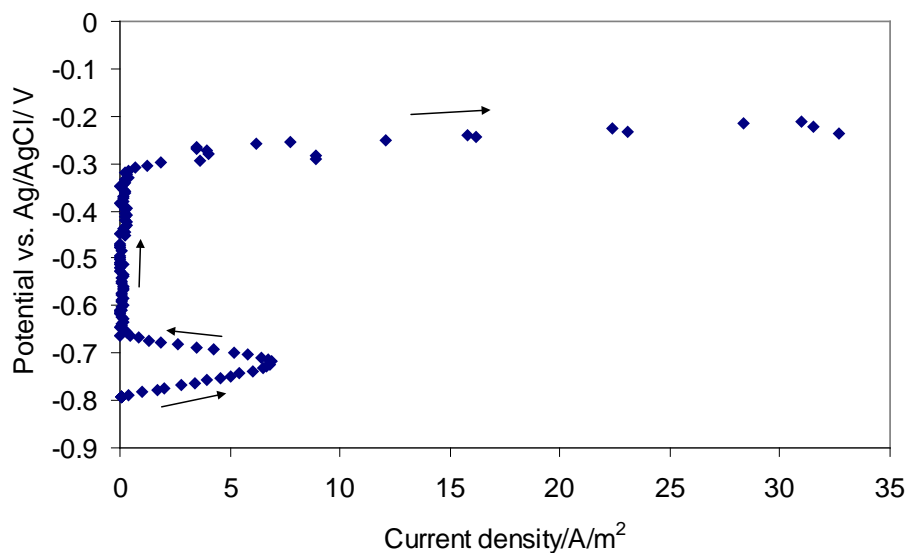


Figure 49. Cyclic polarization curve of C1018. Test conditions: $T=80^{\circ}\text{C}$, $\text{pH}=8$, $\text{NaCl}=2$ mol/L.

The pseudo-passive current density is summarized in Table 8.

Table 8. Summary of the results for cyclic polarization tests

Test number	pH	Temp/ $^{\circ}\text{C}$	NaCl/ mol/L	Passive current density/A/m ²
1	7	60	0.2	8~9
2	8	60	0.2	0.03~0.7
3	7	80	0.2	~33
4	8	80	0.2	0.02~0.1
5	7	60	2	~2
6	8	60	2	0.2~0.5
7	7	80	2	~50
8	8	80	2	0.03~0.2

A4.3 Test Result Analysis

The factorial effect analysis was performed to provide a quantitative evaluation of the effect of factors (parameters) on pseudo-passive current density. A matrix containing the geometric notation of different factors together with the target parameters (pseudo-passive current density) is shown in Table 9. This matrix was used to numerically evaluate the effect of individual factors and interaction between factors on the target parameters. The effect of parameters is calculated as:

$$E = \frac{1}{4} \sum_{i=1}^8 (\alpha_i \cdot P_i) \quad (163)$$

Where E: effect of a particular factor; i : the number of experiment; α : Factorial effect coefficient associated with each factor found in Table 9; P: values of target parameters (pseudo-passive current density) obtained in each experiment. The more the value of E deviates from 0, the more significant the corresponding parameter(s) would be.

For instance, to determine the effect of pH on the pseudo-passive current density, the following equation is used:

$$E_{pH} = \frac{1}{4} (-1 \times 8.5 + 1 \times 0.36 + (-1) \times 33 + 1 \times 0.06 + (-1) \times 2 + 1 \times 0.35 + (-1) \times 50 + 1 \times 0.12) \quad (164)$$

which gives a value of -23.15. The negative value of E_{pH} indicates that increase of pH would lead to a decrease of pseudo-passive current density, and vice versa.

The results of factorial effect analysis on pseudo-passive current density are summarized in Table 3.

Table 9. Matrix used for performing factorial effect analysis

Run	Factorial Effect Coefficient							Passive current density/A/m ²
	pH	T	pH & T	Cl ⁻	pH & Cl ⁻	T & Cl ⁻	pH&T&Cl ⁻	
1	-1	-1	1	-1	1	1	-1	8.5
2	1	-1	-1	-1	-1	1	1	0.36
3	-1	1	-1	-1	1	-1	1	33
4	1	1	1	-1	-1	-1	-1	0.06
5	-1	-1	1	1	-1	-1	1	2
6	1	-1	-1	1	1	-1	-1	0.35
7	-1	1	-1	1	-1	1	-1	50
8	1	1	1	1	1	1	1	0.12

Table 3. Effect of factors on passive current density

Factors	Effect
pH	-23.15
T	17.99
pH & T	-18.26
[Cl ⁻]	2.64
pH & [Cl ⁻]	-2.61
T & [Cl ⁻]	5.89
pH & T & [Cl ⁻]	-5.86

APPENDIX 5: MODELING PSEUDO-PASSIVE CURRENT DENSITY OF CARBON STEEL IN CO₂ ENVIRONMENT BASED ON POINT DEFECT MODEL

A5.1 Introduction

The Point Defect Model is considered to be one of the most successful mechanistic models describing passivity; it was originally developed by D. Macdonald and his colleagues beginning in the early 1980s.²⁸⁻³¹ The model is based on the hypothesis that passive current density is governed by the transport of various defects (vacancies and interstitials) through the passive film. The most important assumptions made in the Point Defect Model are:

- Electric field strength is independent of film thickness. This assumption has been verified by experimental evidence, as the potential drop across the passive film was found to be linearly changed with passive film thickness.³²
- Passive film/solution interface potential is linearly related to pH and applied potential.

To ease further discussion of this model, a brief introduction on point defects is given below. A point defect can be defined as “a lattice site which contains an atom, ion or molecule which would not be present on that site in a perfectly stoichiometric material”.¹²⁸ In nature, any real crystals above absolute zero degree (0 K) contain defects. A point defect can be either a vacancy site or an interstitial site in a crystal structure. The two most common types of point defect are so-called Schottky and Frenkel defects, as demonstrated in Figure 50. It can be seen that the Schottky defect contains a pair of

cation and anion vacancies, while Frenkel defect is made of a cationic interstitial ion accompanied by a corresponding cation vacancy. Some characteristics of point defects related to the Point Defect Model are listed below.

- Interstitial ions exist in significant amount only when the size of the cation is much smaller than the anion.
- Ions situated at normal sites are electronically neutral; however, vacancies are negatively or positively charged to balance the surrounding ions.
- For a Schottky defect, a cation vacancy must be accompanied by certain numbers of anion vacancy to maintain overall electro-neutrality of the crystal.

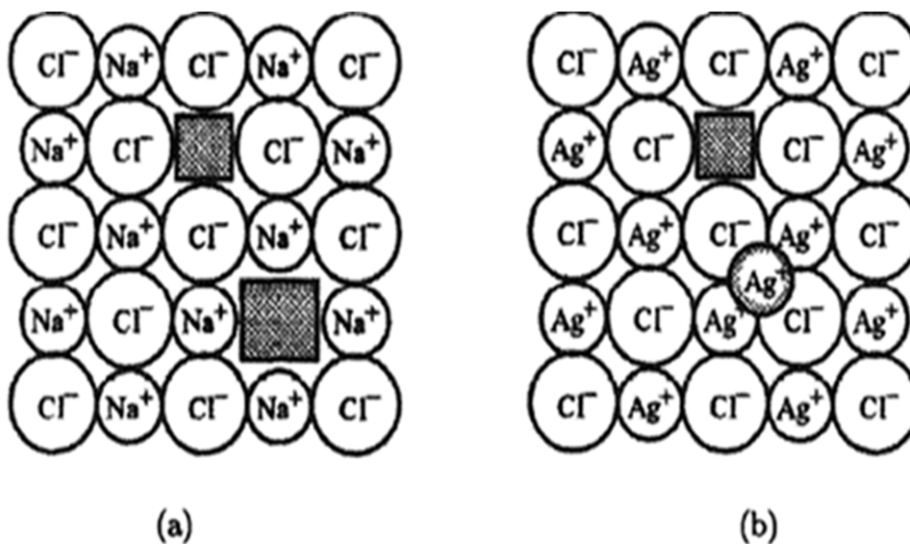


Figure 51. Original point defect model for carbon steel.³⁸ Fe: Fe atom on a metal lattice site; Fe_{Fe}: Fe on Fe site in the oxide; Fe_i^{x+}: iron interstitial in the oxide layer; O_O: oxygen ion in the oxide; V_{Fe}^{x-}: Fe vacancy; V_O^{o-}: oxygen vacancy; Fe^{Γ+}: metallic species in solution; FeO_{x/2}: oxide barrier layer; FeCO₃: precipitated outer layer; k_i: reaction rate constant; BL: oxide barrier layer; OL: outer layer.

In this work, modifications were made to this model for proper coupling of the Point Defect Model with the localized corrosion model. The pseudo-passive film considered in this study is magnetite (FeO+Fe₂O₃) through which vacancies of Fe³⁺ and O²⁻ travels; however, interstitial defects are not taken into account. This is because the radius of Fe³⁺ in a crystal (about 0.785 nm) is not significantly smaller than that of O²⁻ (about 1.25nm).¹²⁹ It would require a significant amount of energy for Fe³⁺ to squeeze into the lattice structure formed by O²⁻. Hence, it was determined that the interstitial defects, would not contribute much to the electrical charge-carrying process. Further simplification was made by excluding the outer layer in the model, which is mainly composed of FeCO₃ in a carbon steel/CO₂ system. This is because the potential distribution in the solution (including that within FeCO₃ layer) can be obtained by solving the Laplace equation, which allows for direct determination of potential on the pseudo-passive surface. Therefore, potential gradient across FeCO₃ layer is not required in this particular model. Figure 52 shows schematic of the revised model proposed in this study.

(170) and (171);¹²⁸ however, electrons are not involved in these reactions and so the existence of these reactions would not affect the current traveling within the film.



It has been argued that Reactions (165), (167) and (168) are lattice conservative,²⁸ which means that these reactions would not lead to the movement of boundaries, but are dedicated to transfer of charge. Reactions (166) and (169), however, are considered to be responsible for pseudo-passive film growth and dissolution, respectively. This argument deserves further discussion. It can be seen that Reactions (165), (167) and (168) involve the generation of a species (Fe^{Fe} in reaction (165), V_{Fe}^{3-} in reaction (167) and O^O in reaction (168)) at the expense of consumption of another species (V_{Fe}^{3-} in reaction (165), Fe^{Fe} in reaction (167) and V_O^{2+} in reaction (168)). It can be imagined that consumption/loss of the species on the boundaries of pseudo-passive film could lead to neighboring ions with a coordination number only one less than that in the bulk; therefore, the site of consumption can be viewed as a vacancy site, that will be replenished by the upcoming ions, while site of generation will be occupied by upcoming vacancies. Hence, at the steady state, boundaries will be maintained due to continuous consumption/supplement of ions or vacancies on the boundaries. As to Reaction (166), a cationic ion (Fe^{Fe}) and a vacancy (V_O^{2+}) are generated for every one iron atom in the base metal. In other words, this reaction generates new pseudo-passive film without consuming itself. Therefore, this reaction would lead to pseudo-passive film growth.

Details are given below for equation derivation of pseudo-passive current density based on the model presented in Figure 52.

At steady state, electron fluxes can be expressed in terms of fluxes of vacancies for Reactions (165) through (168), respectively. No vacancies are involved in reaction (169); therefore, electron flux is expressed in terms of H^+ concentration.

For Reaction (165):

$$J_e = -3J_{V_{Fe}^{3-}} \quad (172)$$

For Reaction (166):

$$J_e = 2J_{V_O^{2+}} \quad (173)$$

For Reaction (167):

$$J_e = J_{V_{Fe}^{3-}} \quad (174)$$

For Reaction (168):

$$J_e = 0 \quad (175)$$

For Reaction (169):

$$J_e = k_s c_{H^+}^n \quad (176)$$

Total electron flux is gained by summing up electron fluxes in all reactions:

$$J_e = \sum_{i=1}^n J_{e,i} = [2J_{V_O^{2+}} - 2J_{V_{Fe}^{3-}} + k_s c_{H^+}^n] \quad (177)$$

Current density is related to electron flux as:

$$i_{ss} = F \cdot (-nJ_e) = F \cdot [-2J_{V_O^{2+}} + 2J_{V_{Fe}^{3-}} - k_s c_{H^+}^n] \quad (178)$$

It was argued that Reactions (166) and (169) are responsible for pseudo-passive film growth and dissolution, respectively. At the steady state, film growth rate equals film dissolution rate.

Film growth rate is given by:

$$\frac{dm_{Fe}}{dt} = -\frac{2}{3}J_{V_0^{2+}} \quad (179)$$

Film dissolution rate is given by:

$$\frac{dFeO_{3/2}}{dt} = k_s c_{H^+}^n \quad (180)$$

At the steady state,

$$-\frac{2}{3}J_{V_0^{2+}} = k_s c_{H^+}^n \quad (181)$$

Equation (181) suggests that pseudo-passive film dissolution kinetics is directly related to anion flux at the steady state.

It should be noted that, for electrochemical reactions, the fluxes of anions and cations are not necessarily balanced. This is because, besides cations and anions, electrons are also involved in the transport. Therefore, it is the total fluxes of cations, anions and electrons that are conserved. This can be demonstrated by combining Equations (177) and (181), which gives:

$$J_e + 2J_{V_{Fe}^{3-}} - \frac{4}{3}J_{V_0^{2+}} = 0 \quad (182)$$

Substitute Equation (181) into (178), yields:

$$i_{ss} = F \cdot \left(2J_{V_{Fe}^{3-}} - 2\frac{2}{3}J_{V_0^{2+}} \right) \quad (183)$$

or

$$i_{ss} = 2F \cdot (J_{V_{Fe}^{3-}} + k_5 c_{H^+}^n) \quad (184)$$

Equation (183) indicates that the pseudo-passive current density is attributed to the movement of both cations and anions. Equation (184) suggests that the pseudo-passive current density is a result of competition between cation flux and passive film dissolution. Because anion flux is at the same rate of film dissolution (Equation (181)), it can be readily deduced that cation movement must be dominant in the transport process to maintain a steady pseudo-passive film.

Flux of Fe^{3+} vacancy can be calculated by considering Reaction (167) which is the only reaction where Fe^{3+} vacancy is involved on the pseudo-passive film/solution boundary. The total flux of Fe^{3+} vacancy at steady state can be calculated as:

$$J_{V_{Fe}^{3-}}(x=0) = J_{V_{Fe}^{3-}}(x=L) = k_3 \quad (185)$$

Substituting Equation (185) into (184), gives:

$$i_{ss} = 2F \cdot (k_3 + k_5 c_{H^+}^n) \quad (186)$$

The rate constant of an electrochemical reaction is given by:²⁸

$$k = k^0 e^{\frac{\alpha n F \phi}{RT}} \quad (187)$$

Apply Equation (187) to reactions (167) and (169), yield:

$$k_3 = k_3^{0'} e^{\frac{-\alpha_3 F \phi_{f/s}}{RT}} \quad (188)$$

$$k_5 = k_5^{0'} e^{\frac{-\alpha_5 F \phi_{f/s}}{RT}} \quad (189)$$

Let $\gamma = \frac{F}{RT}$, Equations (188) and (189) can be simplified as:

$$k_3 = k_3^{0'} e^{-\alpha_3 \gamma \phi_{f/s}} \quad (190)$$

$$k_5 = k_5^{0'} e^{-\alpha_5 \gamma \phi_{f/s}} \quad (191)$$

Assuming that the potential at pseudo-passive film/solution interface is linearly related to pH and metal potential (temperature has been found to be a minor factor):²⁸

$$\phi_{f/s} = \phi_{f/s}^0 + xV + ypH \quad (192)$$

Substituting Equation (192) into Equations (190) and (191), yields:

$$k_3 = k_3^0 e^{-\alpha_3 \gamma (xV + ypH)} \quad (193)$$

$$k_5 = k_5^0 e^{-\alpha_5 \gamma (xV + ypH)} \quad (194)$$

Where

$$k_3^0 = k_3^{0'} e^{-\alpha_3 \gamma \phi_{f/s}^0} \quad (195)$$

$$k_5^0 = k_5^{0'} e^{-\alpha_5 \gamma \phi_{f/s}^0} \quad (196)$$

Substituting Equation (193) and (194) into Equation (186), the pseudo-passive current density can be calculated as:

$$i_{ss} = 2F \cdot \left(k_3^0 e^{-\alpha_3 \gamma (xV + ypH)} + k_5^0 e^{-\alpha_5 \gamma (xV + ypH)} c_{H^+}^n \right) \quad (197)$$

The previous work performed by Macdonald *et al.* has shown that:^{38,130}

$$n = 0.5; \alpha_3 = 0.95; \alpha_5 = 0.55;$$

$$k_3^0 = 1 \times 10^{-4} \text{ mol/m}^2 \cdot \text{s}, k_5^0 = 1 \times 10^{-8} \text{ mol/m}^2 \cdot \text{s}$$

The only parameters to be determined are x and y.

By incorporating Equation (197) into the localized corrosion model and by adjusting the values of x and y, the model is calibrated against the measured galvanic current density values obtained in an artificial pit test,¹⁰⁵ which yields x=-0.01 and y=0.01. The equation for pseudo-passive current density is then given by:

$$i_{ss} = 2F \cdot \left\{ \begin{array}{l} 10^{-4} \exp \left[\frac{-0.95(-0.04V + 0.014pH)F}{RT} \right] \\ + 10^{-8} \exp \left[\frac{-0.55(-0.04V + 0.014pH)F}{RT} \right] c_{H^+}^n \end{array} \right\} \quad (198)$$

It can be shown that the second term in the bracket of RHS of Equation (198) is negligible compared to the first term; therefore, the final equation for pseudo-passive current is:

$$i_{ss} = 2F \cdot 10^{-4} \exp \left[\frac{-0.95(-0.04V + 0.014pH)F}{RT} \right] \quad (199)$$

Nomenclature

Fe: Fe atom on a metal lattice site; Fe_{Fe}: Fe on Fe site in the oxide; O_O: oxygen ion in the oxide; V_{Fe}³⁻: Fe vacancy; V_O²⁺: oxygen vacancy; Fe²⁺: metallic species in solution; FeO_{3/2}: oxide barrier layer; k_i: reaction rate constant; J_{V_O²⁺}, J_{V_{Fe}³⁻}, J_e: fluxes of oxygen ion vacancy, Fe vacancy and electron, respectively; i_{ss}: pseudo-passive current density; k₃, k₅: rate constants of reaction (167) and (169), respectively; k₃^{0'}, k₃⁰, k₅^{0'}, k₅⁰: standard rate constant for reactions (167) and (169), respectively; α₃, α₅: transfer coefficients of reactions (167) and (169); n: reaction order of reaction (169) in terms of H⁺; **V: potential**; F: Faraday constant; R: universal gas constant; T: Kelvin temperature; t: time; **x, y: parameters to be determined.**

APPENDIX 6: OPEN SOURCE MODEL OF UNIFORM CO₂/H₂S CORROSION

A6.1 Introduction

Carbon steel is the most commonly used engineering structural material in the oil and gas industry. In such environments, various aggressive species, such as CO₂, H₂S and organic acids tend to attack pipelines made from carbon steel. In the past few decades, uniform corrosion of carbon steel in oil and gas pipelines has been extensively studied, leading to sizable publications targeting many key aspects of uniform corrosion. Although not completely understood, most steps associated with CO₂ corrosion mechanisms are now believed to be clear. H₂S corrosion is still subject to ongoing investigation, but initial study has shed some light on the understanding of uniform corrosion mechanisms.¹³² With information available from the open literature, it is now possible to build a mechanistic model to predict uniform corrosion rates in order to assist with the understanding of the corrosion process. In fact, a number of models for CO₂ corrosion in wells and pipelines have been developed in recent years, as summarized by Nyborg.³ However, the availability of most of these models to the public is largely limited due to their proprietary nature. In addition, a large scatter in the prediction is not uncommon resulting from different theories, assumptions and modeling strategies. Due to the lack of transparency of the code behind the models, it is difficult for users to make a sound judgment as to which one is more reliable. It can be imagined that, as the corrosion process becomes increasingly complex, larger discrepancies may be expected from various models. This section of work is aimed at providing the corrosion community with a free mechanistic model for internal corrosion prediction of carbon steel pipelines

particularly related to oil and gas industry. Strongly rooted in theories, this model can offer trustworthy predictions for a wide range of conditions, as will be shown in the following sections. The model, named FREECORP, was developed exclusively based on public information. All the information related to the model, including theories, assumptions and limitations, is available to the users and can be accessed through <http://www.corrosioncenter.ohiou.edu/freecorp>. In addition, the source code is open and shared. With open source code, the model can be improved and expanded by adding new modules or modifying existing modules. By doing so, model capability can be extended to accommodate a wider range of environments.

As already mentioned in a previous publications, the motivation of offering this model to the corrosion community is:¹⁶

- To elevate the level of understanding and the prediction capability of mild steel corrosion as related to the oil and gas industry.
- To ensure that the best available science and technology is available to corrosion engineers, and implemented using a transparent approach that is open for further development and improvement.
- To increase the level of involvement of the broader corrosion community in developing better and more flexible tools suited for their intended purposes, an approach which will hopefully be mimicked in the future in other fields of corrosion.
- To fulfill one of the key missions of the Institute for Corrosion and Multiphase Technology and Ohio University as a public institution, which is to educate the wider professional community and extend its reach beyond the pool of the current research

sponsors in order to enable more effective dissemination of the already published knowledge and technology.

This model is able to predict a uniform corrosion rate for carbon steel under attack by CO_2 , H_2S , HAc and/or O_2 . To facilitate the understanding of corrosion mechanisms, additional information is given apart from corrosion rate. For instance, the contribution of each corrosive species to the overall corrosion rate is quantified as a percentile. An Evans diagram is provided for $\text{CO}_2/\text{HAc}/\text{O}_2$ corrosion where polarization curves are shown for individual electrochemical reactions as well as total anodic and cathodic reactions. For H_2S corrosion, the H_2S concentration profile across the mackinawite layers and the liquid boundary layer is illustrated in place of an Evans diagram. It was determined that the H_2S concentration profile would be more informative and useful, since the H_2S corrosion model is based on the assumption of mass transfer control. The effect of FeCO_3 and FeS is simulated using empirical correlations in order to achieve a better prediction.

In the following sections, the main theories related to uniform corrosion caused by CO_2 , H_2S , HAc and/or O_2 are briefly reviewed, followed by a description of the implementation of these theories into the model. Model verification and parametric study are then presented. In the final section, limitations of the current version of the model are described and directions for future development are pointed out.

A6.2 Theories of the Model

Although many publications are referenced during model development, 3 key papers are used as the theoretical basis of this model. These are: the paper by Nešić, Postelthwaite and Olsen for CO_2 corrosion¹³¹, that by George, Nešić and de Waard for

HAc corrosion⁹⁶ and that by Sun and Nešić for H₂S corrosion¹³². CO₂ and HAc corrosion are electrochemical processes involving water chemistry, electrochemistry and mass transport. Those effects have been previously discussed in Chapter 4 above and will not be replicated here.

Compared to CO₂ corrosion, H₂S corrosion is much less understood. Even though abundant experimental data for H₂S corrosion have been presented in the open literature, discrepancies and contradictions are often seen in the literature. At present, the topic of H₂S corrosion mechanism is still subject to much debate. From the experimental results, H₂S corrosion seems to manifest itself as a fast surface reaction (either chemical or electrochemical) followed by massive FeS layer growth.¹³² An FeS layer is always present on a corroding steel surface in an H₂S-containing environment, causing substantial reduction of the general corrosion rate. Although the current level of knowledge does not grant a solid mechanism that is consistent with all experimental observations and agreed upon by all researchers, this model employs a mechanism proposed by Sun *et al.*,¹³² that is considered to be plausible and supported by many experimental results. According to this theory, H₂S is initially absorbed onto the steel surface and immediately reacts with iron to form a very thin ($\ll 1 \mu\text{m}$), dense and protective non-stoichiometric iron sulfide film – mackinawite. Due to its compactness, this film acts as a solid-state diffusion barrier for species involved in the corrosion process and leads to a significant and rapid reduction of the corrosion rate. Although slow, diffusion of the corrosive species through this mackinawite film does not completely cease, and the continuing corrosion at the steel surface continues to generate

more mackinawite. As this process proceeds, the internal stress in the mackinawite film is built up due to epitaxial stresses and the Pilling-Bedford ratio (large volume ratio of the mackinawite to iron). These stresses lead to microcracking and eventually delamination of the mackinawite film. A cyclic process of growth, cracking and delaminating of mackinawite eventually leads to the formation of an outer mackinawite layer that is thicker, more porous and less protective.

Considering the fact that the inner and outer FeS layers are always present in H₂S corrosion, Sun *et al.* assume that H₂S corrosion is under mass transfer control.¹³² Corrosion rate is limited by the mass transfer of corrosive species, such as H₂S, CO₂, H⁺, HAc, etc., through the FeS layers on steel surface.

In reality, H₂S corrosion can be complicated by a number of factors. For instance, given enough time, the mackinawite film might transform into other forms of sulfides such as pyrrhotite. In addition, pyrrhotite might precipitate from the solution to form an additional solid layer and further increase mass transfer resistance. In the presence of high-concentration H₂S and oxygen, elemental sulfur might form in the pipelines and induce localized corrosion. These effects are not included in the present version of the model.¹³⁸

A6.3 Mathematical Model

The FREECORP model is a simplified version of the model presented in Chapter 4 for uniform corrosion (MULTICORP V5). The CO₂/HAc corrosion model is a simple electrochemical model in which corrosion rate is determined based on the fact that the total anodic current is balanced by the total cathodic current. The H₂S corrosion rate is

calculated based on the assumption of mass transfer limiting, which implies that corrosion rate is determined by the diffusion rates of corrosive species. Unlike MULTICORP, where mass transfer of species is obtained by solving complex partial differential equations, in FREECORP it is calculated by the concept of a mass transfer coefficient involving a simple empirical correlation. For CO₂ corrosion, pure charge transfer and mass transfer/chemical reaction-limiting current density are calculated for each cathodic reaction independently, which are then coupled together to give an integrated scheme of the electrochemical reaction kinetics. This section details the mathematical description of the model.

A6.3.1 CO₂/HAc Corrosion

CO₂/HAc corrosion rate is calculated through the determination of individual electrochemical reaction rates involved in the corrosion process. The electrochemical reactions that are taken into consideration in this model include: oxidation of iron, reduction of hydrogen ion, direct reduction of carbonic acid, direct reduction of acetic acid, reduction of water and reduction of oxygen.

A6.3.1.1 Anodic Reaction

Oxidation of iron is the only anodic reaction considered in this model.



Reaction (78) is a charge transfer control process within the potential range of interest. The current density of this reaction can be calculated using the Tafel equation and is previously given in Table 1. Table 1 presents equations used calculate the charge

transfer current density of major electrochemical reactions involved in CO₂/HAc corrosion. In the following text of section 5.3.1, unless otherwise stated, the charge transfer current density calculation refers to the corresponding equation shown in Table 1.

A6.3.1.2 Cathodic Reactions

Reduction of hydrogen ion

H⁺ reduction is the primary cathodic reaction in a CO₂ system with pH less than 5.



The current density for reduction of hydrogen ion consists of two components: charge transfer limiting and mass transfer limiting. Total current density is calculated using a harmonic mean:

$$\frac{1}{i_{H^+}} = \frac{1}{i_{a,H^+}} + \frac{1}{i_{lim,H^+}^d} \quad (200)$$

Where i_{H^+} : total current density of H⁺ reduction, A/m²; i_{a,H^+} : charge transfer current density of H⁺ reduction, A/m²; i_{lim,H^+}^d : mass transfer limiting current density of H⁺ reduction, A/m².

The mass transfer limiting current density is related to bulk concentration of H⁺ as:

$$i_{lim,H^+}^d = k_{m,H^+} F c_{H^+} \eta_{FeCO_3} \eta_{FeS} \quad (201)$$

Where k_{m,H^+} : H⁺ mass transfer coefficient, m/s; c_{H^+} : bulk concentration of H⁺, mol/m³;

$\eta_{FeCO_3}, \eta_{FeS}$: scale factor related to iron carbonate and iron sulfide film, respectively.

Mass transfer coefficient of H^+ can be calculated using the published correlation for straight pipes:¹³⁶

$$Sh = \frac{k_{m,H^+} l}{D_{H^+}} = 0.0165 Re^{0.86} Sc^{0.33} \quad (202)$$

Where Sh : Sherwood number; l : pipe diameter, m; D_{H^+} : diffusion coefficient of hydrogen ion, m^2/s ; Re : Reynolds number = $\rho ul / \mu$; Sc : Schmidt number = $\mu / \rho D$.

In a dilute solution, the diffusion coefficient of species relates to temperature and solution viscosity, which can be calculated using the Stokes-Einstein equation:

$$D_{H^+} = D_{ref,H^+} \times \frac{T_K}{T_{ref}} \times \frac{\mu_{ref}}{\mu} \quad (203)$$

Where D_{ref,H^+} : reference diffusion coefficient of H^+ , $9.31 \times 10^{-9} m^2/s$; T_{ref} : reference temperature, 293.16 K; μ_{ref} : reference liquid viscosity, 1.002 kg/(m.s).

Equation (202) and (203) are used to calculate the mass transfer coefficients of all involved species with corresponding reference diffusion coefficients.

Water density and viscosity required in the Reynolds number calculation are a function of temperature and are respectively given by:¹³⁷

$$\rho_{H_2O} = (753.596 + 1.87748 \times T_K - 0.003564 \times T_K^2) \quad (204)$$

$$\mu_{H_2O} = \mu_{ref} \times 10^{\frac{1.3272 \times (20 - T_C) - 0.001053 \times (20 - T_C)^2}{T_C + 105}} \quad (205)$$

Where μ_{ref} : reference water viscosity, 1.002 kg/(m.s); T_C , T_K : system temperature in °C and Kelvin respectively.

Direct reduction of carbonic acid

At the steel surface, carbonic acid can be directly reduced.



The kinetics of this reaction could be limited by charge transfer or, more commonly, by a slow hydration rate of CO₂, as discussed in 4.3.1. The total current density is calculated by the harmonic mean of charge transfer and chemical reaction-limiting current densities:

$$\frac{1}{i_{H_2CO_3}} = \frac{1}{i_{a,H_2CO_3}} + \frac{1}{i_{lim,H_2CO_3}^r} \quad (206)$$

Where $i_{H_2CO_3}$, i_{a,H_2CO_3} and $i_{lim,H_2CO_3}^r$ are total current density, charge transfer current density and chemical reaction-limiting current density in A/m², respectively.

The chemical reaction-limiting current density is given by Nešić *et al.* as:¹³¹

$$i_{lim,H_2CO_3}^r = Fc_{CO_2} \left(D_{H_2CO_3} K_{hyd} k_{hyd}^f \right)^{0.5} f \eta_{FeCO_3} \eta_{FeS} \quad (207)$$

Where c_{CO_2} : concentration of CO₂ in bulk solution, mol/m³; $D_{H_2CO_3}$: diffusion coefficient of H₂CO₃ in water, m²/s; K_{hyd} : equilibrium constant for CO₂ hydration reaction; k_{hyd}^d : forward reaction rate constant for CO₂ hydration reaction; f : flow factor affecting CO₂ hydration which accounts for mass transfer of H₂CO₃.

CO₂ concentration can be obtained from partial pressure of CO₂ based on Henry's law:

$$c_{CO_2} = K_{CO_2}^d P_{CO_2} \quad (208)$$

Where $K_{CO_2}^d$: Henry's constant; P_{CO_2} : partial pressure of CO₂, bar.

Henry's constant is a function of temperature and given by:¹³³

$$K_{CO_2}^d = \frac{14.5}{1.00258} \times 10^{-(2.27+5.65 \times 10^{-3} T_f - 8.06 \times 10^{-6} T_f^2 + 0.075 \times t)} \quad (209)$$

The forward reaction rate constant for CO₂ hydration is a function of temperature and given by:¹³⁴

$$k_{hyd}^f = 10^{329.85 - 110.541 \log T_K - \frac{17265.4}{T_K}} \quad (210)$$

Flow factor f is given by:¹³⁵

$$f = \frac{1 + e^{-2\delta_m / \delta_r}}{1 - e^{-2\delta_m / \delta_r}} \quad (211)$$

Where δ_m and δ_r are defined as mass transfer and reaction layer thickness, respectively, which can be calculated as:¹³⁵

$$\delta_m = \frac{D_{H_2CO_3}}{k_{m,H_2CO_3}} \quad (212)$$

$$\delta_r = \sqrt{\frac{D_{H_2CO_3} K_{hyd}}{k_{hyd}^f}} \quad (213)$$

Where k_{m,H_2CO_3} is the mass transfer coefficient of H₂CO₃ in m/s, which can be obtained using Equations (202) and (203).

It has been argued that flow factor becomes significant only when thickness of the mass transfer boundary layer is of the same order as the reaction layer.

Direct reduction of HAC

Acetic acid takes part in the corrosion process in two main ways. Firstly, by dissociation, it can provide additional sources of H⁺ to be reduced. Secondly, it can be directly reduced on the steel surface and further increase the corrosion rate.



It has been shown that the current density for direct reduction of HAc could be limited either by charge transfer or mass transfer.⁹⁶ The total current density is given by:

$$\frac{1}{i_{HAc}} = \frac{1}{i_{a,HAc}} + \frac{1}{i_{lim,HAc}^d} \quad (81)$$

Where i_{HAc} , $i_{a,HAc}$ and $i_{lim,HAc}^d$ are total current density, charge transfer current density and mass transfer limiting current density of this reaction in A/m², respectively.

The mass transfer limiting current density of this reaction is given by:

$$i_{lim,HAc}^d = k_{m,HAc} F c_{HAc} \eta_{FeCO_3} \eta_{FeS} \quad (214)$$

Where $k_{m,HAc}$: mass transfer coefficient of HAc, m/s; c_{HAc} : bulk concentration of acetic acid, mol/m³.

Oxygen reduction

Although oxygen is not a common corrosive species in oil and gas pipeline systems, it could invade the system through inappropriate operation or insufficient de-oxidation of chemical solutions injected into the system. In order to take into account oxygen contamination, oxygen reduction is built in the model as well.

Like H⁺ reduction and HAc reduction, the current density of oxygen reduction could be limited by either charge transfer or mass transfer. The current density is therefore calculated as:

$$\frac{1}{i_{O_2}} = \frac{1}{i_{a,O_2}} + \frac{1}{i_{lim,O_2}^d} \quad (215)$$

Where i_{O_2} : total current density of oxygen reduction, A/m²; i_{a,O_2} : charge transfer current density of oxygen reduction, A/m²; i_{lim,O_2}^d : mass transfer limiting current density of oxygen reduction, A/m².

Charge transfer current density is given by Tafel equation:

$$i_{a,O_2} = i_{0,O_2} \times 10^{\frac{E_{0,O_2} - E}{b_{O_2}}} \quad (216)$$

Where i_{0,O_2} : current density of oxygen reduction at a reference point, 0.06A/m²; E_{0,O_2} : potential of oxygen reduction at a reference point, 0.5V; b_{O_2} : Tafel slope of oxygen reduction.

The reference current density of oxygen reduction is a function of temperature:¹³¹

$$i_{0,O_2} = i_{0ref,O_2} \times e^{\frac{-\Delta H_{O_2}}{R} \left(\frac{1}{T_K} - \frac{1}{T_{ref}} \right)} \quad (217)$$

Where i_{0ref,O_2} : current density of oxygen reduction at a reference temperature, A/m²; T_{ref} : reference temperature, 298.16K; ΔH_{O_2} : activation energy of oxygen reduction, 10k J/mol.

Mass transfer-limiting current density is given by:¹³¹

$$i_{lim,O_2}^d = 4k_{m,O_2} F c_{O_2} \eta_{FeCO_3} \eta_{FeS} \quad (218)$$

Where k_{m,O_2} : mass transfer coefficient of oxygen, m/s; c_{O_2} : bulk concentration of oxygen, mol/m³.

It should be noted that, due to the high reversible potential of oxygen reduction, this reaction is almost always controlled by mass transfer in the potential range of interest.

Water reduction

Water reduction normally contributes little to overall corrosion rate; however, it can become important when the solution pH is sufficiently high or when a certain level of negative potential is applied on the metal surface.¹³ It is also essential to include this reaction in the model in order to give a complete description of the polarization curves, as water reduction becomes dominant in cathodic polarization curves when the potential is sufficiently low. Due to the fact that water supply is unlimited everywhere in the solution, water reduction would not be limited by mass transfer. Therefore, water reduction is always assumed to be under charge transfer control. The current density of this reaction is given by Tafel equation:

$$i_{H_2O} = i_{0,H_2O} \times 10^{\frac{E_{0,H_2O} - E}{b_{H_2O}}} \quad (219)$$

Where i_{H_2O} : current density of water reduction, A/m²; i_{0,H_2O} : reference current density of water reduction, A/m²; E_{0,H_2O} : reference potential of water reduction, V; b_{H_2O} : Tafel slope of water reduction.

The reference current density of water reduction can be calculated from:

$$i_{0,H_2O} = i_{0ref,H_2O} \times e^{\frac{-\Delta H_{H_2O}}{R} \left(\frac{1}{T_K} - \frac{1}{T_{ref}} \right)} \quad (220)$$

Where i_{0ref,H_2O} : reference exchange current density of water reduction, $10^{-4.45}$ A/m²;
 ΔH_{H_2O} : activation energy of water reduction, 30kJ/mol; T_{ref} : reference temperature,
 298.16K.

It has been argued that reduction of water is thermodynamically equivalent to H⁺ reduction,¹³¹ therefore the reference potential and Tafel slope can be calculated in the same way as those for H⁺ reduction, as shown in Table 1.

A6.3.1.3 Determination of CO₂/HAc Corrosion Rate

The CO₂/HAc corrosion rate is determined based on charge balance on the steel surface. By equating total anodic current density with total cathodic current density, the unknown corrosion potential can be solved.

$$\sum_1^{na} i_a = \sum_1^{nc} i_c \quad (221)$$

Where i_a , i_c : anodic and cathodic current density, respectively, A/m²; na, nc : total numbers of anodic and cathodic reactions, respectively.

Once corrosion potential is found, current density of individual electrochemical reactions involved in the corrosion process can be readily calculated. The corrosion rate can then be determined based on the current density of iron oxidation or the total current density of cathodic reactions.

$$\begin{aligned} CR &= \frac{i_a M_{w,Fe}}{\rho_{Fe} nF} \times 1000 \times 3600 \times 24 \times 365 \\ &= 1.159 i_a \end{aligned} \quad (222)$$

Where CR: corrosion rate, mm/yr; i_a : total anodic current density, A/m²; $M_{w,Fe}$: atomic mass of iron, 55.56g/mol; ρ_{Fe} : density of iron, 7800g/m³; n: number of moles of electrons involved in iron oxidation, 2 mole/mol.

A6.3.2 H₂S Corrosion

Due to the presence of three layers on steel surface, i.e., a very thin but dense mackinawite film on steel surface, a porous and often thick outer mackinawite layer and a liquid boundary layer, H₂S corrosion is considered to be under mass transfer control. Hence, an H₂S corrosion rate can be obtained from the total fluxes of the corrosive species. The flux of individual corrosive species (H₂S, H⁺, H₂CO₃, HAc, etc.) across three layers is a function of the mass transfer coefficient and the concentration gradient within the layer. At steady state, a unique flux is experienced throughout the mass transfer layers. By equating fluxes in different layers, intermediate concentrations can be eliminated, which finally leads to an implicit expression for flux related only to the mass transfer coefficient and the bulk and surface concentrations.

Take H₂S as an example. The flux of H₂S due to diffusion through the liquid boundary layer can be calculated as:¹³²

$$Flux_{H_2S} = k_{m,H_2S} (c_{b,H_2S} - c_{o,H_2S}) \quad (223)$$

The flux of H₂S due to diffusion through the outer mackinawite layer is given by:¹³²

$$Flux_{H_2S} = \frac{D_{H_2S} \varepsilon \psi}{\delta_{OS}} (c_{o,H_2S} - c_{i,H_2S}) \quad (224)$$

The flux of H₂S due to solid state diffusion through the inner mackinawite film is given by:¹³²

$$Flux_{H_2S} = A_{H_2S} e^{\frac{B_{H_2S}}{RT_K}} \ln \left(\frac{c_{i,H_2S}}{c_{s,H_2S}} \right) \quad (225)$$

Where $Flux_{H_2S}$: flux of H₂S, mol/(m²s); k_{m,H_2S} : mass transfer coefficient of H₂S in liquid boundary layer, calculated using equation, m/s; D_{H_2S} : diffusion coefficient of H₂S in water, calculated using the Stokes-Einstein correlation (Equation (203)) with reference diffusion coefficient (D_{ref,H_2S}) of H₂S of 1.3x10⁻¹⁰ m²/s at $T_{ref} = 298.16$ K and $\mu_{ref} = 1.002$ kg/(m.s); ε, ψ : empirically determined porosity and tortuosity of outer mackinawite scale, $\varepsilon = 0.9$ and $\psi = 0.003$ respectively; δ_{os} : thickness of the outer scale, m; $c_{b,H_2S}, c_{o,H_2S}, c_{i,H_2S}, c_{s,H_2S}$: concentration of H₂S in bulk solution, at outer scale/solution interface, at inner film/outer scale interface and at steel surface, respectively, mol/m³; A_{H_2S}, B_{H_2S} : Arrhenius constants, $A_{H_2S} = 1.30 \times 10^{-4}$ mol/(m²s) and $B_{H_2S} = 15.5$ kJ/mol.

Considering steady-state, where the flux of species is constant across these layers, by equating Equations (223) through (225) to eliminate intermediate concentration, c_{o,H_2S} and c_{i,H_2S} , the following equation is obtained for the flux of H₂S:¹³²

$$Flux_{H_2S} = A_{H_2S} e^{\frac{B_{H_2S}}{RT_K}} \ln \frac{c_{b,H_2S} - Flux_{H_2S} \left(\frac{\delta_{os}}{D_{H_2S} \varepsilon \psi} + \frac{1}{k_{m,H_2S}} \right)}{c_{s,H_2S}} \quad (226)$$

Where c_{s,H_2S} is assumed to be 1.0x10⁻⁷ mol/m³.

The thickness of outer mackinawite layer can be calculated as:¹³²

$$\delta_{os} = \frac{\Delta m_{os}}{\rho_{FeS} A} \quad (227)$$

Where Δm_{os} : mass of outer mackinawite layer, kg; ρ_{FeS} : density of iron sulfide, kg/m³ and A: surface area of steel, m².

The mass of the outer mackinawite layer can be calculated based on the scale retention rate, which is related to the damage of mackinawite layer:¹³²

$$\Delta m_{os} = SRR \cdot M_{FeS} \cdot A \cdot \Delta t \quad (228)$$

Where SRR: scale retention rate, mol/(m²s); M_{FeS}: molar mass of iron sulfide, kg/mol; A: surface are of steel, m²; Δt : time span, s.

Experiments have shown that scale damage rate can be estimated by:¹³²

$$SRR = \frac{0.5 Flux_{H_2S}}{1 - \varepsilon} \quad (229)$$

Combine Equations (227), (228) and (229) yields:

$$\delta_{os} = \frac{0.5 Flux_{H_2S} M_{FeS} \Delta t}{\rho_{FeS} (1 - \varepsilon)} \quad (230)$$

Apparently, H₂S is not the only species that can cause corrosion. Other species such as H⁺, H₂CO₃, HAc etc., once they have penetrated through the inner makinawite film, will be able to react with steel and further increase the corrosion rate. Therefore, the contributions from other species have to be taken into consideration as well.

By analogy, the flux of other species can be determined in a similar fashion to the one shown for H₂S. The fluxes of H⁺, H₂CO₃ and HAc are respectively given by:¹³²

$$Flux_{H^+} = A_{H^+} e^{\frac{B_{H^+}}{RT_k}} \ln \frac{c_{b,H^+} - Flux_{H^+} \left(\frac{\delta_{OS}}{D_{H^+} \varepsilon \psi} + \frac{1}{k_{m,H^+}} \right)}{c_{s,H^+}} \quad (231)$$

$$Flux_{H_2CO_3} = A_{H_2CO_3} e^{\frac{B_{H_2CO_3}}{RT_k}} \ln \frac{c_{b,H_2CO_3} - Flux_{H_2CO_3} \left(\frac{\delta_{OS}}{D_{H_2CO_3} \varepsilon \psi} + \frac{1}{k_{m,H_2CO_3}} \right)}{c_{s,H_2CO_3}} \quad (232)$$

$$Flux_{HAc} = A_{HAc} e^{\frac{B_{HAc}}{RT_k}} \ln \frac{c_{b,HAc} - Flux_{HAc} \left(\frac{\delta_{OS}}{D_{HAc} \varepsilon \psi} + \frac{1}{k_{m,HAc}} \right)}{c_{s,HAc}} \quad (233)$$

Where $Flux_{H^+}$, $Flux_{H_2CO_3}$, $Flux_{HAc}$: fluxes of H^+ , H_2CO_3 , HAc ; A_{H^+} , B_{H^+} : Arrhenius constants for H^+ , $A_{H^+}=4.0 \times 10^{-7} \text{ mol}/(\text{m}^2\text{s})$ and $B_{H^+}=1.55 \times 10^4 \text{ J}/\text{mol}$; $A_{H_2CO_3}$, $B_{H_2CO_3}$: Arrhenius constants for H_2CO_3 , $A_{H_2CO_3}=2.0 \times 10^{-9} \text{ mol}/(\text{m}^2\text{s})$ and $B_{H_2CO_3}=1.55 \times 10^4 \text{ J}/\text{mol}$; A_{HAc} , B_{HAc} : Arrhenius constants for HAc , $A_{HAc}=2.0 \times 10^{-9} \text{ mol}/(\text{m}^2\text{s})$ and $B_{HAc}=1.55 \times 10^4 \text{ J}/\text{mol}$; c_{b,H^+} , c_{o,H^+} , c_{i,H^+} , c_{s,H^+} : concentrations of H^+ in bulk solution at outer scale/solution interface, at inner film/outer scale interface and at steel surface, respectively, mol/m^3 ; c_{b,H_2CO_3} , c_{o,H_2CO_3} , c_{i,H_2CO_3} , c_{s,H_2CO_3} : concentrations of H_2CO_3 in bulk solution at outer scale/solution interface, at inner film/outer scale interface and at steel surface, respectively, mol/m^3 ; $c_{b,HAc}$, $c_{o,HAc}$, $c_{i,HAc}$, $c_{s,HAc}$: concentrations of HAc in bulk solution at outer scale/solution interface, at inner film/outer scale interface and at steel surface, respectively, mol/m^3 ; D_{H^+} , $D_{H_2CO_3}$, D_{HAc} : diffusion coefficients of H^+ , H_2CO_3 and HAc in water, m^2/s ; k_{m,H^+} , k_{m,H_2CO_3} , $k_{m,HAc}$: mass transfer coefficients of H^+ , H_2CO_3 and HAc in water, m/s .

In the model, the surface concentrations of H₂S, H⁺ and HAc are assumed to be 1.0x10⁻⁷ mol/L, a value small enough that can be claimed to be a mass transfer control process, while H₂CO₃ surface concentration are calculated from:

$$c_{s,H_2CO_3} = \frac{Flux_{H_2CO_3}}{\left(D_{H_2CO_3} \varepsilon \psi K_{hyd} k_{hyd}^f\right)^{0.5}} \quad (234)$$

Once the flux of individual species is available, overall H₂S corrosion rate can then be readily calculated by summing up the fluxes of all present corrosive species.

$$CR_{H_2S} = Flux_{H_2S} + Flux_{H^+} + Flux_{H_2CO_3} + Flux_{HAc} \quad (235)$$

A6.3.3 Film Growth

Film growth is vital to any corrosion process. Once present, it often controls the corrosion rate. In this model, the effect of FeCO₃ and FeS layer are characterized by a scale factor, which is empirically determined as a function of supersaturation of FeCO₃ or H₂S concentration.

The scale factor related to FeCO₃ layer is calculated as:

$$\begin{aligned} \eta_{FeCO_3} &= \frac{1}{SS_{FeCO_3}^{0.7}} && \text{if } SS_{FeCO_3} > 1 \\ \eta_{FeCO_3} &= 1 && \text{if } SS_{FeCO_3} \leq 1 \end{aligned} \quad (236)$$

Where SS_{FeCO_3} is the supersaturation of FeCO₃.

Supersaturation of FeCO₃ is defined as:

$$SS_{FeCO_3} = \frac{c_{Fe^{2+}} \cdot c_{CO_3^{2-}}}{K_{SP}^{FeCO_3}} \quad (237)$$

Solubility limit of FeCO_3 is a function of temperature and ionic strength and given by:⁹⁹

$$K_{SP}^{\text{FeCO}_3} = \frac{10^{-10.13-0.0182T_c}}{0.0115 \cdot \text{ion}^{-0.6063}} \quad (238)$$

Where T_c : temperature, °C; ion : ionic strength of the solution.

The effect of iron sulfide film depends on the amounts of H_2S existing in the system, as shown below:

$$\eta_{\text{FeS}} = \frac{1}{1 + 0.05c_{\text{H}_2\text{S}}^{\text{ppm}}} \quad (239)$$

Where $c_{\text{H}_2\text{S}}^{\text{ppm}}$ is concentration of H_2S in gas phase in ppm.

A6.3.4 Determination of $\text{CO}_2/\text{H}_2\text{S}$ Dominant Process

When CO_2 and H_2S co-exist in the system, both CO_2 and H_2S corrosion rates are calculated based on their respective mechanisms, as described above. The mechanism that gives the higher corrosion rate is considered as the dominant mechanism.

A6.4 Implementation of the Model

This model is developed as an excel add-in to allow for easy access to embedded codes. All inputs and outputs are stored in excel sheets, which can be manipulated and saved in whichever way the user prefers. The source codes are written using the Object-Oriented Programming (OOP) approach where major functionality, such as anodic or cathodic reaction rates, corrosion rate calculation, etc., is encapsulated as an individual object, which can be separated from the graphic user interface (GUI) and utilized in other programs for special needs. This function is designed to provide the possibility to expand

the model into areas other than oil and gas industry where corrosion is a concern. With an object-oriented structure, more functions can be developed as individual objects and incorporated into the model for enhanced functionality without disturbing the main corrosion calculation process. For instance, a water chemistry model can be added as an object to obtain species concentrations in the solution.

It should be mentioned that similar functionality is not yet available for H₂S corrosion model in the current version of FREECORP software. Figure 53 schematically shows the structure of the model.

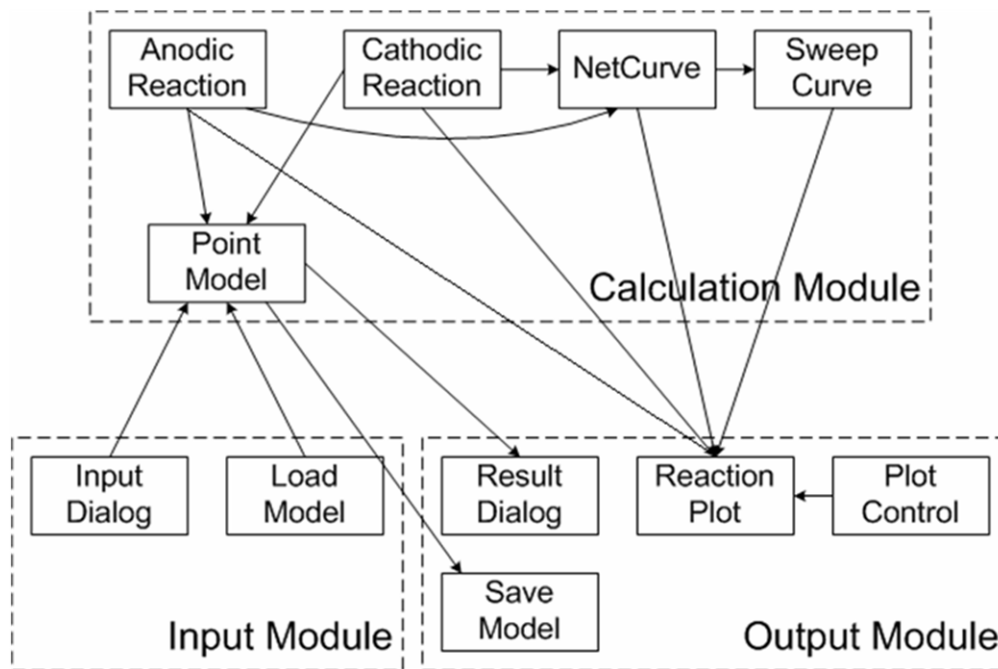


Figure 53. Structure of the FREECORP software.¹⁶

Compared to other corrosion prediction software packages, FREECORP has a few unique features. First of all, rooted from solid mechanisms, this model is capable to

quantifying the contributions of individual corrosive species. This feature allows users to easily identify the predominant corrosive species and better understand the corrosion mechanisms with the help of other information provided by the software. Two examples are given in Figure 54 and Figure 55 to illustrate the GUI showing the contributions of corrosive species for CO₂ and H₂S corrosion cases, respectively.

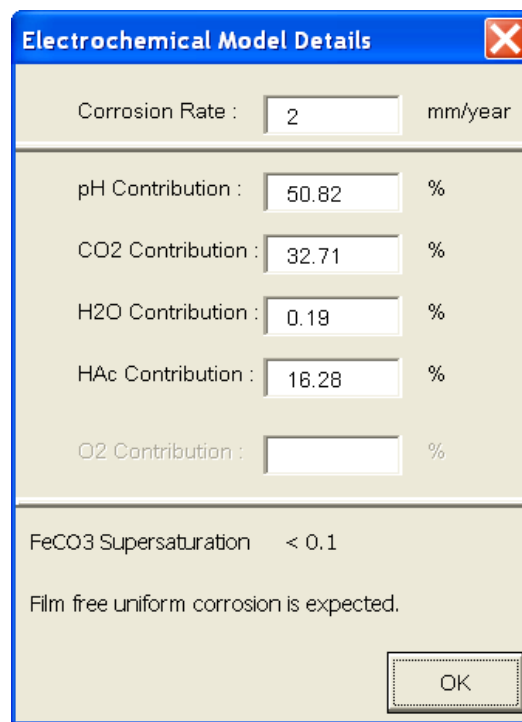


Figure 54. Screen shot for contributions of corrosive species in a CO₂ corrosion case. Simulation conditions: temperature 20°C, pipe diameter 0.1m, velocity 1m/s, CO₂ partial pressure 1bar, HAc 10ppm, pH 4.

Parameter	Value	Unit
Corrosion Rate	0.6	mm/year
H2S Contribution	1.72	%
pH Contribution	76.59	%
CO2 Contribution	14.13	%
HAc Contribution	7.56	%

Figure 55. Screen shot for contributions of corrosive species in a H₂S corrosion case. Simulation conditions: temperature 20°C, pipe diameter 0.1m, velocity 1m/s, CO₂ partial pressure 1bar, H₂S 10ppm, pH 4.

Corrosion mechanisms can be further investigated by visualizing the diagram associated with the dominant corrosion process. For CO₂/HAc corrosion, which is electrochemical in nature, polarization (E-i) curves are shown for each individual electrochemical reaction and total anodic and cathodic reactions. The potentiodynamic sweep curve is also shown on the same diagram. Each of the polarization curves can be freely turned on/off for enhanced visibility and customized presentation of the corrosion process. For H₂S corrosion, where mass transfer is a concern, FREECORP gives the concentration profile of H₂S across the mass transfer boundary layers, including inner makinawite film, outer porous makinawite layer and liquid phase diffusion boundary layer. Figure 56 and

Figure 57 demonstrate two examples of the main software interface in which an Evans diagram and an H₂S concentration profile are shown for CO₂ and H₂S corrosion, respectively.

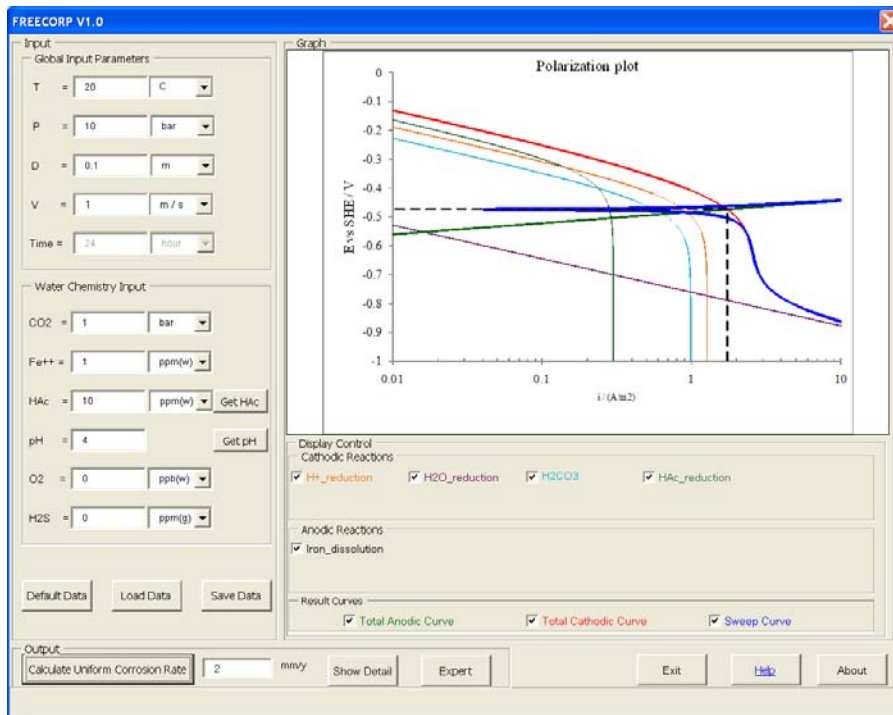


Figure 56. Screen shot for the user input/output window for CO₂ corrosion in FREECORP.

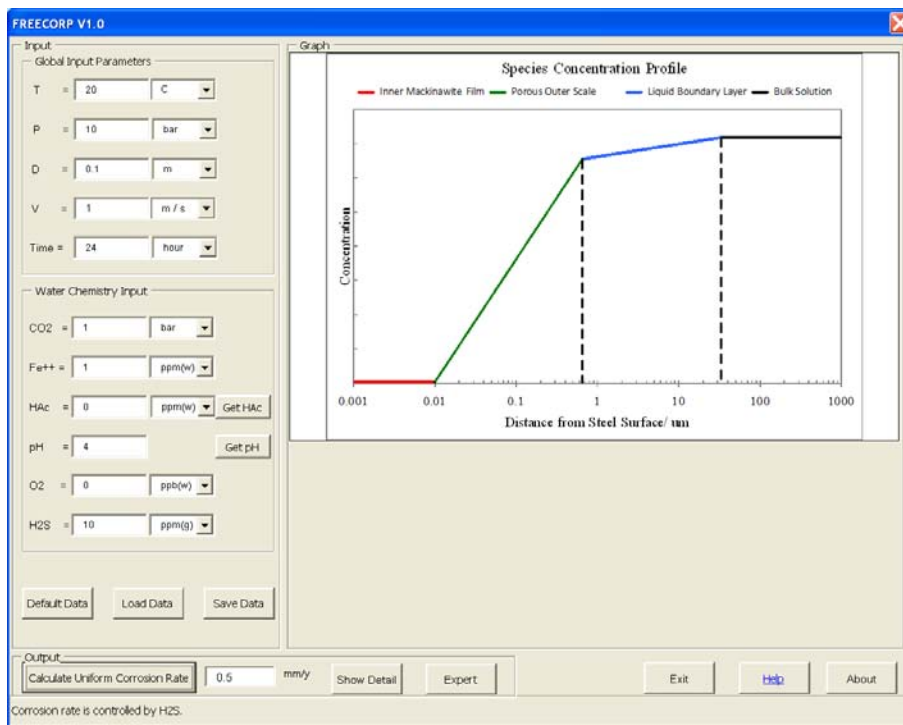


Figure 57. Screen shot for the user input/output window for H₂S corrosion in FREECORP.

Another unique feature of the model is that any electrochemical reactions, including built-in reactions and user-defined reactions, can be added to or removed from the corrosion process. With this feature, the effect of each reaction can be clearly identified through the variation of corrosion rate resulting from the addition or removal of a particular reaction. By accommodating user-defined reactions, the applicability of the model is expanded to other steel/environmental systems where electrochemical reaction kinetics are available. The user-defined reaction participates in the calculation process by including a text file containing all necessary parameters in the folder where the program is located. A certain format is required for the text file. Figure 58 shows a template of the text file, which contains required parameter values in an acceptable format.

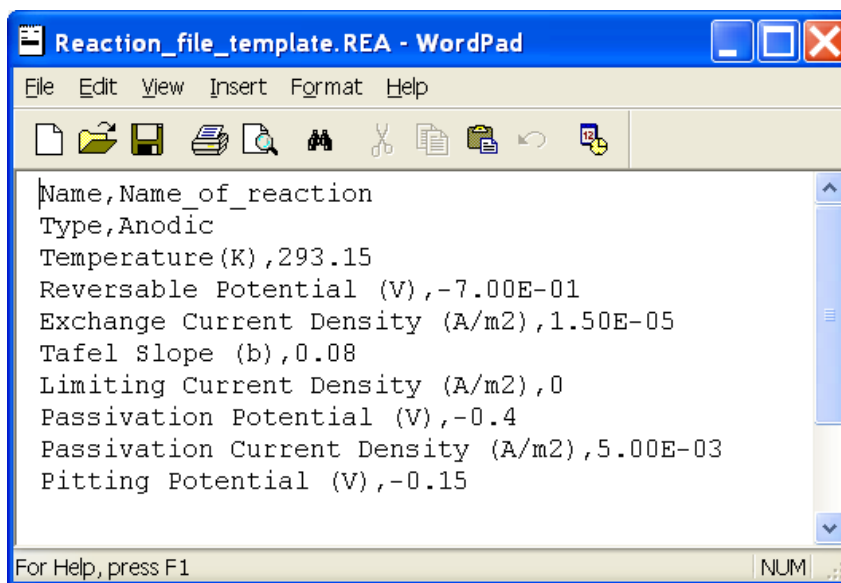


Figure 58. Template for the inputs of a user-defined reaction in FREECORP.

A6.5 Model Limitations

There are a few limitations associated with the model. The major limitations include:

- This model is a so-called “Point model”, where corrosion rate is calculated only for one single point along pipelines.
- This model assumes dilute solution theory, which means that concentrations rather than activities are used in the calculation. In addition, species are assumed to freely diffuse through the solution without coupling with each other.
- This model predicts only uniform corrosion; localized corrosion is not implemented in the current version of the model.

- The effect of high salt concentration on the corrosion process has not been taken into account in the current model.
- Flow dynamics are not implemented in this model, which makes the model applicable only to single phase flow. However, with object-oriented code structure, it is possible to couple this model with other external flow simulators, such as OLGA, for multiphase flow corrosion predictions.
- Effect of FeCO_3 and FeS layer are taken into account through simple empirical correlations which are related to supersaturation of FeCO_3 and H_2S concentration, respectively.
- When CO_2 and H_2S coexist in the system, the model determines the dominant corrosion process in a somewhat simple manner. CO_2 and H_2S corrosion rates are individually calculated based on the corresponding mechanisms; the one that gives the higher corrosion rate is considered to be the main corrosion cause.

As model development progresses, most of the above limitations are expected to be overcome in the near future.

A6.6 Model Verification

The model has been verified using both in-house experimental data as well as data available in the open literature. Good agreement was obtained between the model and experiments for various conditions. The comparisons are extensively demonstrated in the user manual of FREECORP.¹³⁸ This section presents some of the comparisons in order to give a general sense of the prediction accuracy.

Figure 59 shows the comparison between predicted and measured polarization curves. Although no direct comparison can be made for individual electrochemical reaction kinetics, good agreement is obtained between measured and predicted potentiodynamic sweeps. The total cathodic and anodic polarization curves indicate that corrosion is under charge transfer control at the corrosion potential under tested conditions. Therefore, it can be expected that corrosion rate would not change with further increase of velocity. This case clearly demonstrates the value of the model in elucidating the corrosion mechanisms, which is not easily achieved through experiments.

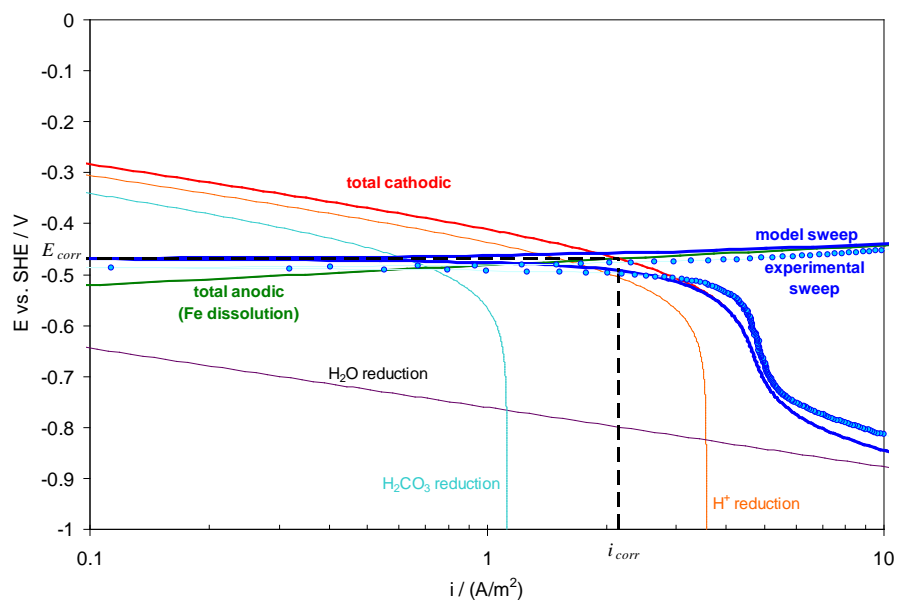


Figure 59. Comparison of experimental and FREECORP predicted polarization curves for temperature 20°C , partial pressure of CO₂ 1bar, solution pH 4 and velocity 2 m/s.¹⁶

Figure 60 shows the comparisons between the model and experiments for varied CO₂ partial pressure and velocity. Good agreement is achieved under all conditions. The

figure indicates that measured corrosion rates hardly change with increasing velocity under relatively high CO₂ pressure. This is because, under the tested conditions, corrosion process is largely limited by the CO₂ hydration rate, which is not sensitive to the change in flow. It can be seen that this behavior is successfully captured by the model; no significant corrosion rate change is predicted with change in velocity.

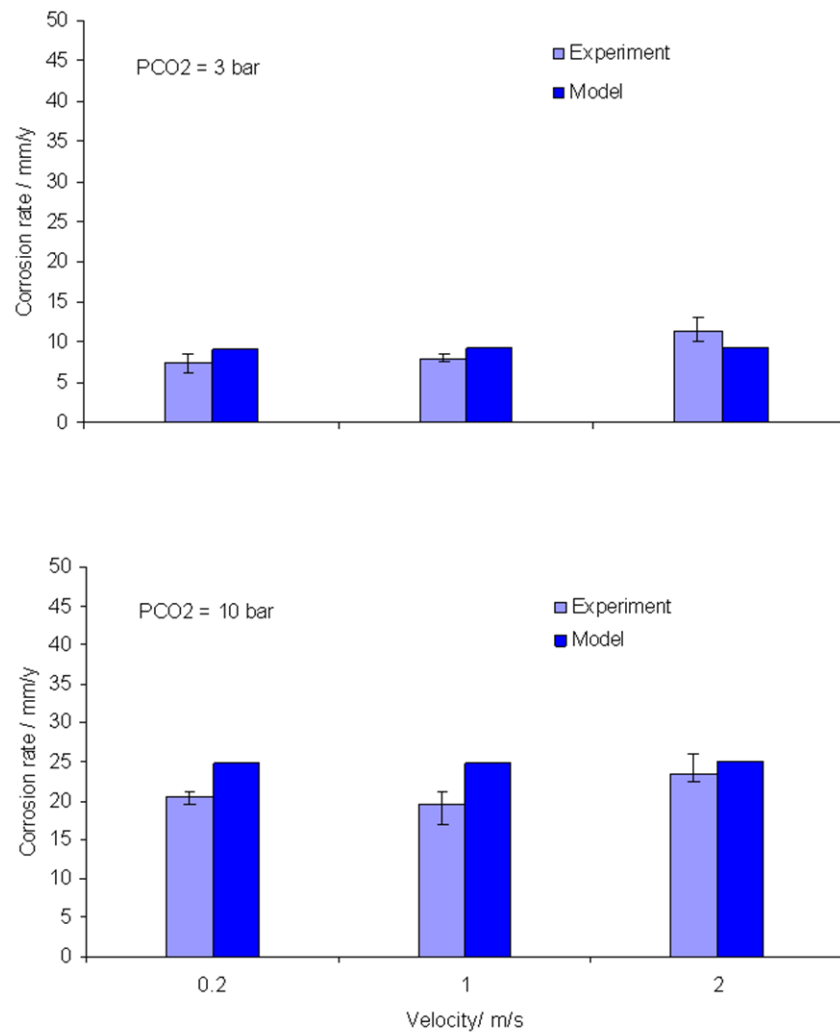


Figure 60. Comparison between FREECORP predictions and experiments for different partial pressure of CO₂. Test condition: temperature 60°C, pH 5, pipe diameter 0.1 m. Data is taken from ICMT database.¹⁶

Figure 61 shows the predicted and measured corrosion rate as a function of HAc concentration. Both the model and the experiments suggest an increase in corrosion rate with increasing HAc concentration. Compared to *Figure 60*, it is evident that the

corrosion rate caused by HAc is much higher than that associated with CO₂ at the same pH, indicating much higher corrosiveness of HAc.

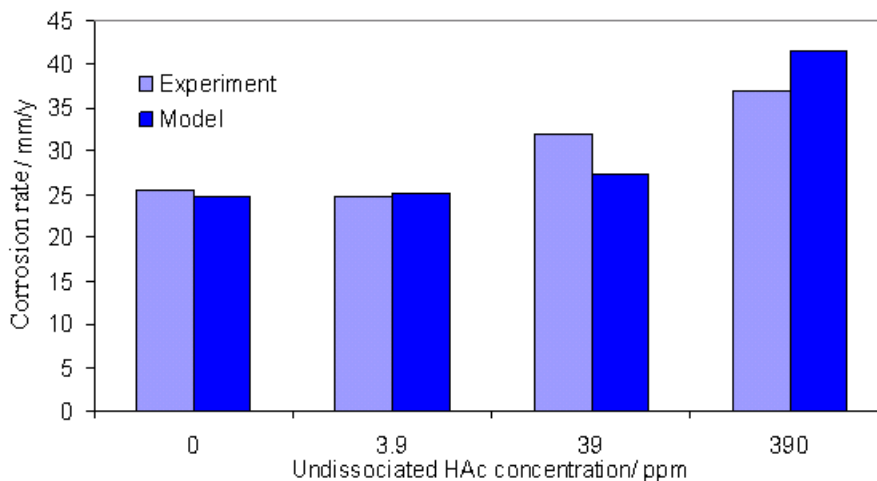
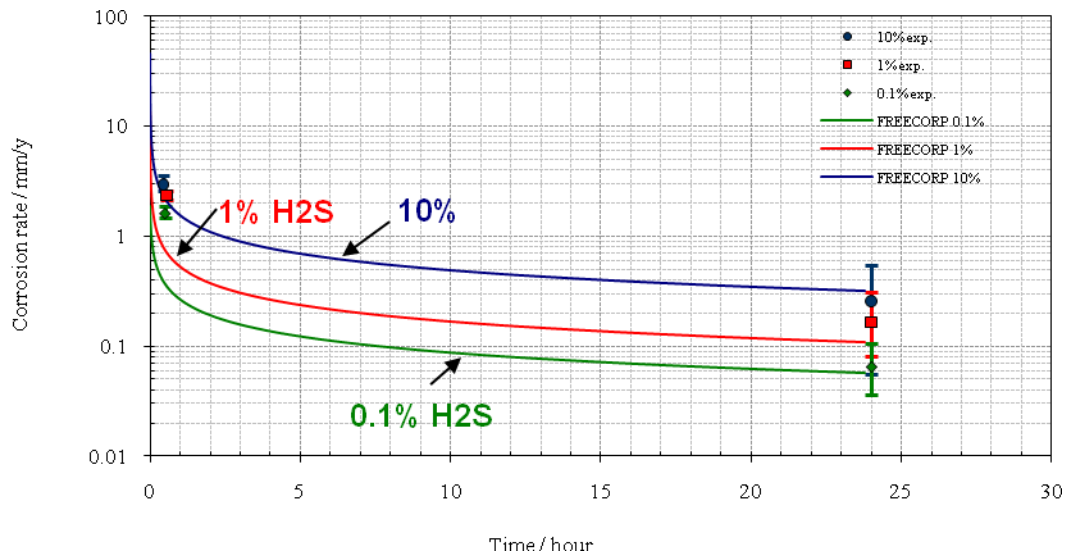


Figure 61. Comparison of experimental and FREECORP predicted corrosion rate. Test conditions: temperature 60°C, pH 5, liquid velocity 1 m/s, partial pressure of CO₂ 10 bar, pipe diameter 0.1m.¹⁶

Figure 62 shows the corrosion rate evolution with time for different H₂S concentrations. It can be seen that the measured corrosion rates decrease as time advances. This is due to the development of makinawite film on the metal surface which enhances the mass transfer resistance to corrosive species. Higher H₂S concentration increases the flux through the makinawite film and leads to a higher corrosion rate.



Fi

Figure 62. Comparison of FREECORP predictions and measurements for H₂S corrosion. Test conditions: temperature 80°C, pH 5, liquid velocity 1 m/s, pipe diameter 0.1m. Data is taken from icmt database.¹⁶

Figure 63 demonstrates the comparison between model predictions and experimental results reported by Institute for Energy Technology, Norway (IFE).¹³⁹ The test conditions are listed in Table 10. The table reflects a wide variety of test conditions which involve multiple factors. Nonetheless, the model predicts comparable corrosion rates to those obtained in the experiments. The agreement in these complex and varied corrosive environments indicates the solid and trustworthy theoretical basis of the model, which can be confidently used as a predictive tool for H₂S/CO₂/HAc environment in the recommended range of parameters as presented in section 5.7.

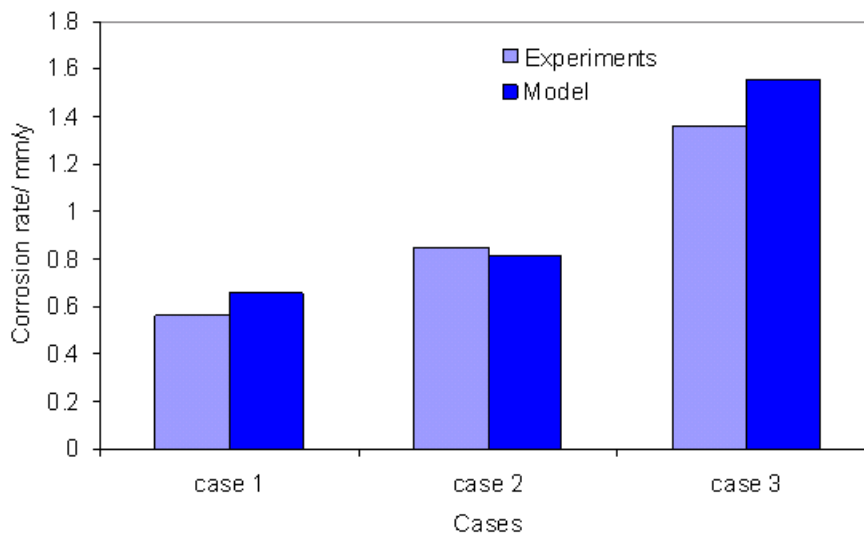


Figure 63. Comparison of measured and FREECORP predicted corrosion rates under the conditions listed in Table 10.¹⁶

Table 10. Test conditions taken from open literature¹³⁹ for FREECORP verification

Parameters	Case 1	Case 2	Case 3
Temperature, °C	80	25	80
pCO ₂ , bar	3.3	3.3	10.0
pH ₂ S, bar	10	10	30
Solution pH	3.10	3.20	2.90
Pipe diameter, m	0.015	0.015	0.015
Velocity, m/s	1	1	1
Duration, days	19	21	15

A6.7 Conclusions

A mechanistic model is developed in this work to predict uniform corrosion of carbon steel in CO₂, H₂S, HAc and/or O₂ environment. The model, called FREECORP, is built based exclusively on open literature and is freely available to public users. The model is written as a Microsoft Excel[®] add-in, the source code of which is made open to the public. An object orient programming approach was adopted in developing the source code, which allows for easy modification of the model. FREECORP provides the flexibility of adding or removing any built-in reactions as well as user-defined reactions into or from the system. This provides a tool to evaluate the effect of individual reactions on the overall corrosion process. Apart from corrosion rate, the model provides other valuable information to assist with the understanding of underlying corrosion mechanisms. Contribution of individual corrosive species to overall corrosion rate can be quantified for easy identification of the main corrosive species. For CO₂/ HAc / O₂ corrosion with electrochemical process dominant, polarization curves are given for individual reactions as well as total anodic and cathodic reactions. For H₂S corrosion, where mass transfer limiting is assumed, the concentration profile of H₂S across the inner and outer magnetite films and the liquid boundary layer are displayed.

The model has been extensively verified against a large number of experiments, taken both from in-house databases and the open literature. Good agreement is achieved under various conditions, reflecting a solid theoretical root in the model. The model can confidently be used in the parameter range within which verification was performed. The recommended range of parameters are: temperature 20 to 120°C; pipe diameter 0.01 to 1

m; liquid velocity 0.001 to 20 m/s; Fe^{2+} 0 to 100ppm; HAc 0 to 1000ppm and pH 3 to 7.

Although the level of uncertainty might increase for the predictions made beyond this range, it should still be able to provide good guidance as to the corrosivity of the environment, owing to the mechanistic nature of the model.